Abstract

Title of Dissertation: Dust Structure and Composition Within Molecular Clouds and Cores

Nicholas Lane Chapman, Doctor of Philosophy, 2007

Dissertation directed by: Professor Lee G. Mundy
Department of Astronomy

We observed three molecular clouds and four isolated cores at wavelengths from 3.6 – 24 μm. The clouds we observed were Ophiuchus, Perseus, and Serpens and the cores were L204C-2, L1152, L1155C-2, and L1228. Our goal was to use these deep infrared data to map changes in the extinction law and the dust properties throughout the observed regions.

In our clouds, we found the lowest density regions have an IRAC extinction law similar to the one observed in the diffuse ISM. At higher extinctions, there is evidence for grain growth because the extinction law flattens compared to the diffuse ISM law and becomes more consistent with a model utilizing larger dust grains. In the densest regions of Serpens and Perseus, $A_{K_s} \geq 2$, it appears icy mantles are forming on the dust grains. We detected one low extinction region in Perseus with an anomalous extinction law that is not explained by current ideas about grain growth or the formation of ices onto dust grains.

The extinction law in the cores shows only a slight flattening of the extinction law with increased extinction. Even at the lowest extinctions, the extinction law is more consistent with a dust model containing grain growth, rather than with the diffuse ISM. Two of the four cores have evidence for ices forming the densest regions. Molecular outflows appear to have an impact on the dust grains in two of our cores: L1152 and L1228.

In both our clouds and cores, the extinction law at 24 μm is almost always higher than the value predicted by current dust models, but is consistent with other observations. We find some evidence for the 24 μm extinction law decreasing as the extinction increases. Overall, there are relatively few stars with detections $\geq 3\sigma$ at 24 μm. More observations are needed to understand the nature of the extinction law at this wavelength.

Dust Structure and Composition Within Molecular Clouds and Cores

by

Nicholas Lane Chapman

Dissertation submitted to the Faculty of the Graduate School of the
University of Maryland at College Park in partial fulfillment
of the requirements for the degree of
Doctor of Philosophy
2007

Advisory Committee:

Professor Lee G. Mundy, chair
Professor Neal J. Evans
Professor Eve Ostriker
Professor Stuart N. Vogel
Professer Richard Walker
Professor Mark Wolfire

To anyone who has ever looked up at the starry night sky and wondered

Acknowledgements

If I have seen further it is by standing on the shoulders of giants

- Isaac Newton

I find Newton's quote particularly apt because this thesis would have never seen the light of day without the support, contributions, and help from many other people. First and foremost, I would like to thank my advisor, Lee Mundy. As an advisor, Lee has always given me the freedom to explore and discover my research interests. He has also helped build my independence and self-motivation, two qualities needed to become a successful scientist. We have also had many useful scientific discussions whenever I ran into a mental brick wall. Finally, I would like to thank him for his continued efforts to improve clarity and precision of my scientific writing.

Furthermore, I would like to acknowledge some of the unsung heros in this department. To John Trasco and Mary Ann Phillips who quietly keep the department running, day in and day out. Additional thanks to Mary Ann for the chocolate supply in her office. Also, Peter Teuben has given me immeasurable amounts of his time and technical expertise. Without him, none of the

software I used could have ever been written and this thesis would be merely a dream. Additional thanks to the computer staff who keep the departmental computers running and backed up.

Thanks also to my fellow graduate students who have done their best to delay my graduation by making me do fun things. In particular, I would like to thank my officemates, Misty La Vigne, Lisa Wei, and Ashley Zauderer. Also, Matthew Knight, who got me playing fantasy football, and Mia Bovill, a good friend. Finally, even though she is not a current student, I would like to thank Mandy Proctor for much needed moral support as I have tried to turn all my research into a coherent thesis. I always looked forward to observing runs at Kitt Peak as a chance to catch up with her.

Finally, my family have supported me financially and emotionally over the years. My mom always told me to stay in school as long as possible and I did my best. My dad never begrudged financial support for school and for numerous trips home to visit. Thanks also to Genevieve, who was the youngest sibling but still managed to get her Pharm. D. before any of her older brothers got doctorates, Christopher who helped me move (twice!), and Alexander for first getting me interested me in physics all those years ago.

Contents

List of Tables

List of Figures

Chapter 1

Introduction

1.1 The Importance of Dust Grains

Dark nebulae were first discovered in the late 1700's by Caroline and William Herschel (Herschel 1785). However, it was over 100 years later before dark nebulae were established as discrete, optically thick clouds (Wolf 1923). With these observations, plus work by Trumpler (1930), it was established that interstellar grains caused the obscuration, or extinction.

For decades, the only way to study these clouds was through the dust grains. The discovery of the 21 cm H I emission lead to the observation of a general correlation at low extinction between the H I emission and absorption (Lilley 1955). However, dust clouds showed little, if any, H I emission suggesting that any gas in these clouds was molecular (Bok et al. 1955; Heiles 1969). This was confirmed with the detection of CO in the interstellar medium (Wilson et al. 1970). Since then, these dust clouds have been known as molecular clouds because the dust absorbs the ultraviolet radiation and allows molecules to form.

Molecular clouds have been established as the sites for star formation. As such, studying the physical properties of clouds is important for understanding star formation. Dust

grains offer several advantages over molecules. First, the constancy of the gas-to-dust ratio has been well established so dust grains are an excellent tracer of the bulk mass in the cloud, namely H_2 (Bohlin et al. 1978; Jenkins & Savage 1974; Predehl & Schmitt 1995). Molecular tracers, on the other hand, can suffer depletion in cold regions (Evans 1999). Stars form in dense regions and the dust attenuates the light from these stars. To obtain the true luminosities for these protostars, it is necessary to correct for the column density of dust along the line-of-sight. This requires knowledge of the extinction and the extinction law, or variation of extinction with wavelength. Lastly, from studying the extinction law the properties of the dust grains themselves can be inferred. The properties of the dust grains can shed light on the environment within the clouds.

1.2 Measuring Extinctions

The most direct method for computing the extinction is to observe the spectrum towards a star along a given line-of-sight. With knowledge of a star's spectral type, the extinction in any waveband can be accurately determined. Obtaining a spectrum for each and every star in a field is too time-consuming for this method to work on large regions. The star count method (Wolf 1923), whereby the decrease in the total number of stars within a given patch of sky is an estimator of the extinction within that patch, can be used over large cloud regions though it is limited by poor resolution (several arcminutes at best) and the random distribution of the stellar background. Another method is to compute the 100 μm optical depth from the ratio of the IRAS 60 and 100 μm emission. This is then converted to visual extinction (Wood et al. 1994). This technique does not rely on the distribution of background stars but still has low resolution since it is limited by the IRAS beam size.

The real breakthrough in extinction measurement came from Lada et al. (1994) who

used a technique called Near-Infrared Color Excess (NICE) to map the extinction within IC5146 using H and K bands. They exploited the fact that the extinction law is roughly constant over many sightlines in the near-IR (Cardelli et al. 1989) and that the intrinsic $H-K$ color for stars has a small dispersion. Thus, even if the true spectral type is unknown, an accurate estimate of the extinction can be determined. This method has been widely adopted for studying the structure of molecular clouds and cores. Alves et al. (2001) mapped B68 and found the density profile could be well-fit as a critically stable Bonnor-Ebert sphere. The structure of B335 and L694-2 were mapped by Harvey et al. (2003, 2001). Both had super-critical density profiles suggesting collapse is occurring in these cores. This theme is reiterated by Lada et al. (2004) who observed a ring of extinction within a globule of the Coalsack nebula. The authors speculate this may be a core in the process of formation. Larger clouds have been mapped as well, such as L977 by Alves et al. (1998) and IC5146 (Lada et al. 1999, 1994).

The 2MASS survey, which mapped the entire sky in the JHK_s bands, makes it easier than ever to construct extinction maps of arbitrary regions. Using the 2MASS data, Lombardi & Alves (2001) devised an improvement to the NICE technique, dubbed NICER, for Near-Infrared Color Excess Revisited. The idea behind NICER is to use the $J-H$ and $H-K_s$ colors simultaneously to calculate the "best" extinction value, i.e. the one with minimum variance. Using this method, they were able to construct extinction maps with half the variance of maps made using the standard NICE method ($H-K_s$). The authors later used this method to map 48 deg^2 of the Pipe nebula using the 2MASS data (Lombardi et al. 2006).

1.3 Changes in Dust Properties

The dust properties appear to vary with column density. In the diffuse ISM, numerous studies have shown that $R_V \equiv A_V/(A_B - A_V)$, the ratio of total-to-selective extinction, has a value of 3.1 (e.g. Rieke & Lebofsky 1985; Whittet 1992). In the denser ISM, R_V values range from $4-6$ (e.g. Kandori et al. 2003; Strafella et al. 2001; Vrba et al. 1993). These observations are consistent with the idea of larger average grain sizes in dense regions, which leads to larger R_V values. Kim et al. (1994) used the maximum entropy method to create smoothly varying grain size distributions that reproduced R_V values of 3.1 and 5.3. The $R_V = 5.3$ grain distribution had $\sim 10\times$ fewer small grains ($< 0.1\,\mu$m in size) compared to the $R_V = 3.1$ grains. Kramer et al. (2003) combined $450/850\,\mu$m and *JHK* observations to study the dust properties in IC 5146. They found evidence for the formation of ices onto grains in the densest cores, consistent with Ossenkopf & Henning grain models (Ossenkopf & Henning 1994). Schnee et al. (2005) used extinction maps derived with NICER and compared them with the $100\,\mu$m dust opacity (derived from the IRAS 60 and 100 μm images). They found that the conversion factor from τ_{100} to extinction varied between molecular clouds and even within clouds. This factor is directly related to the dust properties.

Observations along various lines of sight have produced several empirical extinction laws. The de facto "standard" extinction law is the Rieke & Lebofsky (1985) $R_V = 3.1$ law. This law has become a standard because of its apparent universality in the near-infrared. At longer wavelengths, this extinction law does not appear quite as universal. The Rieke & Lebofsky (1985) law follows a power law from the near-infrared out to $\sim 7\,\mu$m before increasing again towards the $10\,\mu$m silicate extinction peak. More recently, a flatter extinction law in the mid-infrared has been found in observations of hydrogen recombination lines towards the Galactic center using the Infrared Space Observatory

(Lutz 1999; Lutz et al. 1996). Using the Spitzer Space Telescope, other authors have found a similarly flat extinction law from $3.6-8\,\mu$m along other lines of sight (Flaherty et al. 2007; Indebetouw et al. 2005).

1.4 Theoretical Grain Models

The observed extinction law directly relates to the dust grain properties. One of the classic standard grain models is the Mathis et al. (1977, MRN) grain model. This model consists of two grain populations, silicate and graphite, with a power law range of grain sizes ($n(a)da \propto a^{-3.5}da$). It did an excellent job of matching observations of several sightlines through diffuse clouds. Since then, various observations have highlighted the need to revise this model. Cardelli et al. (1989) showed that in the UV/optical wavelengths, the extinction law varies depending on the line-of-sight. These changes could be characterized by a single parameter, $R_V = A_V/(A_B - A_V)$. For the diffuse ISM, $R_V \sim 3.1$ while larger values are found in dense clouds.

Furthermore, observations of dust thermal emission in the $3-60\,\mu$m regime suggest the existence of grains much smaller than the MRN lower limit (50 $\AA$) (e.g. Draine & Anderson 1985). Emission features at 3.3, 6.2, 7.7, 8.6, and $11.3\,\mu$m are believed to be due to C-C and C-H vibrational modes in polycyclic aromatic hydrocarbons (PAHs) (Leger & Puget 1984). Both of these sets of observations suggest the existence of a population of extremely small carbonaceous grains.

In Figure 1.1 we have plotted three modern theoretical dust models along with the results from four empirical studies. These studies provide good fits to the various observations. Weingartner & Draine (2001) $R_V = 3.1$ fits the Rieke & Lebofsky (1985) data points, while their $R_V = 5.5$ model provides a good fit to the flatter data found by several other authors. The model proposed by Pontoppidian et al. (in prep.) also provides a

good fit to the flatter data points and includes ices which are not present in either of the Weingartner & Draine models.

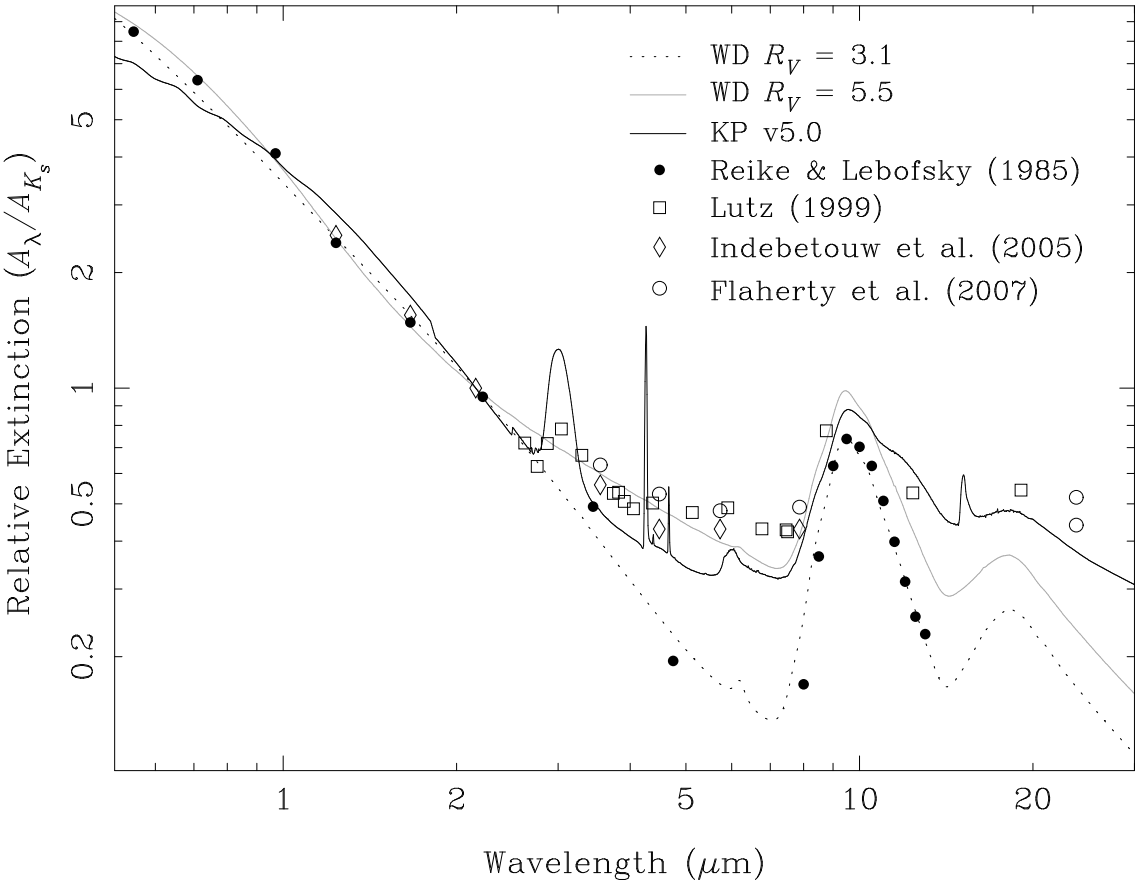

Figure 1.1: Various theoretical and empirical extinction laws. Curves are shown for Weingartner & Draine $R_V = 3.1$ and 5.5 (dotted and gray lines) and Klaus Pontoppidian et al. (black line) dust models. The data points correspond to empirically derived average extinction laws from Lutz (1999) (squares), Rieke & Lebofsky (1985) (filled circles), Indebetouw et al. (2005) (diamonds), and Flaherty et al. (2007) (open circles). All extinction values are scaled relative to the extinction in the K_s band.

The Weingartner & Draine (2001) models incorporate small graphite and PAH grains to match observations from various lines of sight. Their $R_V = 3.1$ model fits the "standard" Rieke & Lebofsky extinction law and provides a bridge to previous extinction studies. Compared to $R_V = 3.1$, their $R_V = 5.5$ model incorporates a slightly different dust distribution with a larger number of carbonaceous/silicate grains and a greater fraction of larger grains (see Figure 1.2). This model matches observations in denser regions which

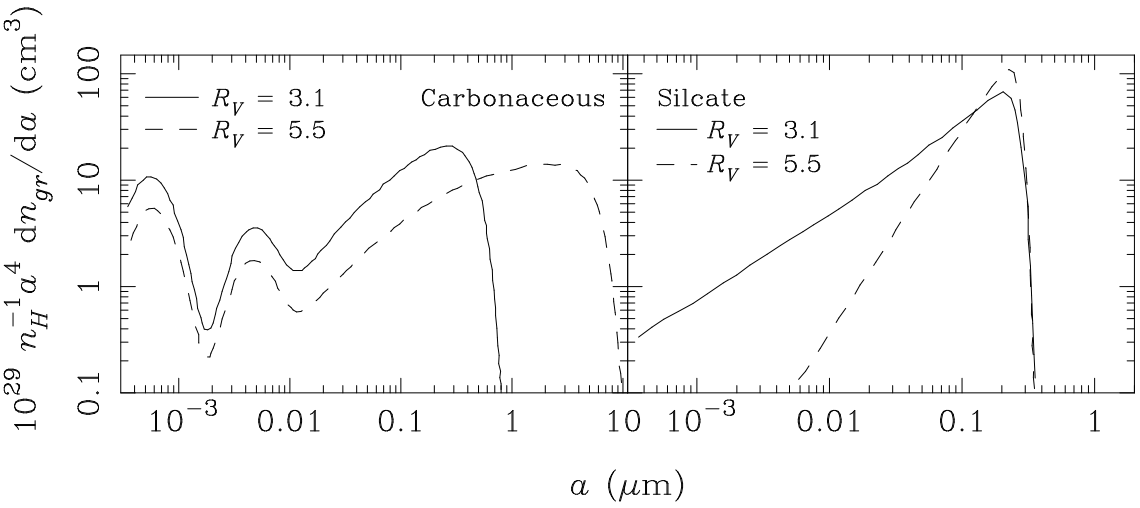

Figure 1.2: Comparison of the Weingartner & Draine $R_V = 3.1$ vs. 5.5 dust models. The two grain populations, carbonaceous (left) and silicate (right), are shown. The $R_V = 5.5$ model has larger carbonaceous dust grains, and fewer smaller dust grains as compared to the $R_V = 3.1$ model.

have found a flatter extinction law in the mid-infrared.

One area in which the Weingartner & Draine dust models are deficient is the lack of support for ice features. In cold dense regions, it is reasonable to assume that icy mantles may form on dust grains which can alter the predicted extinction law. The Pontoppidian et al. dust model utilizes a simplified version of the WD3.1 dust model and adds icy mantles from both water and volatiles. Several ice absorption features can be seen in Figure 1.1, these are due to H_2O, CO_2, and CO.

1.5 This Dissertation

High spatial resolution observations are crucial to the study of dust properties; there is ample evidence showing that dust structure exists on scales less than several arcminutes (e.g. Alves et al. 1998; Lada et al. 1999, 2004, 1994). Yet, no sensitive, high spatial resolution, large area surveys to investigate dust properties exist. This dissertation was designed to address this hole by making such a survey. In the following chapters we will

present observations from $1.25 - 24\,\mu$m of three molecular clouds and four isolated cores. We will attempt to answer the following questions:

1. How are dust grain sizes and compositions related to the extinction?
2. How do star forming regions impact dust properties?
3. Do the dust properties differ between clouds, between cores, and between clouds and cores?

In chapter 2 we will discuss in detail our observations, data reduction, and methodology. Chapter 3 will then present the results for our three clouds: Perseus, Ophiuchus, and Serpens. Then, in chapter 4 we will discuss our four cores: L204C-2, L1152, L1155C-2, L1228. We observed these cores with very deep mid-infrared observations to look for faint protostars. In addition to a discussion of the dust properties, we will present our results on faint YSOs in the cores. Finally, in Chapter 5 we will present our conclusions and directions for future research.

Chapter 2

Producing Source Catalogs

2.1 Introduction

In this chapter we will discuss the details on how our source catalogs were created. Our near-infrared JHK_s bands were processed separately from the mid-infrared wavelengths ($3.6 - 70\,\mu$m) so we will discuss them separately below. In § 2.2 we will describe the steps we took to create calibrated source catalogs at the JHK_s wavelengths including how we dealt with instrumental defects. In § 2.3 we will summarize the c2d data processing pipeline. For further details, refer to the c2d delivery documentation (Evans et al. 2007). It is also available online[1]. We will examine the reliability of our JHK_s and mid-infrared photometry in § 2.4.1. In § 2.5 we will describe our method for automated source classification. Some of this is discussed in the c2d delivery documentation, though we compute our extinctions in a different manner from c2d. We will investigate the accuracy and reliability of our extinctions in § 2.6. Finally, in § 2.7 we will explain how we created the average stellar models used in this dissertation.

[1] http://ssc.spitzer.caltech.edu/legacy/c2dhistory.html

Table 2.1. JHK_s Observations Summary

Semester	Regions Observed	"Missing Flux" Problem?
2003B	L1155C-2	N
2004B	Serpens,Perseus,L1152,L1155C-2,L1228	Y
2005B	Perseus,L1152,L1155C-2,L1228	Y
2006A	Ophiuchus,Serpens,L204C-2	N

Note. — The third column refers to the presence or lack of the so-called "missing flux" problem in the observations. See § 2.2.4 for further discussion on this instrumental effect.

2.2 Near Infrared Data Processing

This section describes the method we used for processing our near-infrared data. Our observations were taken with the FLoridA Multi-object Imaging Near-ir Grism Observational Spectrometer (FLAMINGOS) (Elston 1998). We used the Kitt Peak 4-meter telescope during the 2003B - 2006A observing semesters. In Table 2.1 we summarize our observations including whether a specific instrumental defect, the "bad" quadrant, is present in the data set. In § 2.2.4 we will discuss this effect in detail. All data processing was performed with custom written scripts in python and using PyRAF[2]. The FLAMINGOS instrument has a $\sim 10' \times 10'$ field of view. To map our cloud regions, we mosaicked individual fields together. Each field overlapped its neighbors by $1-2$ arcminutes. Within each field, we observed multiple dithers with small position offsets from the center.

[2]PyRAF is a product of the Space Telescope Science Institute, which is operated by AURA for NASA

2.2.1 Dark/Flat/Sky Processing

The first steps in our JHK_s data reduction pipeline followed a fairly standard procedure (Howell 2000). We first subtracted a median filtered dark image from each dither. Secondly, the dithers were flat-fielded by dividing out a dome flat. The last, and most important, step was to subtract out the sky. This is critical for IR observations where the sky is typically much brighter than the astronomical objects of interest. We used a two-pass sky subtraction using a running median. This means that for each dither, we median combined the nearest dithers in time to compute a median sky image which was then subtracted from the target dither. For example, if our target dither was #6 in a sequence, we would use dithers #3-5 and 7-9 to find the median sky image. The combination of dithering and median combining the data resulted in a sky image that was reasonably clear of stars. However, in fields with high stellar density or containing extremely bright sources, the median sky image was still contaminated by the effects of stars. To correct for this, we performed a second sky subtraction. In the first pass, we median combined the nearby dithers and subtracted off the sky. From this first pass sky subtraction, we created an object mask of the stars. Then, for the second pass sky subtraction, we first masked out the pixels from the object mask before median combining the dithers. This method produced an improved sky subtraction.

2.2.2 Coordinate Refinement

After the two passes of sky subtraction, we combined together our individual dithers into a single image for each field by manually determining the linear shift between dithers. The world coordinates for the final images were corrected by using the 2MASS catalog as a reference.

2.2.3 Source Extraction and Photometry

To find sources, we used the IRAF task `daofind`. We visually inspected the output source list to delete false detections and also add sources missed by the source extractor. We used the IRAF task `daophot` to obtain photometry for each source. This procedure works by PSF fitting which was critically important for the crowded star fields in Serpens.

Similar to our coordinate refinement, we used the 2MASS catalog to calibrate our photometry in each region. For each field and wavelength, we selected approximately 20 2MASS sources scattered throughout the frame. These 2MASS sources were selected to be ~ 1 mag. above the 10σ limits for the 2MASS survey to ensure the sources had reliable photometry and also faint enough to not be saturated. The sources were used to create a model PSF which we used to calibrate the photometry for every source.

2.2.4 "Missing Flux" Quadrant

The bulk of our observations suffer from a "missing flux" problem for sources located within one quadrant of the CCD (see Table 2.1). We uncovered this effect when reducing our data from the 2004B observing run. Stars within this quadrant were up to ~ 0.5 mag. fainter when compared to 2MASS photometry. This effect spanned multiple filters and fields. Stars in the remaining three quadrants of the CCD were not affected. The root cause of this problem is believed to have been a deterioration of the coating on the BaF2 "field lens" which acted as the entrance window to the camera dewar (Eikenberry et al. 2005, private communication). We planned our observations during the 2005B observing run in such a way that the affected quadrant in each field overlapped with an unaffected quadrant in the adjacent field. We then discarded data from the quadrant with the "missing flux" problem in each field. The BaF2 coating was removed after our 2005B observing run. Based on analysis from our 2006A data, we determined this "missing flux" problem

had been resolved.

For our 2004B observations, we still needed to deal with the "missing flux" problem. The simplest solution would have been to throw out all stars within the affected quadrant in every field we observed. This method was unappealing because it would have meant the loss of 25% of our mapped area and left gaps in our coverage maps. Rather than do this, we decided to correct the photometry for the affected stars using the 2MASS photometry as a "truth" table.

The persistence of the "missing flux" across filters, different nights, and even different observing runs suggested the phenomenon was slowly varying with time. Therefore, for each waveband, JHK_s, we combined the photometry from *all* sources in *all* fields obtained over the 2004B observing run into a single field. We then created a uniform map of the difference between our psf-fitted magnitude and the 2MASS magnitude for each field by overlaying a uniform grid on the data. At each grid point, we computed the weighted average of the magnitude difference, weighted both by uncertainty and distance from the grid position. The resultant difference map for our 2004B H band data can be seen in Figure 2.1. The "missing flux" region covers a significant fraction of the upper-righthand quadrant of the CCD.

Once we had created the magnitude difference map for each band in the 2004B observing run, we converted these maps to flux difference maps, but ignored any differences from zero that were $\leq 2\sigma$. We multiplied the final dark subtracted, flat-fielded, sky-subtracted, and dither combined image for each field by the relevant flux difference map. The net effect was to artificially increase the image counts for sources within the affected quadrant while not altering the values elsewhere in the image (except for the edges). We then recomputed our source photometry on the new re-scaled image. Finally, for each source we summed the photometric error in magnitudes in quadrature with a factor to account for uncertainties in this flux correction process. This factor was the larger of: 10%

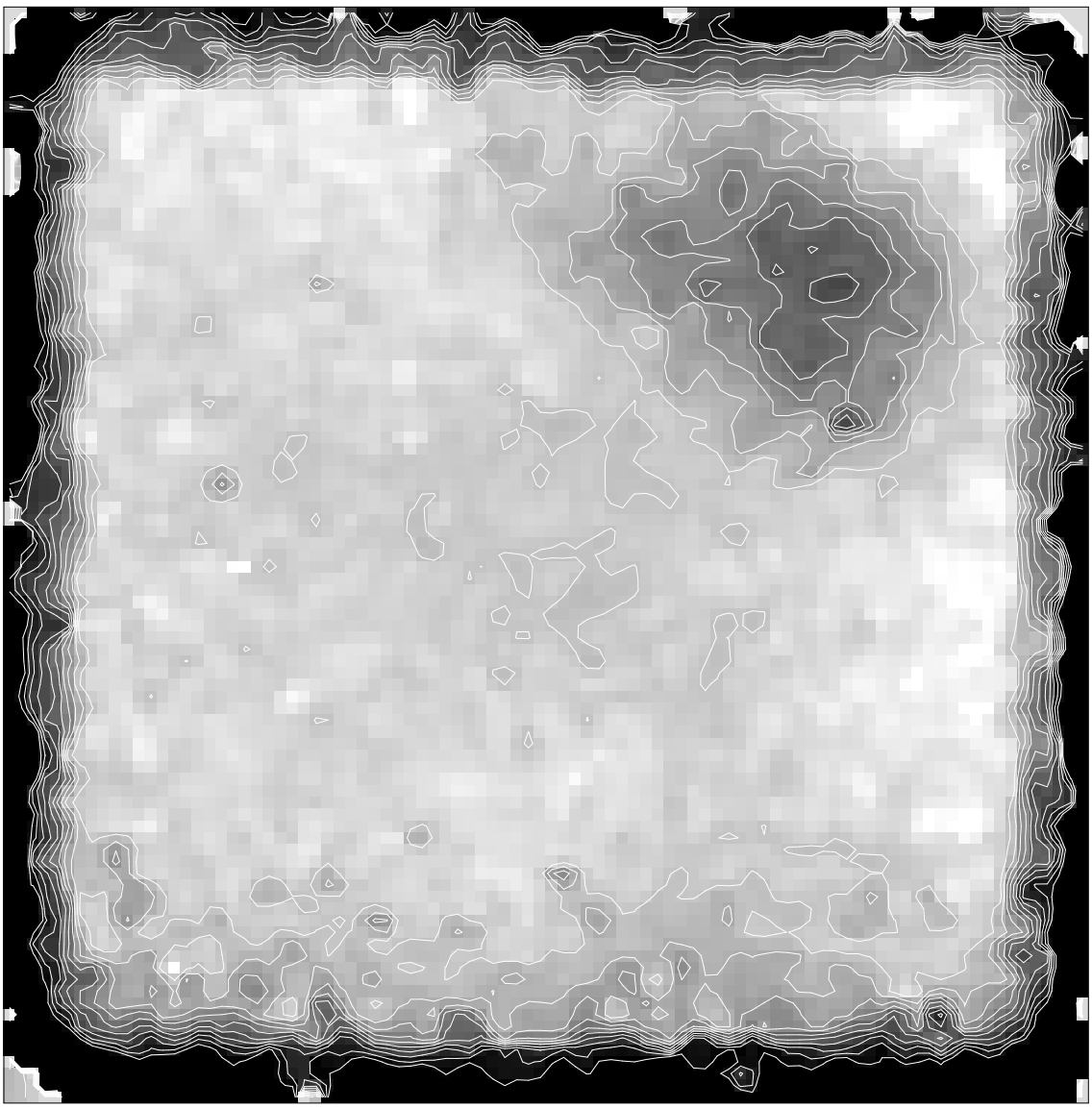

Figure 2.1: Difference between our PSF fitted magnitude and the 2MASS magnitude for *H* band using all source extracted from our 2004B observing run. The affected quadrant, where our photometry is significantly fainter than 2MASS, is clearly visible in the upper right quadrant of the image. Contours start at 3σ (0.06 mag.) in steps of 3σ. Also note the photometry deviates from 2MASS along the edges due to distortions of the stars in the images. Our mosaics were planned in such a way that these edges overlap with unaffected regions in the adjacent fields.

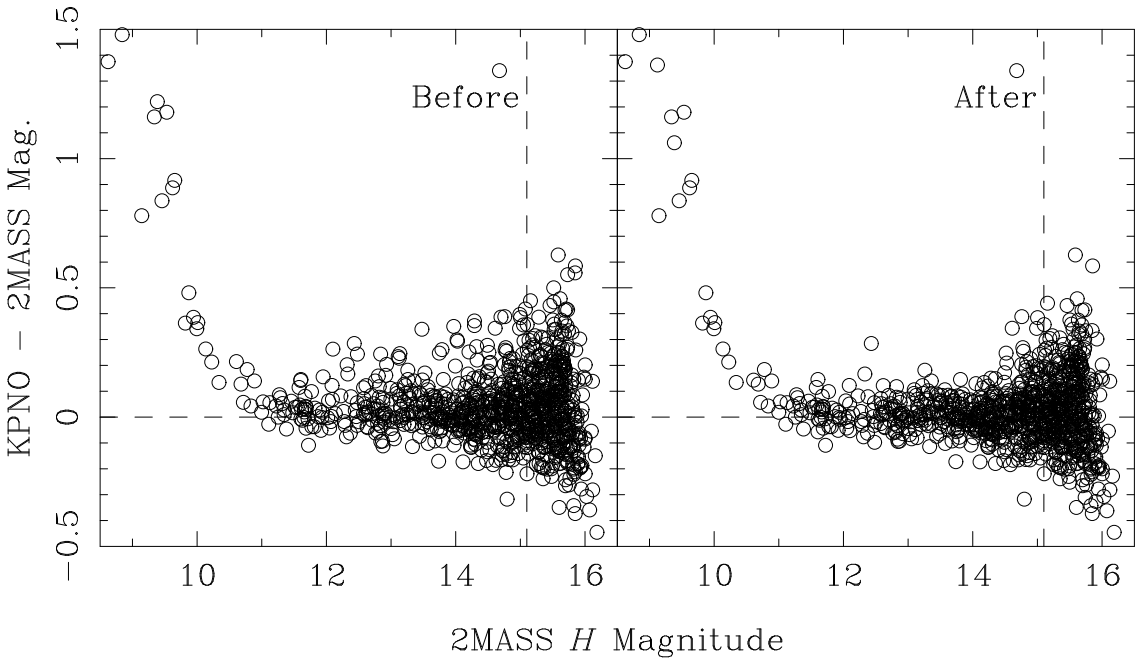

Figure 2.2: The difference between our PSF fitted magnitude (KPNO) and the 2MASS H band magnitude for one of our fields in Serpens. The left panel shows the distribution before we have applied the correction for the "missing flux" and the right panel shows the improvement to the photometry after correcting for the "missing flux". The vertical dashed lines denote the 2MASS 10σ limit of 15.1 mag. in the H band. Saturation is clearly evident for sources brighter than $\sim$ 11th magnitude.

of the pixel value in the difference map at the location of the source or the overall standard deviation of the difference map. The net result of our correction can be seen in Figure 2.2. On the left-hand side we have plotted our initial difference in point source magnitude vs. 2MASS H magnitude for one of our fields in Serpens. In the right-hand panel, we have plotted the same thing after our photometric correction for the "missing flux". A number of the points with differences of $\sim 0.2 - 0.3$ have been corrected in the righthand panel. Note that brighter than $\sim$ 11th magnitude, our observations are saturated. We will deal with saturated sources in the following section.

2.2.5 Creating the JHK_s Catalogs

We combined our photometry-corrected source lists from each field in each band to create a final source list for each band in each region. Since our mosaics were planned with overlap between adjacent fields, we positionally matched sources between one field and another and then excluded the source that was closer to its fields' edge. This allowed us to remove sources with poor photometry that are near the edges of each field (see Figure 2.1). Sources near to the edge which were not matched with a source in the adjacent field were excluded.

Next, we band-merged the source list for each band to create the bandmerged catalog. In our final catalogs, not all sources were detected at the J, H, and K_s bands. Of these, we visually inspected those detected in at least 2 bands with an average quality of detection of 'B' (i.e. one band with quality 'A' and the second band with quality 'C', or both with quality 'B', or both with quality 'A'). The quality grades refer to the S/N of the detection where 'A' is $\geq 7\sigma$, 'B' is $\geq 5\sigma$ and 'C' is $\geq 3\sigma$. Any sources which appeared real were added to our source extraction lists and a flux was fitted for that position in the missing band. If `daophot` found a non-zero flux for the position, the source was added to our bandmerged catalog. This process was called bandfilling. Our final bandmerged and bandfilled catalog only contains sources detected in all three near- infrared wavelengths. We do not have any upper limits.

The final step in creating our final JHK_s catalog was to replace the fluxes for saturated fluxes. For 2MASS sources brighter than 11th magnitude, we substituted the 2MASS fluxes in for our saturated ones. See Figure 2.2 for an example of saturated sources.

2.3 Mid-Infrared Data Processing

All our mid-infrared observations come from the Spitzer Space Telescope (hereafter *Spitzer*) (Werner et al. 2004). We utilized the two imaging instruments on-board *Spitzer*, the InfraRed Array Camera (IRAC) (Fazio et al. 2004) and Multiband Imaging Photometer for Spitzer (MIPS) (Rieke et al. 2004), to probe the $3.6 - 70\,\mu$m wavebands. Our observations of Ophiuchus, Perseus, and Serpens utilize the data from the *Spitzer* Legacy Science Program "From Molecular Cores to Planet-Forming Disks" (c2d) (Evans et al. 2003). The four cores in our sample, L204C-2, L1152, L1155C-2, and L1228 were part of a separate *Spitzer* observing program called 'DeepCores'. However, these data were also processed using the c2d pipeline. Detailed discussion of the c2d pipeline is part of the c2d data delivery documentation (Evans et al. 2007). We will give just a brief overview of the c2d pipeline here. The c2d pipeline is divided into multiple teams: the IRAC-cc and MIPS-cc teams are in charge of calibration and quality checking of the individual *Spitzer* images; the map1 team mosaics the data and creates the source extractions; finally, the map2 team visually inspects the source extractions, merges together the source extractions from different wavelengths into a single source, and classifies each source based on its spectral energy distribution. Mr. Chapman is in charge of the map2 team.

2.3.1 Image Processing

Our observations are divided into Basic Calibrated Datasets (BCDs) where each BCD represents a single exposure at a given wavelength that has been processed through the Spitzer Science Center's (SSC) pipeline. All our data were processed by the SSC using the S13 version of their pipeline. Starting from the BCDs, the c2d IRAC-cc (Tracy Huard, CfA) and MIPS-cc (Tim Brooke, Caltech) teams further processed the images to remove additional instrumental effects. Before any other processing, we first corrected for "jail-

bar" effects in both the IRAC and MIPS data. The IRAC "jailbar" effects are due to bias level drifts. The SSC had previously corrected for this effect in their pipeline, but this was not done in S13 because it was believed the improvement was negligible. The IRAC-cc team obtained the SSC's "jailbar" correction module and applied it to our data. For MIPS, we also corrected a "jailbar" response pattern that is caused by bright sources or cosmic rays by applying an additive correction to the low readouts to bring them up to the same level as the high readouts.

Improvements to IRAC BCDs

We applied corrections for three image artifacts that appear near bright sources: muxbleed, column pulldown, and banding. Muxbleed appears as rows of uniformly bright pixels adjacent to very bright sources in IRAC bands 1 and 2 (3.6 and 4.5 μm). The IRAC-cc team corrected these values by interpolation from a predetermined table. Column pulldown has an opposite effect as muxbleed: the column values near bright sources are too low. This primarily effects bands 1 and 2, though we applied the correction to all four IRAC bands. To fix column pulldown, we applied an additive correction to bring these values up to the median value of surrounding pixels. Finally, banding affects rows in bands 3 in 4 by depressing the source counts. We applied a similar technique to the one used for column pulldown to correct this effect.

After we applied these three corrections for artifacts, we also performed a correction for the "first-frame" effect in band 3. The bias level of an image depends on the elapsed time between the previous observation and the current one. The SSC performs a bias-subtraction when creating the BCDs except for the first long exposure in band 3. To correct for this, we use all the IRAC 3 images in an observation to determine the median value for each pixel in the map, which is then subtracted from the first frame in each observation.

Finally, we applied array dependent photometric corrections as recommended by the SSC. These correct for variations in the photometry across the array.

Improvements to MIPS BCDs

The MIPS-cc team processed the 24 μm images to remove some further instrumental effects. The first four frames in a map were scaled to the median of following frames, and each AOR was self-flattened to eliminate a small instrumental brightness gradient along the column direction. Furthermore, the images were median-combined to create "self-flats". These were used to eliminate several residual image artifacts such as occasional latent images, residual jailbarring, and incompletely corrected illumination patterns.

The SSC provided two sets of BCD products for the 70 μm data, unfiltered (normal processing) and filtered (a time median filter is applied). We did not make any improvements to the SSC images.

The 160 μm data were also not improved by the MIPS-cc team. These data are not used in this thesis and so will not be discussed further.

2.3.2 Mosaicking and Source Extraction

The Map1 team (Paul Harvey & Lucas Cieza, University of Texas) created mosaic images using the SSC's MOPEX program (Makovoz & Marleau 2005) with the outlier rejection, overlap correction, and position refinement modules. For the c2d observations, we took short integrations in the IRAC bands, called high dynamic range (HDR) data to obtain the correct photometry for saturated sources. All our observations in each wavelength were taken in two epochs. The two epochs of observations were separated by 4-8 hours in c2d, and by up to 3 weeks later in DeepCores. Map1 created photometry and mosaics made from three products: the first epoch of data, the second epoch of data, and the combined epochs (utilizing data from both individual epochs and the HDR data, if available). The

initial point source extraction was performed on each mosaic using a modified version of the DOPHOT program (Schechter et al. 1993). This program works by fitting Point Spread Functions (PSFs), so as sources were found, they were subtracted from the image. This procedure was iterated until a user defined flux limit was reached. We calculated the final position and photometry for each source using all BCD images that contributed to that source.

The IRAC and MIPS 24 μm source fluxes were calibrated by computing the ratio between the aperture flux and model PSF flux for all sources with a reliable aperture flux and that could be fitted by the point source profile. We used an aperture box 7 pixels wide for all bands. The average aperture to PSF flux ratio was assumed to hold for all sources, and a multiplicative correction was applied. This ratio was always with a few percent of unity.

The 70 μm point source extractions were performed on mosaic images made using MOPEX on the SSC's filtered and unfiltered BCDs. Source extractions were then performed using the SSC's point source extraction software, APEX, on both mosaic images. We used the Point Response Function (PRF) photometry from the filtered mosaic except for sources brighter than $\sim$ 2 Jy, when the SSC's filtering over corrects in the wings of the PRF. In such cases, we substituted PRF photometry from the unfiltered mosaic.

2.3.3 Bandmerging

The final stage of data processing prior to science analysis of c2d images involved the creation of bandmerged catalogs. Again, refer to the c2d delivery document (Evans et al. 2007) for details.

IRAC - MIPS 24 Bandmerging

For each band, the three source extraction lists (epoch1, epoch2, and combined epochs) were checked for "self-matches" within an epoch; two sources extracted within one epoch, but with positional matches of $\leq 2\farcs0$ were considered to be the same source. The fluxes of the detections were summed, and the position of the source was calculated as the weighted mean. We then merged the three lists together to cross-identify sources with positional matches of $2\farcs0$ or less. We visually inspected the epoch-merged source lists for each band to remove diffraction spikes, column pull-down, latent images, and other image artifacts that were misidentified as sources.

The epoch-merged source lists for each band were then merged as follows. First, we merged the four IRAC bands together, one-at-a-time. We started by merging IRAC1 (3.6 μm) and IRAC2 (4.5 μm), then merged this product with IRAC3 (5.8 μm), and finally combined with IRAC4 (8 μm). At each step, we combined detections at two wavelengths into a single source if the difference in central position was $\leq 2\farcs0$. Then, this bandmerged IRAC catalog was merged with the 24 μm MIPS1 band using a larger distance, $4\farcs0$. The larger distance was used because of the larger PSF at 24 μm compared to IRAC. A 24 μm detection was always matched to the nearest IRAC source, even if there was more than one IRAC source within the $4\farcs0$ radius.

In all steps of bandmerging, we merged together the closest position match between 2 wavelengths. Any other detections within the specified radius were preserved in the final catalog, but not merged.

MIPS 70 μm Bandmerging

Even though we have two epochs of observation at 70 μm, they do not have much overlap between them. Thus, we only performed source extractions on the combined epochs dataset. First, we performed a 'self-merging' on the combined epochs dataset using a matching radius of $4\farcs0$. Secondly, each 70 μm point source detection was matched to all shorter wavelength catalog sources within a $8\farcs0$ radius. We them visually inspected each merged 70 μm detection to determine the 'best' source match between shorter wavelengths ($1.25 - 24\,\mu$m) and 70 μm. This 'best' source match was the one with the most consistent Spectral Energy Distribution (SED) across all detected wavelengths. In a few cases where it was not clear which SED was 'better', we chose the closer match.

Shorter wavelength sources that were within $8\farcs0$ of a 70 μm detection but *not* matched with the 70 μm, were assigned a special flag to denote their status. Thus, in our final catalog, a 70 μm detection is listed *once* ; we did not try to split up the flux to different shorter wavelength sources.

JHK_s Bandmerging

The last step to creating our final source catalogs for each cloud and core was to merge our *Spitzer* catalogs with the JHK_s catalogs obtained from Kitt Peak. This merging was performed similarly to other steps; we compared the JHK_s catalog with our *Spitzer* one using a distance matching criterion of $2''$. In cases where there was more than one possible match between JHK_s and *Spitzer* catalogs, we always chose the closest match.

2.4 Reliability

In this section we will evaluate the reliability of the fluxes and positions of our catalogs. We will concentrate primarily on the reliability of our JHK_s source extractions. The reliability of our *Spitzer* observations is discussed extensively in the delivery documentation (Evans et al. 2007).

2.4.1 JHK_s Reliability

For all our JHK_s catalogs we performed three tests on the reliability and accuracy of the positions and photometry for these wavebands. We used the 2MASS data for comparison with our catalogs. To ensure that we only used high quality 2MASS sources in our comparison, we restricted ourselves to sources brighter than 14.5, 14.0, and 13.0 magnitudes in the J, H, and K_s bands, respectively. These limits are above 2MASS' 10σ limits of 15.8, 15.1, and 14.3 magnitudes in the J, H, and K_s bands, respectively[3]. We have included figures showing the results from the Serpens molecular cloud; our other regions show similar results.

In Figure 2.3 we have plotted a logarithmic histogram of the difference between our final coordinates in our Serpens catalog and those of the 2MASS catalog. Our mean difference in position is $0\farcs15$ and 95% of our sources have a difference in position of $0\farcs6$ or less (around 2 pixels on the FLAMINGOS CCD).

In Figure 2.4 we plot normalized histograms of the flux difference between our Kitt Peak observations and the 2MASS catalog for all 2MASS sources. The best-fit Gaussian for each waveband is also shown with $\sigma = 0.04 - 0.05$. Based on this analysis, we believe our fluxes are correct to $\sim 5\%$. From the 2MASS documentation, the photometry for bright, non-saturated sources in 2MASS have a precision of 1-2%.

[3]http://www.ipac.caltech.edu/2mass/releases/allsky/doc/explsup.html

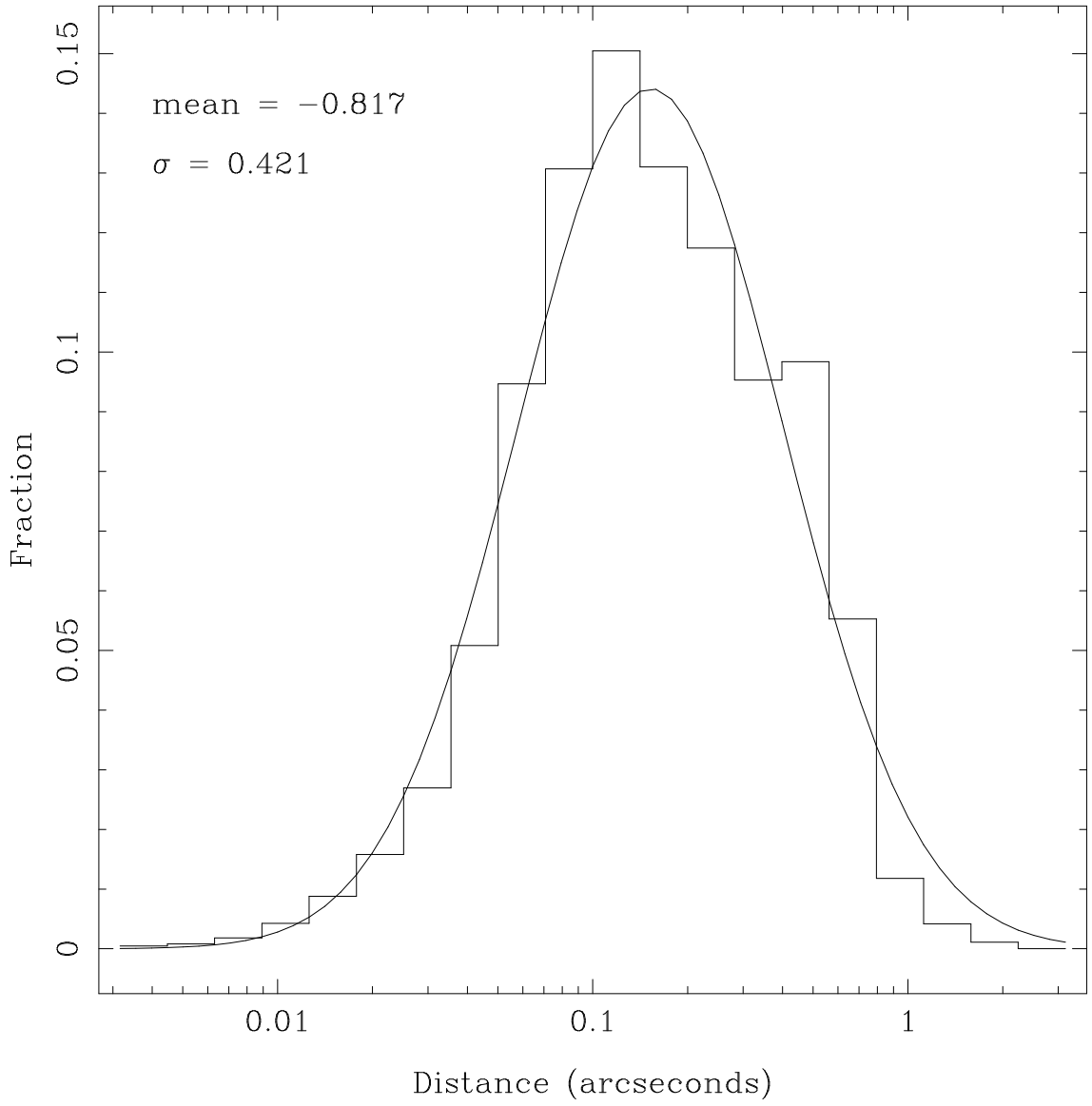

Figure 2.3: Normalized histogram showing the distance, in arcseconds, between 2MASS and KPNO positions. The data are for our Serpens observations. The mean is $0\farcs15$ and 95% of our positions differ by $\leq 0\farcs6$.

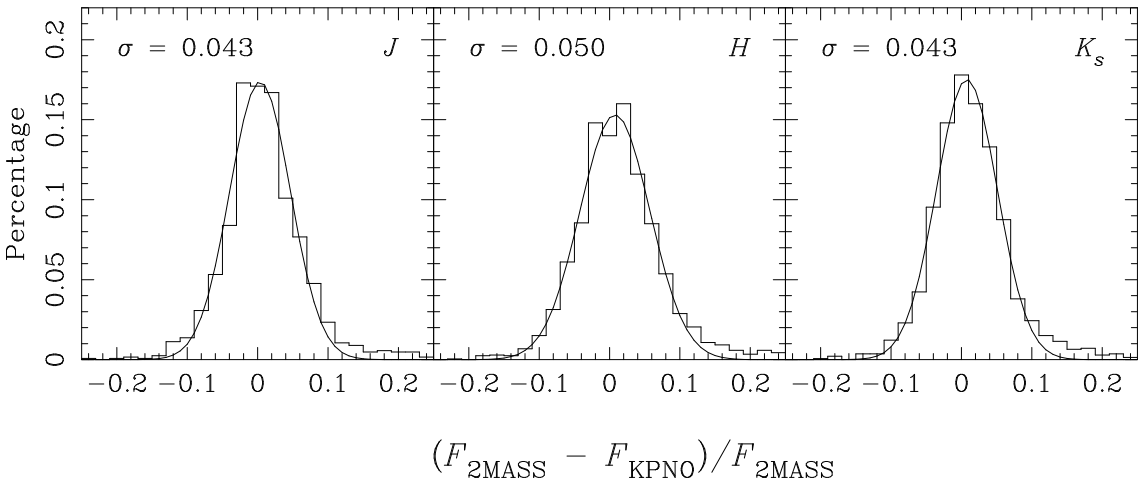

Figure 2.4: Histograms of the difference between our final catalog flux and the 2MASS flux for the J,H,$K_s$bands. The best-fit Gaussian function is overlaid on each histogram with $\sigma = 0.04 - 0.05$. The catalog shown is the Serpens cloud; catalogs from other regions have similar uncertainties.

A final concern with our catalogs is that we may need to apply a color correction due to differences between the 2MASS and FLAMINGOS filters. In Figure 2.5 we have plotted the difference in magnitude between our Kitt Peak data and the 2MASS photometry for the JHK_s wavebands. If a color correction was needed, we would see a deviation from zero difference at larger $H - K_s$ values (Huard et al. 2007). We do not observe any such effect in our data. Therefore, we have not applied any correction to our final catalogs based on potential differences in the 2MASS and FLAMINGOS filter systems.

2.4.2 Mid-IR Reliability

To assess the statistical uncertainties in the c2d data, the c2d Quality team (Neal Evans & Mike Dunham, University of Texas) compared c2d observations of some isolated cores with deeper observations of the same objects. These deeper observations came from two *Spitzer* General Observer programs: "DeepCores" (used in this thesis), and "Cores2Deeper" (PI Phil Myers, *Spitzer* PID 20386). The Quality team compared the magnitudes obtained by c2d with those from these deeper observations and used the re-

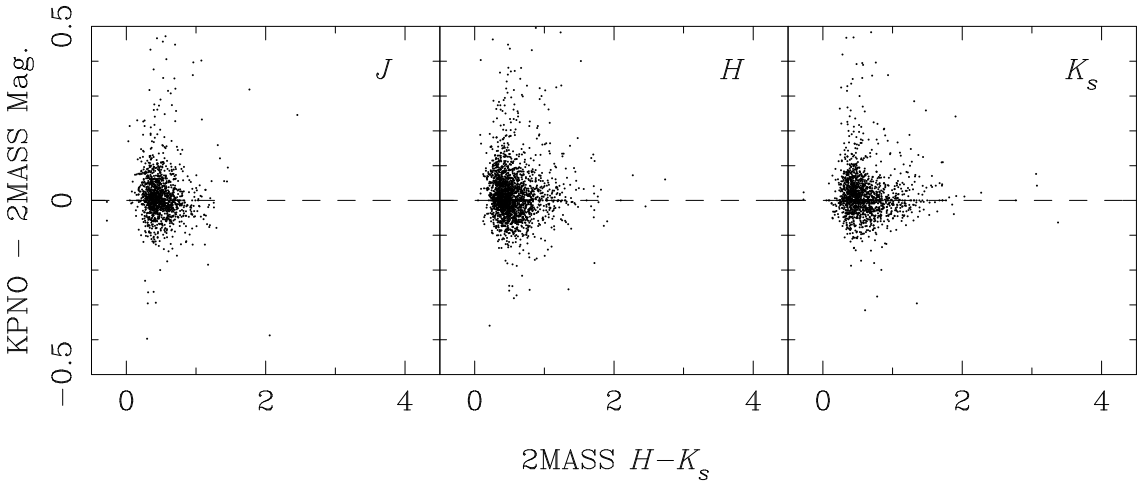

Figure 2.5: Plot of the difference between our Kitt Peak magnitude and the 2MASS magnitude vs. $H-K_s$ color for our Serpens data. Note that there does not appear to be any deviation from zero difference at large $H-K_s$ color for any waveband. All three bands have an average difference < 0.01 mags. with a standard deviation of $0.04-0.05$ mags. A deviation would be observed if a color correction needed to be applied to our photometry.

peatability of the measurements to estimate the statistical error. Based on these measurements, the c2d team determined there were two separate effects: first, the statistical uncertainties listed in the catalog were too low by a factor of ~ 2.3 and second, there was a floor to the minimum uncertainty obtainable on bright sources of 0.05 magnitudes in IRAC and 0.10 magnitudes in MIPS1 (24 μm).

Furthermore, the c2d team compared their photometry with standard stars to estimate the calibration uncertainty. From this analysis, only performed with the IRAC bands, the c2d team found their photometry was consistent with the expected values within 5%. For MIPS1 and MIPS2, the c2d team used the SSC estimates for the calibration uncertainties: 4% (24 μm) and 20% (70 μm).

2.5 Source Classification

Our source classification procedure was developed by Dr. Shih-Ping Lai for the c2d team. This method classifies sources based on their SEDs at wavelengths from $1.25 - 24\,\mu$m. It is important to include the effect of dust extinction when identifying stars because star light is often dimmed by significant dust in the molecular clouds we observed. The observed flux of a reddened star, $F_{obs}(\lambda)$, can be described with the following equation:

$$\log(F_{obs}(\lambda)/F_{model}(\lambda)) = \log(K) - 0.4 \times C_{ext}(\lambda) \times A_{K_s} \tag{2.1}$$

where $F_{model}(\lambda)$ is the stellar photosphere model, K is the scaling factor of the model for a particular star, and $C_{ext}(\lambda) \equiv A_\lambda / A_{K_s}$ is the ratio of extinction at wavelength λ to extinction at K_s from the dust extinction law. K and A_{K_s} can be derived from the linear fit of this equation by adopting stellar photosphere and dust extinction models. The stellar photosphere models for K_s–MIPS1 bands are based on the Kurucz-Lejeune models and come from the SSC's "Star-Pet" tool[4]. For the 2MASS bands, we translated the observed $J-H$ and $H-K$ colors of stars (Koornneef 1983) to fluxes relative to K band and ignored the difference between K and K_s bands.

Each source is classified by several possible criteria. First, we attempt to fit all available wavelengths with a reddened stellar template. If this fails, we exclude each band one-by-one and re-attempt a stellar fit. We do this since a star may have a prominent absorption or emission line in one band. Any sources that cannot be fit as stars are subjected to further tests to classify them. We use three templates to select for Polycyclic Aromatic Hydrocarbon (PAH) emission, star+dust, and finally red sources. If a source fits no other source template, it will be classified based on the shape of the SED.

All non-star objects may also receive a second classification of Young Stellar Object

[4](http://ssc.spitzer.caltech.edu/tools/starpet)

candidate (YSOc) or Background Galaxy candidate (Galc). YSO candidates are traditionally selected from sources with excess flux at near- to far-infrared wavelengths compared to the stellar photosphere. Unfortunately, many background galaxies fit the same description. In order to create a sample strongly enriched in YSO candidates while minimizing confusion from background galaxies, we have used several statistical criteria derived from the SWIRE data of ELAIS N1 (Surace et al. 2004) to separate YSOc sources from other objects with infrared excesses. Since the ELAIS N1 region is towards the North Galactic Pole, we expect the data to contain almost nothing other than stars and background galaxies, making them useful for understanding the distribution of infrared excess non-YSO sources.

We used both IRAC and MIPS data together to identify 'YSO candidates'. The criteria we used were empirically derived from SWIRE and the Serpens molecular cloud. Detailed discussion can be found in the c2d delivery documentation and Harvey et al. (2007a). In brief, we constructed "probability" functions from three color-magnitude diagrams: [4.5] vs. [4.5] - [8.0], [24] vs. [4.5] - [8.0], and [24] vs. [8.0] - [24]. Based on where a source lies in each color-magnitude diagram, it is assigned a probability of being a galaxy. The total probability is then the product of the three individual probabilities. This value may be modified by several factors, including the source's location in an $H-K_s$ vs. $K_s-[4.5]$ color-color diagram. If the final probability is less than a set value, the source is classified as a YSOc, otherwise it will be a Galc. In Figure 2.6 we have shown the four plots used in distinguishing YSOc and Galc objects. This figure is from the c2d delivery documentation and shows the results for the Serpens molecular cloud. The black lines on each figure are *not* hard cutoffs but used to illustrate where the probability cutoffs are assigned. The red line at $[24]=10$ is a hard cutoff. Sources fainter than 10th magnitude at 24 μm are always classified as Galc.

To perform the source classification, all that remains is to choose an appropriate dust

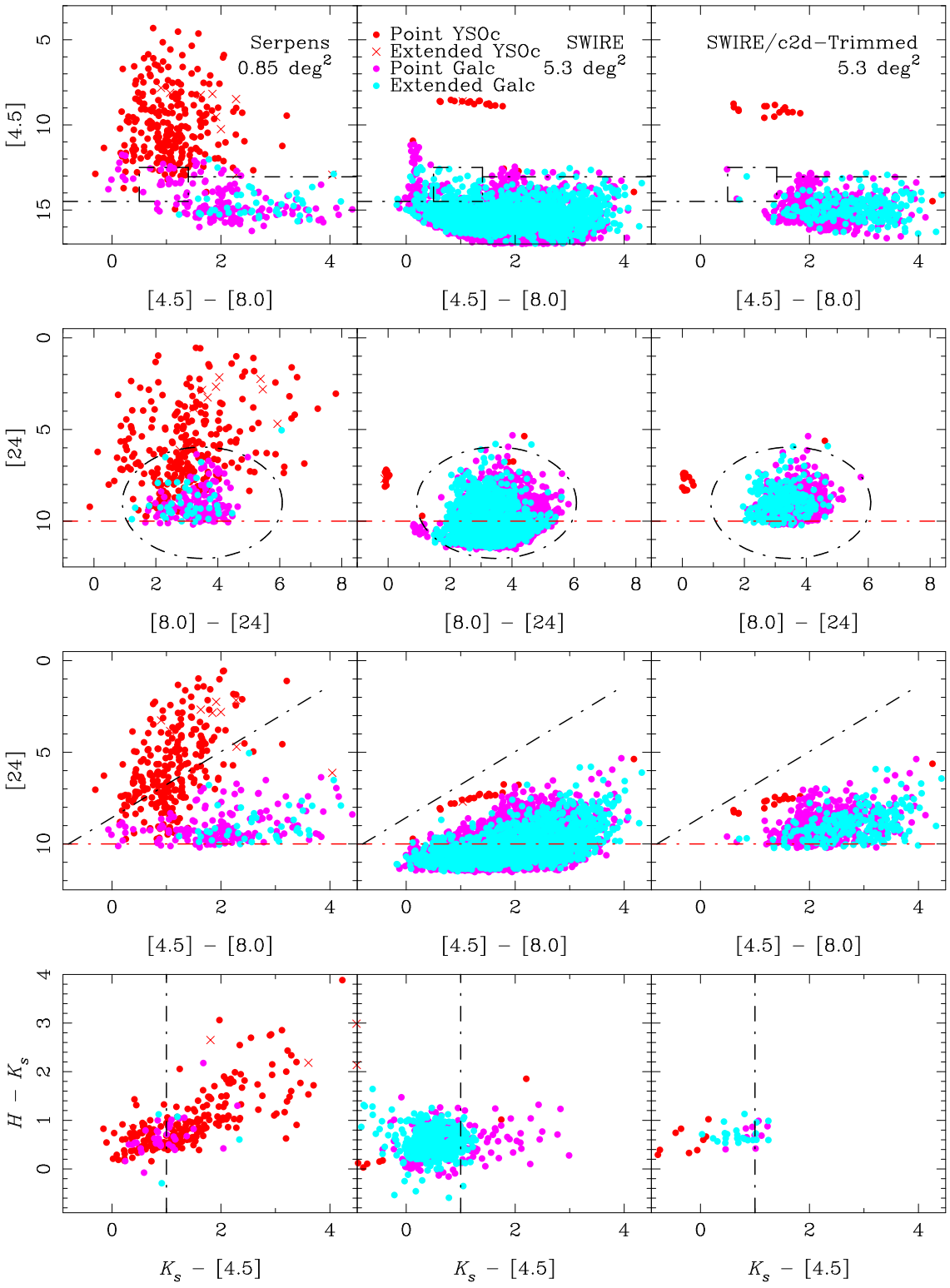

Figure 2.6: Four diagrams showing the selection criteria used for separating YSOc from Galc sources. The left column is for the c2d Serpens data, the middle column is the c2d processed SWIRE catalog for ELAIS N1, and the right column is the c2d processed SWIRE catalog resampled to simulate the extinction and sensitivity of the c2d Serpens observations.

extinction law and then find the best fit values of K and A_{K_s}. The standard c2d pipeline differs from our method in two important respects. First, c2d computed extinctions as A_V, the magnitudes of Visual extinction. We have chosen to adopt A_{K_s}. Secondly, c2d computed K and A_V simultaneously by computing a least squares fit to all available wavebands using equation 2.1. We follow a slightly different procedure: First, A_{K_s} is computed using the JHK_s bands via the NICER technique (Lombardi & Alves 2001). Then, holding A_{K_s} fixed, the best-fit value of K is derived. Our reason for this is that we want to compute the extinction from the JHK_s bands and then use this calculation in deriving the extinction law in the mid-infrared *Spitzer* wavelengths. When only the JHK_s bands are used, we have found this method produces more accurate extinction measurements. See § 2.6 for further discussion. While A_{K_s} could be computed for any source detected in the JHK_s bands, the value is only meaningful for sources classified as stars and therefore not listed in the catalog for non-star source classifications.

2.6 Accuracy of Extinction Methods

There are numerous methods for computing the line-of-sight extinction towards a background star. We will not consider techniques such as star counts or obtaining spectra for each background source since both of these methods are impractical for mapping extinction on large scales with high resolution. Instead, we will focus on techniques that use the photometry from multiple wavebands for each star since this situation describes our data.

The most popular method for computing extinction from photometry is the Near-Infrared Color Excess method (NICE) pioneered by Lada et al. (1994). This method combines aspects of the star counting and spectral techniques to enable large-scale maps of the extinction to be made quickly. The basic idea is that the $H-K_s$ color of a source can be converted into a visual extinction by using a standard extinction law (Rieke &

Lebofsky 1985):

$$A_V = 15.87[(H-K_s)_{observed} - (H-K_s)_{intrinsic}] \tag{2.2}$$

where $(H-K_s)_{intrinsic}$ is the intrinsic $H-K_s$ color for that star. In practice, the intrinsic color for a star is unknown since the true spectral type is unknown. However, in the near-infrared, the scatter in intrinsic $H-K_s$ colors for stars is quite small meaning that an average value, $\langle(H-K_s)_{intrinsic}\rangle$ can be assumed without greatly biasing the resulting value of A_V. Furthermore, this method assumes a certain extinction law (Rieke & Lebofsky 1985). Again, the advantage of using the near-infrared is evident because at these wavelengths the extinction law is fairly independent of line-of-sight (e.g. Cardelli et al. 1989). The scatter in A_V can be further minimized by averaging together spatially nearby values. The NICE technique then computes the A_V towards an arbitrary point as:

$$\hat{A_V} = 15.87\left[\frac{1}{N}\sum_{i=1}^{N}(H-K_s)^i_{observed} - \langle(H-K_s)_{intrinsic}\rangle\right] \tag{2.3}$$

A similar expression to Equation 2.3 can be derived using $J-H$. Lombardi & Alves (2001) combined the extinctions computed from $J-H$ and $H-K_s$ to determine the "best" A_V, i.e. the one with minimum variance. They dubbed this technique NICER, for Near-Infrared Color Excess Revisited. Finally, as an alternative to using infrared colors, the "Cores to Disks" *Spitzer* Legacy Science program has used SED fitting over all available wavebands to determine the extinction.

Which technique provides the most accurate and precise measurements of the extinction? To answer this question, we constructed three model stellar populations with different amounts of extinction: $A_V = 0, 10, 20$. Each population has 10,000 stars and each star is placed at a random distance, which scales the fluxes for every band up or down accordingly. We used the Weingartner & Draine $R_V = 3.1$ extinction law (Weingartner & Draine 2001) to attenuate the fluxes according to the specified A_V. To make

our simulated field as realistic as possible, we used a Kroupa initial mass function (IMF) to weight the stellar population (Kroupa et al. 1993). The input spectral models were the same ones used by the c2d program, which are based on the Kurucz-Lejeune models and come from the SSC's "Star-Pet" tool[5]. The mass for each spectral type came from Cox (2000). Finally, for each waveband from J through MIPS1 (24 μm), we added Gaussian noise to the model fluxes.

For each of our stellar populations, we computed the average extinction and dispersion using five techniques: $J-H$, $H-K_s$, spectral fitting of all bands ($J-24\,\mu$m), spectral fitting of the JHK_s bands, and NICER. We chose to fit spectral types for methods three and four since this is the standard processing procedure followed by c2d and this produces more accurate extinction measurements over using an average stellar model. For the $J-H$, $H-K_s$, and NICER methods we need to assume values for $\langle (J-H)_{intrinsic} \rangle$ and $\langle (H-K_s)_{intrinsic} \rangle$. The values we have chosen to use for all observations in this thesis are:

$$\langle (J-H)_{intrinsic} \rangle = 0.63 \pm 0.16$$

$$\langle (H-K_s)_{intrinsic} \rangle = 0.21 \pm 0.14$$

These values were derived from the lowest extinction regions in the cores L1152, L1155C-2, and L1228. These numbers also agree with the values in our model stellar populations. We did not use the lowest extinction regions in our clouds or in L204C-2 as references since these regions still have moderate extinction and therefore we believe the colors would still contained some reddening.

The results are summarized in Table 2.2. All methods except for spectral fitting of the JHK_s bands do reasonably well in terms of the average extinction for the population being close to the true value. NICER and "Fit All" have lower dispersions than any other

[5](http://ssc.spitzer.caltech.edu/tools/starpet)

Table 2.2. Extinctions from Model Stellar Populations

Method	$A_V = 0$			$A_V = 10$			$A_V = 20$		
	Mean	σ	Median	Mean	σ	Median	Mean	σ	Median
$J-H$	-0.26	1.46	0.05	9.95	1.46	10.26	20.17	1.47	20.49
$H-K_s$	0.06	1.67	0.06	10.46	1.67	10.46	20.87	1.70	20.88
Fit All	0.40	1.11	0.13	10.38	1.12	10.11	20.36	1.11	20.10
Fit JHK_s	1.28	2.51	1.01	11.31	2.50	11.03	21.32	2.54	21.03
NICER	-0.18	1.22	0.17	9.80	1.21	10.15	19.56	1.19	19.93

Note. — Statistics on the extinctions computed using five methods on three model stellar populations ($A_V = 0, 10, 20$). See § 2.6 for a description of how these stellar populations were constructed.

method. Just using the JHK_s bands and attempting to do spectral fitting produces very inaccurate results. Not only are the extinction values too high (by about 1.3 magnitudes), the dispersion is also much larger than any other method.

In this dissertation, we want to compute the observed extinction law in the *Spitzer* wavebands. Therefore, we cannot fit all the wavebands when computing the extinctions; instead, we will use the JHK_s bands alone. Therefore, we have chosen to use the NICER method to compute all our extinctions in this thesis. This technique provides the most accurate extinctions with the lowest standard deviations.

2.7 Average Stellar Models

In later chapters we will be using an "average" stellar model when computing changes in the extinction law. How this "average" model was created is the subject of this section.

We computed the expected stellar distribution for each of our regions: Ophiuchus, Perseus, Serpens, L204C-2, L1152, L1155C-2, and L1228. To compute this distribution, we used the galaxy model from Jarrett (1992); Jarrett et al. (1994). This model produces

source counts broken down by spectral type. With this model we knew, for example, the number of G2 giants versus K0 dwarfs in each region. These source counts gave us a rudimentary weighting function that could be used in computing the average stellar model. However, a weighting function from the raw source counts would ignore the reality that not all spectral types are equally observable at each wavelength. Our next step was to correct for the detection limits of our actual observations. From our data we determined the 5σ limiting magnitudes listed in Table 2.3. The galaxy model lists the extincted K_s magnitude for each star and its extinction, A_V. We used this information, the Weingartner & Draine $R_V = 3.1$ extinction law, and the stellar templates from "star-pet"[6] to compute the magnitude of each star at every observed waveband from $J - 24\,\mu$m. We arbitrarily discarded any detection falling below the 5σ cutoff for the given waveband.

Using the normalized, final, corrected source counts at each waveband as a weighting function, we then computed the average stellar template for each region. Finally, for comparison between the different clouds and cores, we created an average cloud and average core stellar template by averaging together the individual averages. Our results are shown in Table 2.4.

[6]http://ssc.spitzer.caltech.edu/tools/starpet

Table 2.3. 5σ Magnitude Limits

Band	Clouds[a]	Cores[b]
J	20.3	20.3
H	19.5	19.5
K_s	18.4	18.4
IRAC1	17.3	17.3
IRAC2	16.6	18.6
IRAC3	14.3	16.2
IRAC4	13.5	15.4
MIPS1	8.4	11.1

[a] Ophiuchus, Perseus, Serpens

[b] L204C-2, L1152, L1155C-2, L1228

Table 2.4. Average Stellar Model for Each Region

Region	J (mJy)	H (mJy)	K_s (mJy)	IRAC1 (mJy)	IRAC2 (mJy)	IRAC3 (mJy)	IRAC4 (mJy)	MIPS1 (mJy)
Ophiuchus	1.374 ± 0.291	1.335 ± 0.095	1.	0.448 ± 0.018	0.267 ± 0.011	0.178 ± 0.008	0.103 ± 0.006	0.014 ± 0.001
Perseus	1.238 ± 0.276	1.284 ± 0.099	1.	0.457 ± 0.023	0.269 ± 0.011	0.180 ± 0.013	0.101 ± 0.008	0.014 ± 0.000
Serpens	1.560 ± 0.232	1.393 ± 0.061	1.	0.443 ± 0.013	0.261 ± 0.016	0.177 ± 0.005	0.106 ± 0.005	0.014 ± 0.000
Average	1.412 ± 0.152	1.357 ± 0.046	1.	0.447 ± 0.010	0.267 ± 0.007	0.178 ± 0.004	0.104 ± 0.003	0.014 ± 0.001
L204C-2	1.307 ± 0.291	1.311 ± 0.099	1.	0.450 ± 0.020	0.268 ± 0.011	0.178 ± 0.010	0.102 ± 0.006	0.014 ± 0.001
L1152	1.283 ± 0.288	1.302 ± 0.099	1.	0.453 ± 0.021	0.268 ± 0.011	0.179 ± 0.011	0.102 ± 0.007	0.013 ± 0.001
L1155C-2	1.292 ± 0.289	1.306 ± 0.099	1.	0.453 ± 0.021	0.268 ± 0.011	0.179 ± 0.011	0.102 ± 0.007	0.013 ± 0.001
L1228	1.249 ± 0.281	1.288 ± 0.100	1.	0.456 ± 0.022	0.269 ± 0.011	0.179 ± 0.012	0.101 ± 0.008	0.014 ± 0.000
Average	1.282 ± 0.144	1.302 ± 0.050	1.	0.453 ± 0.010	0.268 ± 0.005	0.179 ± 0.005	0.102 ± 0.003	0.013 ± 0.001

Note. — Fluxes are scaled relative to the K_s band.

Chapter 3

The Mid-Infrared Extinction Law in the Ophiuchus, Perseus, and Serpens Molecular Clouds

3.1 Introduction

Molecular clouds are vast parsec scale groupings of gas and dust (Evans 1999; Shu et al. 1987). It is important to understand cloud physical properties if we are to learn about the process of star formation since stars form within clouds. Parameters such as density and temperature vary widely within a single cloud and between clouds due to many mechanisms such as external and internal heating by stars, shocks, and gravitational contraction. The use of dust grains to observed molecular clouds is ideal since they are not affected by possible changes in abundance like tracer molecules such as CO.

In this chapter we will utilize *Spitzer* and deep ground-based JHK_s observations to probe changes in the dust properties within three molecular clouds: Ophiuchus, Perseus, and Serpens. We will compare these results to three different dust models. The Weingart-

ner & Draine (2001) $R_V = 3.1$ and $R_V = 5.5$ models were chosen because they incorporate polycyclic aromatic hydrocarbons (PAHs) and grain growth in the $R_V = 5.5$ model. The third model is being developed by Pontoppidian et al. (in prep) starting from a simplified version of the Weingartner & Draine $R_V = 3.1$ model and incorporating icy mantles on the dust grains. We have used version 5.0 of this model. Throughout this chapter we will denote these models as WD3.1, WD5.5, or KP v5.0, respectively.

3.2 Observations

We mapped regions within the Ophiuchus, Perseus, and Serpens molecular clouds in nine wavebands from $1.25 - 70\,\mu$m. Our *Spitzer* observations ($3.6 - 70\,\mu$m) were taken as part of the "Cores to Disks" *Spitzer* Legacy Science Program (c2d) (Evans et al. 2003), while our JHK_s data were taken at Kitt Peak National Observatory using the FLoridA Multi-object Imaging Near-ir Grism Observations Spectrometer (FLAMINGOS) (Elston 1998). The JHK_s data were taken in three observing runs from September 2004 through June 2006. The *Spitzer* observations have been published previously for Ophiuchus (Padgett et al. 2007), Perseus (Jørgensen et al. 2006; Rebull et al. 2007), and Serpens (Harvey et al. 2006, 2007b).

The c2d observations of Ophiuchus, Perseus, and Serpens cover approximately 11 deg^2 with *Spitzer*'s IRAC and MIPS instruments. Such a large area could not feasibly be observed by FLAMINGOS. So, we have focused on selected regions within these clouds. Our goal is to explore changes in the dust extinction law within molecular clouds so we chose contiguous regions that had a range of extinction values, from low to high. Furthermore, we tried to include small star-forming regions within our mapped areas since these regions may alter the dust properties as well. In Table 3.1 we list the basic properties of these clouds including the areas we mapped with our deeper JHK_s observations.

Table 3.1. Basic Properties of the Clouds

Cloud	l (deg.)	b (deg.)	Dist. (pc)	JHK_s Area (deg^2)
Ophiuchus	353	16	125 ± 25[a]	0.15
Perseus	160	-19	250 ± 50[b]	1.0
Serpens	30	5	260 ± 10[c]	0.33

[a]de Geus et al. (1989)

[b]Enoch et al. (2006)

[c]Straizys et al. (1996)

In Figures 3.1 - 3.3 we have plotted a three color image of each region using the c2d data. The red, green, and blue emission correspond to the 24, 8, and 3.6 μm channels on *Spitzer*, respectively. The green or red outline denotes the area we mapped in the JHK_s bands.

In Ophiuchus we mapped a $\sim 10' \times 60'$ region to the northeast of L1688. There are a number of YSOs on the western side of our map, toward L1688, and several mid-infrared dark cores in the middle and on the eastern side. The primary clump of nebulosity we mapped is so bright that it is saturated at 24 μm and thus shows up as cyan in our color image. The Eastern corner of our mapped area has very little dust luminosity compared to the rest of the region.

Our Perseus observations have a significant amount of dust nebulosity. There is a particularly bright region near the center of our map containing the IRAS source 03382+3145. To the southeast of this region is a cluster of bright red sources. Based on these sources' red appearance in Figure 3.2, they likely have an infrared excess suggesting they are young stellar objects. These sources were not resolved by IRAS, but there is a known source at the same position, IRAS 03388+3139. There are several other isolated infrared

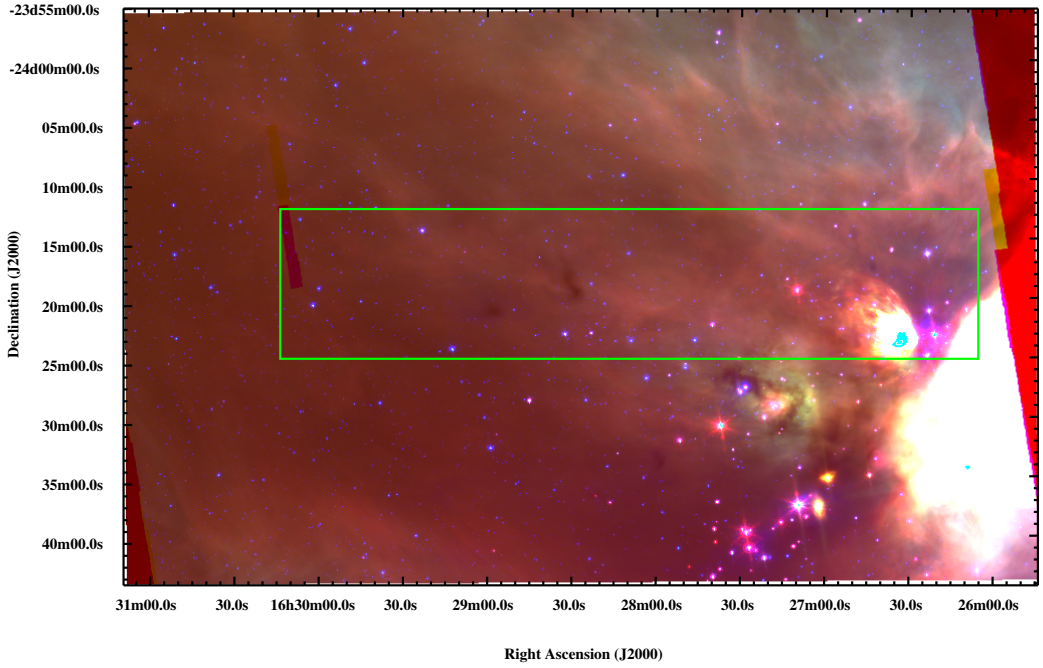

Figure 3.1: Color image of the Ophiuchus cloud made from the 3.6 μm (blue), 8.0 μm (green), and 24 μm (red) channels on *Spitzer*. The green outline denotes the region we observed with our JHK_s observations.

excess sources within the field. Just to the East of our observations is the well-known star-forming region IC348.

Finally, in Serpens we mapped a region surrounding "Cluster B", a group of young stellar objects (YSOs) to the south of the primary Serpens star-formation region and located approximately in the middle of the c2d area (Harvey et al. 2006). There are numerous YSOs within this region and they are not just confined to "Cluster B". There are two notable dark patches that show up in the mid-infrared *Spitzer* data, one to the southeast of "Cluster B", the other to the northeast. Just to the south of our JHK_s maps is the Herbig Ae star VV Ser surrounded by nebulosity.

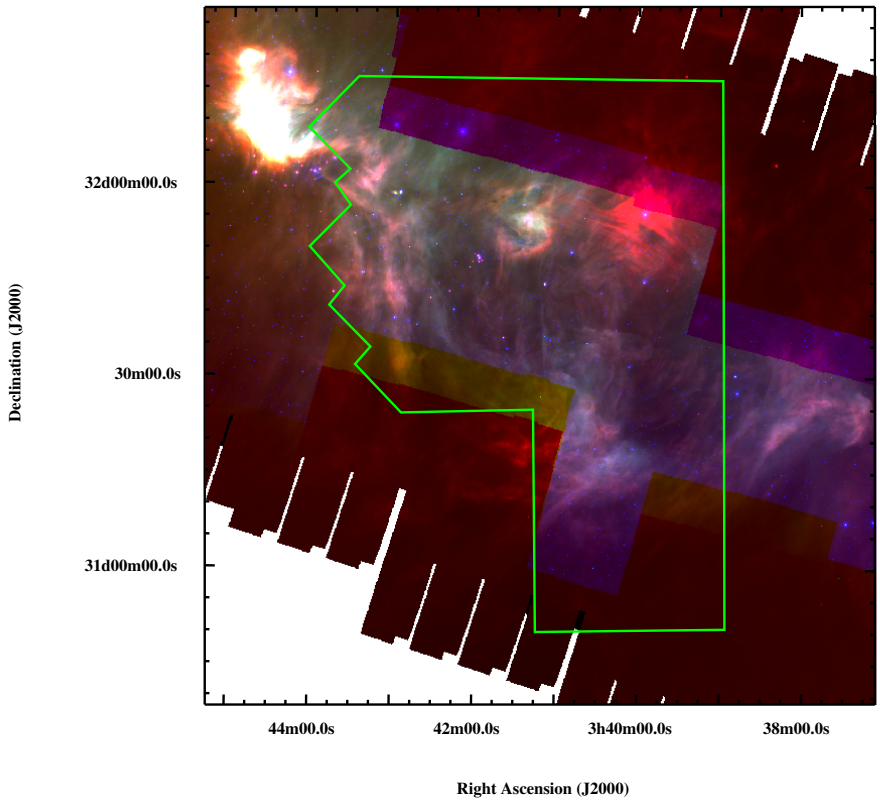

Figure 3.2: Color image of the Perseus cloud made from the 3.6 μm (blue), 8.0 μm (green), and 24 μm (red) channels on *Spitzer*. The green outline denotes the region we observed with our JHK_s observations.

3.3 High-Reliability Star Catalogs

Chapter 2 describes in detail both our and c2d's data reduction pipelines so we will not discuss them here. Our goal in this chapter is to explore how the dust extinction and extinction law changes throughout three molecular clouds. Therefore, high reliability near-infrared JHK_s data are essential because these wavelengths alone are used to calculate extinctions and extrapolate the extinction law in the *Spitzer* bands. Furthermore, we want to restrict our catalogs to stars and JHK_s-only sources. With YSOs, background galaxies, and other infrared excess sources we cannot separate out the expected flux of the SED from changes in those fluxes due to variations in the extinction law. JHK_s-only sources

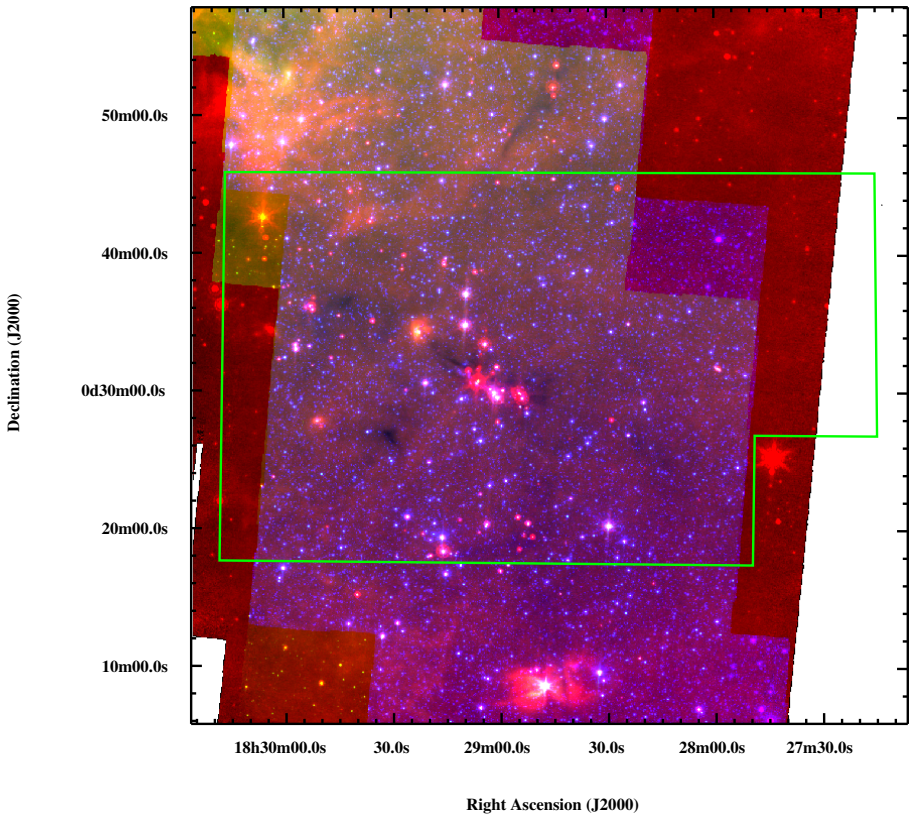

Figure 3.3: Color image of the Serpens cloud made from the 3.6 μm (blue), 8.0 μm (green), and 24 μm (red) channels on *Spitzer*. The green outline denotes the region we observed with our JHK_s observations.

cannot be used in computing changes in the extinction law at mid-infrared wavelengths but are useful in obtaining line-of-sight extinctions.

We initially created high-reliability star catalogs by selecting only those sources classified as stars with both the WD3.1 and WD5.5 dust models. This selection excludes questionable stars which may effect our results, but may also miss bona-fide stars which trace a true change in the extinction law. To check whether this is the case, we created lists of the sources that are only classified as stars with either the WD3.1 or WD5.5 dust models, but not both. Our results for Serpens are shown in Figure 3.4. The stars classified with WD5.5 (green) are strongly associated with the higher extinction regions while the WD3.1 stars (white) are scattered randomly throughout the image. Furthermore, up to a

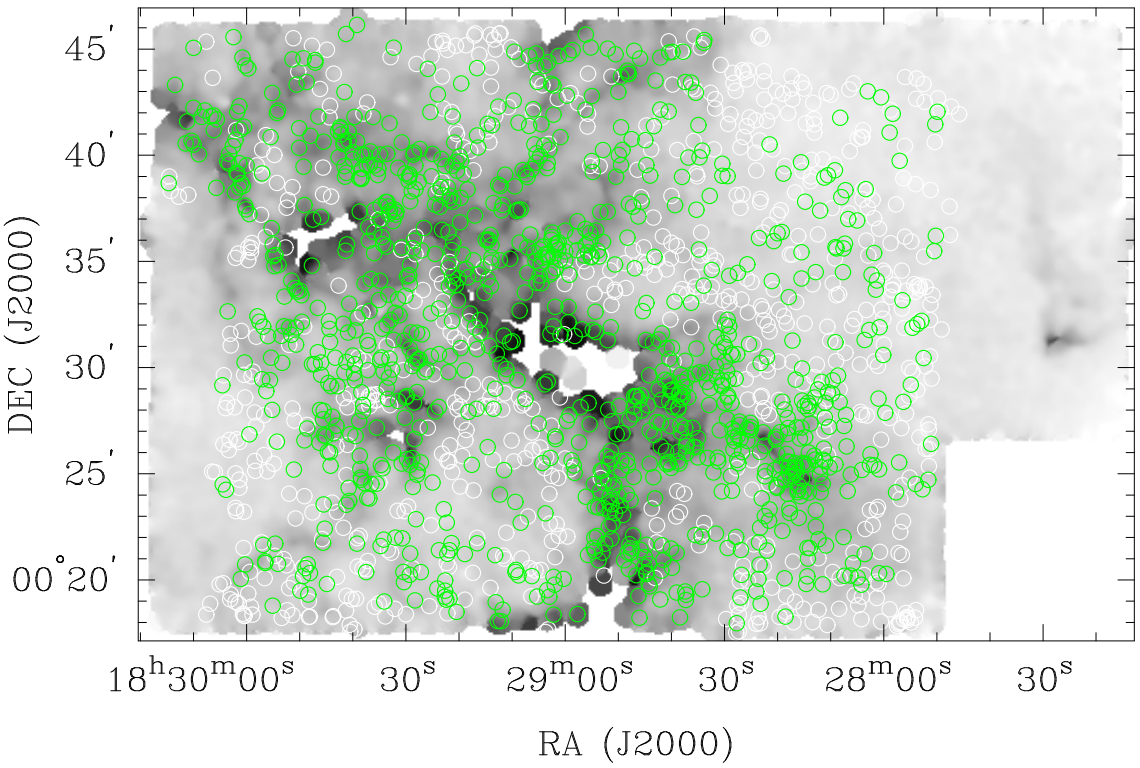

Figure 3.4: Extinction map of Serpens (See § 3.5) with sources identified as stars using only the WD3.1 or WD5.5 dust models. Those stars classified only with the WD5.5 model are shown in green, while those classified with WD3.1 are plotted in white.

third of the detections that are only classified as stars using WD3.1 have a quality flag identifying them as confused with a nearby source suggesting that many of these sources have suspect photometry. In the remainder of the catalog, less than 1% of the sources are similarly confused.

For these reasons, we have selected all sources identified as stars with the WD5.5 dust model and computed line-of-sight extinctions based on this model. The extinctions computed with WD5.5 differ from those computed with a more traditional WD3.1 model by only 1-2%. In this step we also excluded any sources only classified as stars when one of the wavebands was dropped because we did not want to bias our results on the extinction law due to a prominent absorption or emission line. Furthermore, because accurate extinction measurements are essential to this dissertation, we required sources to have a detection $\geq 5\sigma$ in each of the JHK_s bands. Lastly, we 'cleaned' our star catalogs

Table 3.2. Number of Sources in the Clouds

Cloud	Total	3+ bands	JHK_s-only	High Reliability[a]	
				Stars	Cleaned
Ophiuchus	24,671	4,181	59	2,403	2,365
Perseus	83,443	17,114	3815	11,479	11,280
Serpens	100,383	67,783	23,707	49,712	49,485

[a] Sources meeting our high-reliability criteria, § 3.3

Note. — The number of sources in each cloud meeting different selection criteria. The 'stars' and 'cleaned' columns are discussed in § 2.5 and § 3.4.2, respectively.

to remove suspected faint background galaxies. This procedure will be discussed in detail in §3.4.2. In Table 3.2 we list the number of sources in our star catalog for each cloud both before and after removal of faint background galaxies. In this paper whenever we refer to the star catalogs, we will be using the cleaned star catalogs.

3.4 Source Statistics

3.4.1 Comparison to 2MASS

Our 10σ detection limits in the JHK_s bands are 19.5, 18.8, and 17.7 magnitudes, respectively. These limits are $\sim 3.5\times$ deeper than 2MASS in all three bands. The number of JHK_s detections is $2\times$ and $3\times$ larger than 2MASS in Ophiuchus and Perseus, but $6\times$ greater in Serpens, which is towards the Galactic center.

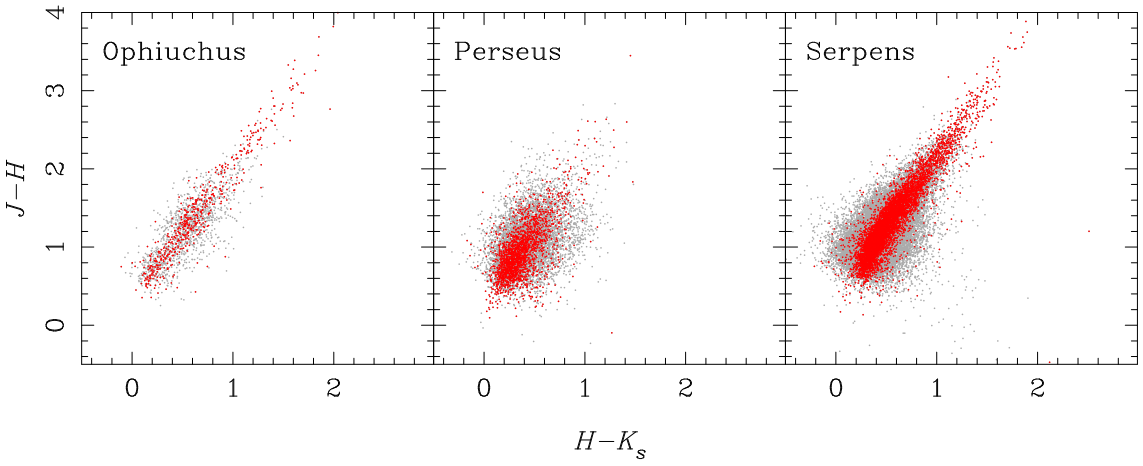

Figure 3.5: Near-infrared color-color diagrams for Ophiuchus, Perseus, and Serpens. We have plotted all stars with uncertainties JHK_s magnitudes ≤ 0.1. Gray points have K_s magnitude > 15 while red points are brighter.

3.4.2 Faint Background Galaxies

Figure 3.5 shows $J-H$ versus $H-K_s$ for our three clouds. In this figure we have only plotted those sources in our high-reliability star catalogs, and only those stars with a magnitude error ≤ 0.1 in all three of the JHK_s bands (roughly 10σ). Those sources brighter than 15th magnitude at K_s are shown in red while fainter sources are gray. We would expect to see extincted stars following a reddening vector which stretches the data points into a line with some scatter (see e.g., Lombardi & Alves 2001). We do see this trend with the red data points in all three clouds and also with the gray points in Ophiuchus and Serpens. This trend is not so clear in Perseus where there are a number of gray sources with $H-K_s \gtrsim 0.7$ and $J-H \lesssim 1.4$ which do not appear to follow the reddening vector.

What is the nature of these sources? One possibility is that these are merely faint stars with bad photometry. It is true that these sources are fainter than 15th magnitude at K_s, however we restricted our plot to sources with detections $\geq 10\sigma$ in the JHK_s bands to ensure good photometry. Upon further examination, we found many of these anomalous sources are only detected in the J-IRAC2 bands. Another possibility, therefore, is that

these sources are not really stars, even though they have been classified as such. Perseus is located at Galactic longitude $l = 160^\circ$, almost in the Galactic anti-center direction, while Ophiuchus and Serpens are located towards the Galactic center at $l = 353^\circ$ and $l = 30^\circ$, respectively. With these Galactic longitudes and given that these anomalous sources are only seen in Perseus, we suspect these sources are likely misidentified background galaxies. The Galactic latitude appears to play little role because Perseus ($b = -19^\circ$) is located at a comparable distance outside of the Galactic plane as Ophiuchus ($b = 16^\circ$), yet Ophiuchus is the most correlated cloud in Figure 3.5.

Our goal in this section is to develop a set of criteria that we will use to separate these suspected faint background galaxies from our actual stars. It is likely that any procedure will remove bona fide stars in addition to background galaxies. We want our criteria to be stringent enough so that the final sample of sources selected for removal will be strongly enriched in background galaxies and contain a minimum number of actual stars. We will then use these procedures to create purified star catalogs which will be used in this dissertation.

To determine whether the sources with anomalous colors really are background galaxies, we need a group of "known" stars and background galaxies to which we can compare. To make these "known" samples, we plotted K_s vs. $K_s - [24]$ for our three cloud regions in Figure 3.6. We only plotted those sources with S/N$\geq 3\sigma$ at 24 μm in addition to the earlier cut (7σ) we made for uncertainties in JHK_s photometry. The shaded contours in each panel are the SWIRE data of ELAIS N1 (Surace et al. 2004) as processed by the c2d team. The ELAIS N1 region is near the north Galactic pole, and therefore we believe the data contain nothing but stars and background galaxies making them useful for selecting stars and galaxies. Based on Figure 3.6 we selected two groups of sources: those with $K_s - [24] \leq 1$ and those sources with $K_s \geq 15$ and $K_s - [24] \geq 4$. We believe the first group contains stars, while the second population contains background galaxies. We will

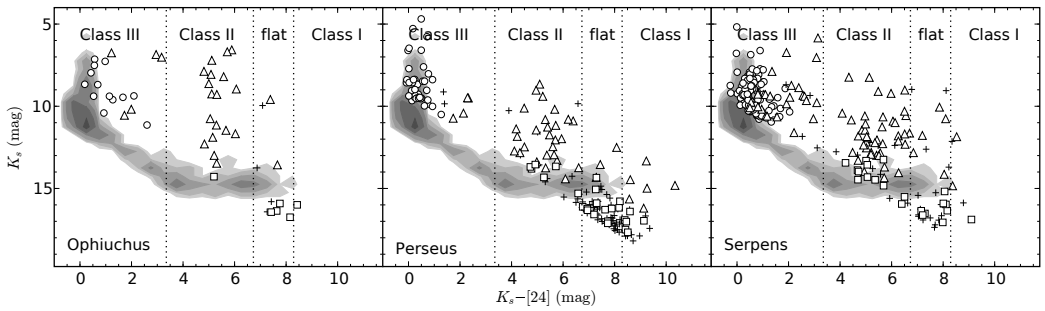

Figure 3.6: K_s vs. $K_s - [24]$ plot for our three clouds. We have used four different symbols to correspond to different source classifications: stars are circles, background galaxies are squares, 'YSO candidates' are triangles, and plus signs denote all other classifications. The vertical lines denote separations between different YSO classes as defined by Greene et al. (1994). The shaded contours are from the c2d processed catalog of part of ELAIS N1 (Surace et al. 2004).

use these groups as our "known" samples.

In Figure 3.7 we overlaid the "known" stars (green) and background galaxies (red) on our $J-H$ vs. $H-K_s$ color-color diagram. There is a rough separation between these two classes of sources. The stars chiefly lie along the stellar reddening vector, while the background galaxies appear below and to the right of this vector, exactly where our anomalous points appear in Perseus. As our first selection criterion, we drew dashed lines to separate stars from galaxies. Note that the separation between the two is not perfect, but does establish that sources with $J-H \geq 0.6$, $H-K_s \geq 0.6$ and to the right of the sloped line are more likely to be galaxies rather than stars. The equation for the sloped line is: $J-H = 1.9 \times (H-K_s) - 0.16$.

As noted earlier, approximately three-fourths of the objects in our clouds that lie in the region selected by our first criterion are only detected in IRAC1 and/or IRAC2. These sources are typically faint enough that they are not detected in the longer wavelengths. In Figure 3.8 we plotted $H-K_s$ vs. $K_s - [3.6]$ and vs. $K_s - [4.5]$. The gray points are those sources selected in all three clouds from Figure 3.7 with $J-H \geq 0.6$, $H-K_s \geq 0.6$, and $J-H \leq 1.9 \times (H-K_s) - 0.16$. Again, green points are stars while red points are

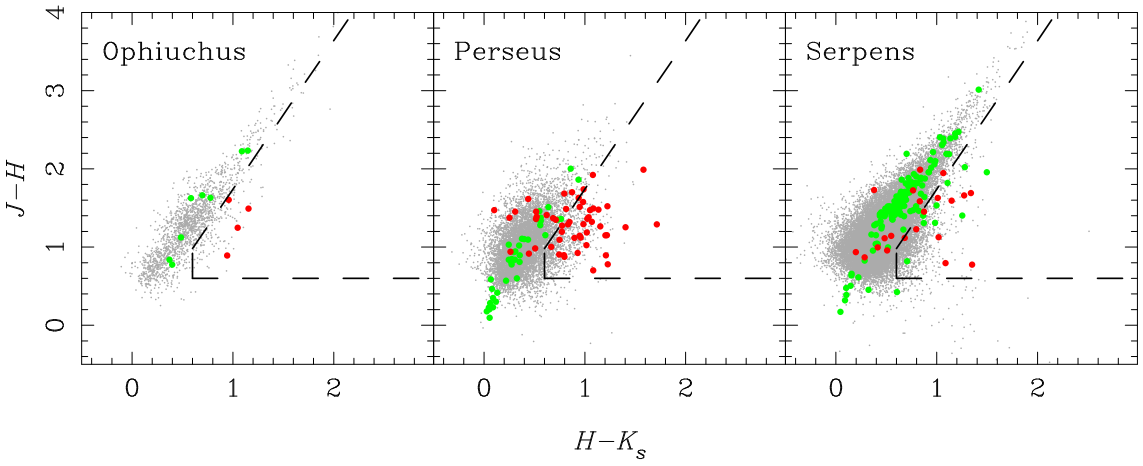

Figure 3.7: Near-infrared color-color diagrams for Ophiuchus, Perseus, and Serpens. Those points classified as stars (§ 2.5) with uncertainties in JHK_s magnitudes ≤ 0.1 are shown in gray. The green points are stars and the red ones are background galaxies. See the text for a discussion on how these sources were selected. The equation for the sloped dashed line is $J-H = 1.9 \times (H-K_s) - 0.16$.

background galaxies. In both of these plots, there is a very clear separation between the stars and galaxies. We have defined a single line to use for both plots: $H-K_s = 1.32x$ where x is either $K_s - [3.6]$ or $K_s - [4.5]$.

Based on Figures 3.7 and 3.8, we have developed two criteria to reduce the number of background galaxies in our data. Starting from the high-reliability "star" catalogs we created in § 3.3, we removed all sources satisfying the following two criteria:

1. $J-H \geq 0.6$, $H-K_s \geq 0.6$, and $J-H \leq 1.9 \times (H-K_s) - 0.16$

2. $H-K_s \leq 1.32 \times (K_s - [3.6])$ and $H-K_s \leq 1.32 \times (K_s - [4.5])$

In Table 3.2 we have listed the number of sources in each star catalog both before and after 'cleaning'. Our cleaning procedure removed 1.6% of the sources in Ophiuchus, 1.8% in Perseus, and 0.5% in Serpens.

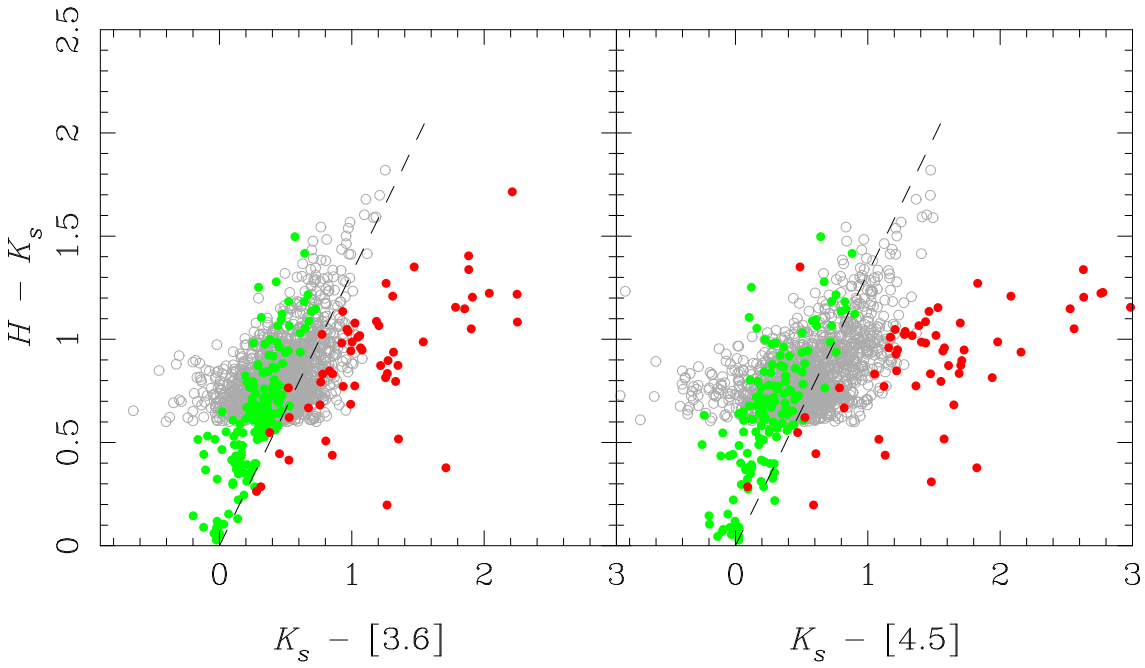

Figure 3.8: $H - K_s$ vs. $K_s - [3.6]$ (left) and vs. $K_s - [4.5]$ (right). The gray points are the sources selected by the dashed lines in Figure 3.7 for Ophiuchus, Perseus, and Serpens. The green points are stars while the red points are background galaxies. See text for discussion of how these sources were selected. The dashed line in each panel has the equation $H - K_s = 1.32x$ where x is either $K_s - [3.6]$ or $K_s - [4.5]$.

3.4.3 Young Stellar Objects and Background Galaxies

Our classification procedure (§ 2.5) also identifies Young Stellar Object candidates (YSOc) and background galaxy candidates (Galc). There are 25, 40, and 74 YSOc sources with JHK_s detections $\geq 7\sigma$ in Ophiuchus, Perseus, and Serpens, respectively. If we normalize per square degree, there are 150, 40, and 220 YSOc objects in each cloud, respectively. The numbers of Galc objects are 6, 25, and 21, or 36, 25, and 63 per square degree for Ophiuchus, Perseus, and Serpens, respectively. The YSOc and Galc objects will be plotted on the extinction maps in the next section.

3.5 Extinction

We have computed extinctions, A_{K_s}, to each source using the NICER technique (Lombardi & Alves 2001) and as described in § 2.5. The line-of-sight (LOS) A_{K_s} values give us a random sampling of the true A_{K_s} in each cloud. To convert these LOS extinctions into a uniform map, we have overlaid a grid on top of the data to represent the cells in the final extinction map. At each grid position, we have utilized all of the LOS extinctions within a given radius. The extinction value in that cell is then the average of the individual extinctions, weighted both by uncertainty and distance from the center of the cell. The equations for the average extinction and uncertainty are:

$$\langle A_{K_s} \rangle = \frac{\sum w^{(i)} A_{K_s}^{(i)}}{\sum w^{(i)}} \tag{3.1}$$

$$\sigma_{A_{K_s}} = \frac{\sqrt{\sum (w^{(i)} \Delta A_{K_s}^{i})^2}}{\sum w^{(i)}} \tag{3.2}$$

$$w^{(i)} = \frac{1}{\Delta A_{K_s}^{(i)2}} \frac{1}{\sigma\sqrt{2\pi}} e^{-2(\theta/2\sigma)^2} \tag{3.3}$$

where θ is the distance in degrees between the center of the cell and each LOS extinction value and σ is the standard deviation of the Gaussian, chosen to create a map with the desired resolution. Note that $\sigma \equiv FWHM/2.3548$ and $FWHM$ is the Full Width Half-Maximum of the Gaussian.

For each cell we chose an integration radius equal to the $FWHM$, or 2.3548σ. All that remains is to choose the appropriate resolution for our maps. We would like to have good statistical accuracy for each cell, so we used a resolution at which there are on average 20+ stars in each cell. For Ophiuchus and Perseus, this corresponds to a $90''$ resolution while in Serpens, which is towards the Galactic center, we were able to make a $30''$ resolution map and still have on average 36 stars per cell.

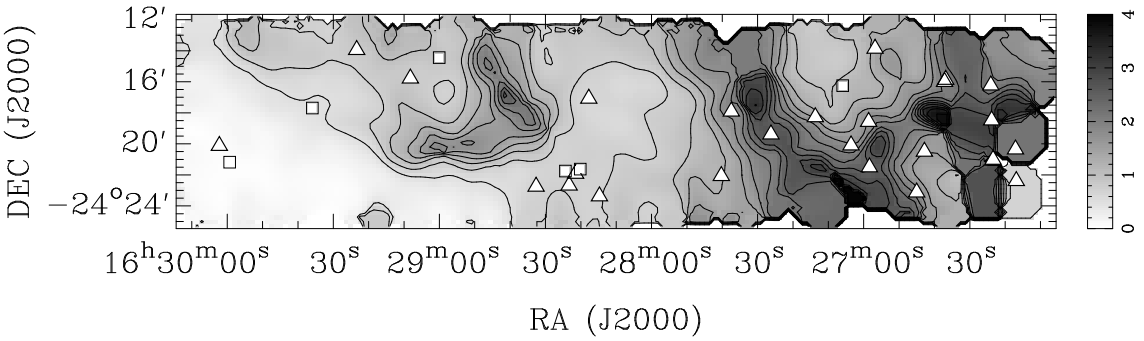

Figure 3.9: A_{K_s} map of our observed region within the Ophiuchus cloud. The map has a resolution of 90″. The contours start at $A_{K_s} = 0.5$ in steps of 0.25 (5σ). We have plotted all the YSOc and Galc objects as triangles and squares, respectively. The maximum A_{K_s} value in the map is 4.0 magnitudes.

Foreground stars can cause problems in regions of high extinction. These sources, which are correctly assigned a very small A_{K_s}, will bias the average value for a given cell. We have dealt with foreground stars as follows: For each cell with more than 2 stars, we compute the mean and median A_{K_s} value. If these two statistics differ by more than 25%, and the average value of A_{K_s} is ≥ 0.75, then we drop the source with the lowest A_{K_s} and recompute the mean and median. If the difference between the old and new mean is less than 25%, we re-add the dropped source to our catalog. The percentage of sources removed in this fashion is less than 1% for Ophiuchus and Serpens and 2% in Perseus.

3.5.1 A_{K_s} Maps

Following the procedure we outlined above, we have constructed extinction maps of Ophiuchus, Perseus, and Serpens (Figures 3.9 - 3.11). The sources classified as either YSOc or Galc have been plotted as triangles and squares, respectively.

Our Ophiuchus region has the largest dynamic range of A_{K_s} values of any of our three regions, up to 4 magnitudes. There is a loop of extinction located at $\sim 16^h28^m30^s$ in addition to the high extinction region L1688 on the western side of the map.

Our Perseus extinction map contains dust filaments in the upper half of the image and

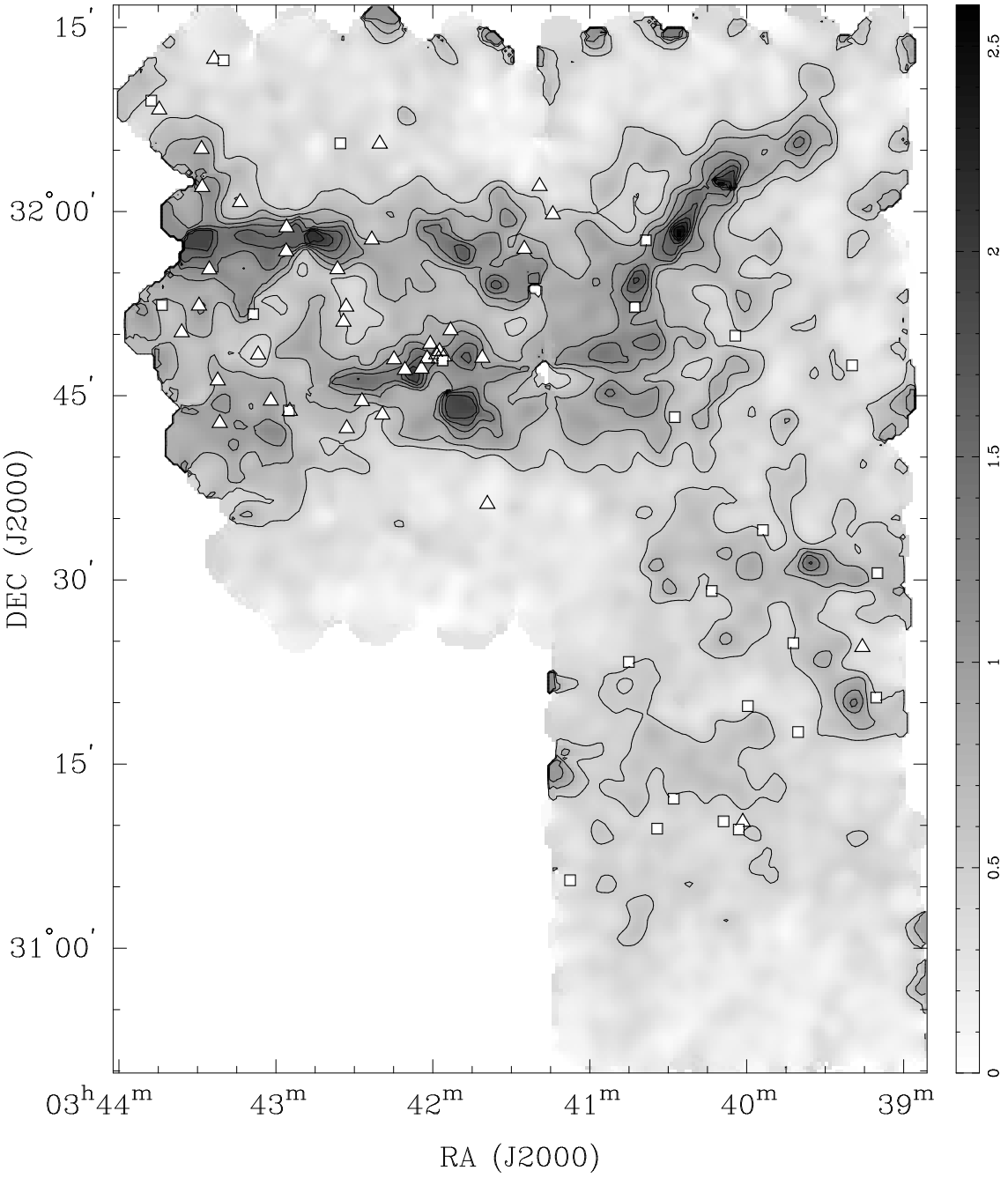

Figure 3.10: A_{K_s} map of our observed region within the Perseus cloud. The map has a resolution of 90″. The contours start at $A_{K_s} = 0.5$ in steps of 0.25 (5σ). We have plotted all the YSOc and Galc objects as triangles and squares, respectively. The maximum A_{K_s} value in the map is 2.6 magnitudes.

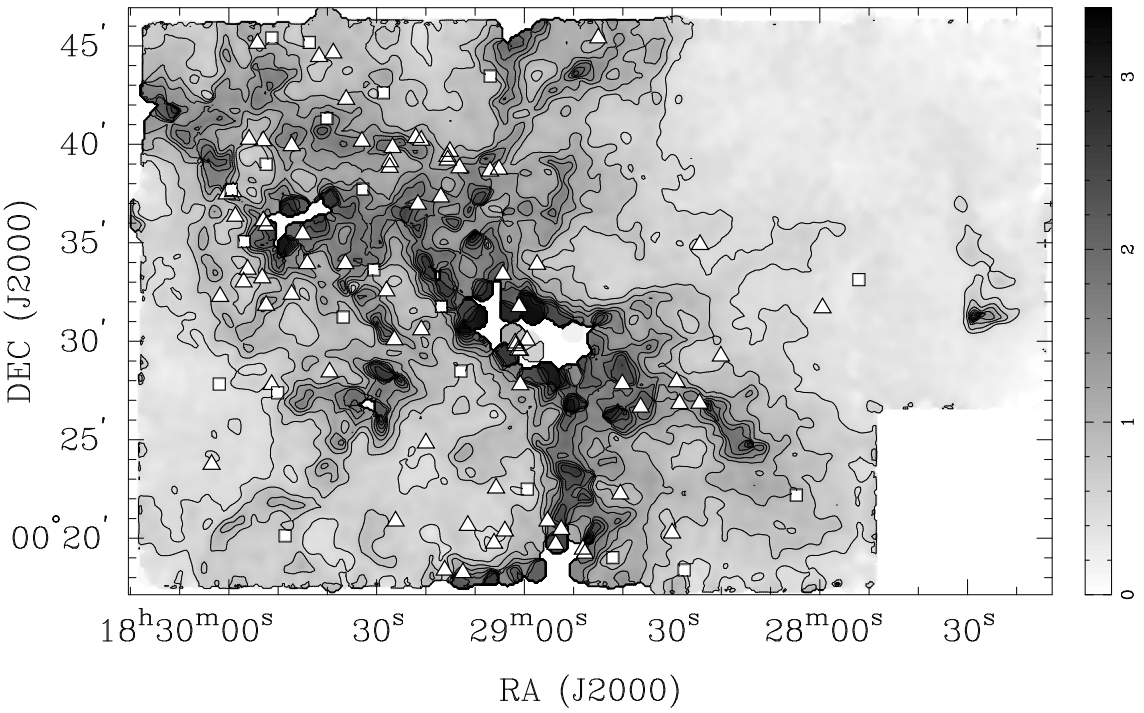

Figure 3.11: A_{K_s} map of our observed region within the Serpens cloud. The "holes" in the map correspond to regions with no data either due to being too dense or because the only sources present were not classified as stars. The map has a resolution of 30″. The contours start at $A_{K_s} = 0.5$ in steps of 0.25 (5σ). We have plotted all the YSOc and Galc objects for Serpens as triangles and squares, respectively. The maximum A_{K_s} value in the map is 3.4 magnitudes.

little extinction above the $A_{K_s} = 0.5$ level elsewhere in the map. There is a cluster of YSOs identified as IRAS 03388+3139 located at RA $\sim 3^h42^m$ DEC $\sim 31°47'$. Furthermore, there is some visual correspondence between high extinction regions and darker patches in the color image (Figure 3.2); the dust lane that crosses the nebulous region of IRAS 03382+3145 ($\sim 3^h41^m30^s$ $+31°55'$) shows up as a high extinction filament in our extinction map (Figure 3.10).

The Serpens map has a higher resolution, 30″, than either Ophiuchus or Perseus due to the greater source density behind the Serpens cloud. There are two dense regions that show up as holes in our maps due to the lack of stellar sources. The larger hole in the center of the map is "Cluster B". The extinction hole located to the West of "Cluster B" shows up as a dark patch in the *Spitzer* images, suggesting this region is extremely dense

to appear opaque in the mid-infrared.

3.5.2 Probability Distribution Function

Simulations of turbulence in molecular clouds have shown that in the limit of isothermal gas distributions where gravity is unimportant, then the density distribution is expected to be log-normal (Padoan et al. 1997; Passot & Vázquez-Semadeni 1998; Vazquez-Semadeni 1994). This observation has been shown to also hold for the column density (Ostriker et al. 2001).

We constructed the probability distribution function (PDF) for our three clouds by taking all of the non-zero pixel values from the extinction maps (Figure 3.9-3.11), binning them in log space with bin size $\Delta \log A_{K_s} = 0.1$, and finally normalizing the histogram. The resultant PDFs can be seen in Figure 3.12. All three clouds show that the PDF is largely log-normal except for a low-extinction tail. The strength of this tail is nearly non-existent in Perseus and Serpens but quite prominent in Ophiuchus. One possible explanation for this behavior is that the temperature decreases at lower densities (Nordlund & Padoan 1999; Passot & Vázquez-Semadeni 1998; Scalo et al. 1998). However, a more prosaic explanation is simply that our maps contain low-extinction off-cloud regions. As a test, when we excluded the low-extinction triangular region in the lower-left corner of the Ophiuchus A_{K_s} map, the tail in the Ophiuchus PDF almost completely disappeared.

3.5.3 Size Scale of Structure

Our extinction maps have resolutions of $90''$ (Ophiuchus and Perseus) and $30''$ (Serpens). These clouds are all at different distances resulting in linear resolutions of 11,250 AU (Ophiuchus), 22,500 AU (Perseus), and 7,800 AU (Serpens). The $90''$ or $30''$ resolution was chosen to create extinction maps with few or no holes and with a reasonable average number of stars per cell for good statistics. We can immediately see the amount of

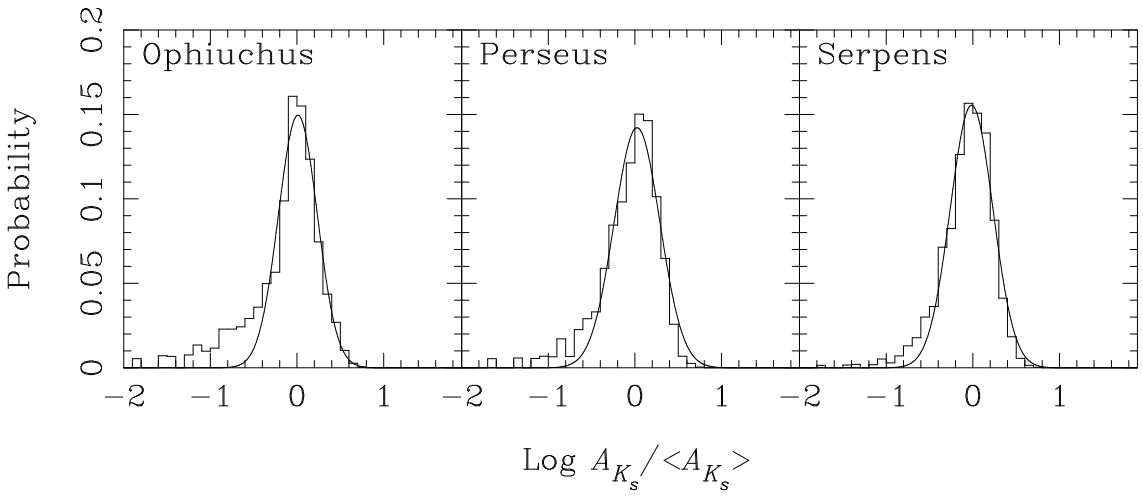

Figure 3.12: The normalized histogram of the line-of-sight extinction values in our clouds. The best-fit Gaussian for each cloud is also plotted.

structure present in our Serpens map (Figure 3.11) as compared to Ophiuchus and Perseus (Figures 3.9 and 3.10).

One method for analyzing dust structure below the resolution of a map is to plot $\sigma_{A_{K_s}} - A_{K_s}$, the standard deviation of A_{K_s} values in a cell versus the average A_{K_s} of that cell. Lada et al. (1994) showed that information about the unresolved substructure can be derived from $\sigma_{A_{K_s}} - A_{K_s}$. If a plot of $\sigma_{A_{K_s}} - A_{K_s}$ has a positive slope, then this indicates unresolved structure which may be either random spatial fluctuations or a density gradient in the cloud (Lada et al. 1999). Padoan et al. (1997) has showed the $\sigma_{A_{K_s}} - A_{K_s}$ relationship is the expected result for clouds with supersonic turbulence.

In Figure 3.13 we have plotted $\sigma_{A_{K_s}} - A_{K_s}$ for our clouds. We constructed these figures by comparing, for each pixel, the standard deviation of the A_{K_s} measurements in the cell with the average value of A_{K_s}. We then binned these measurements in A_{K_s}. Each panel represents a different map resolution, either 30, 45 ,60, or $90''$.

All three clouds show a definite slope at $90''$ and $60''$ resolution. At $45''$, Ophiuchus and Perseus appear flat for $A_{K_s} \leq 1$. Finally, at $30''$, Ophiuchus and Perseus are relatively flat for $A_{K_s} \leq 2$. Above this limit, Perseus rises sharply and Ophiuchus may also exhibit a

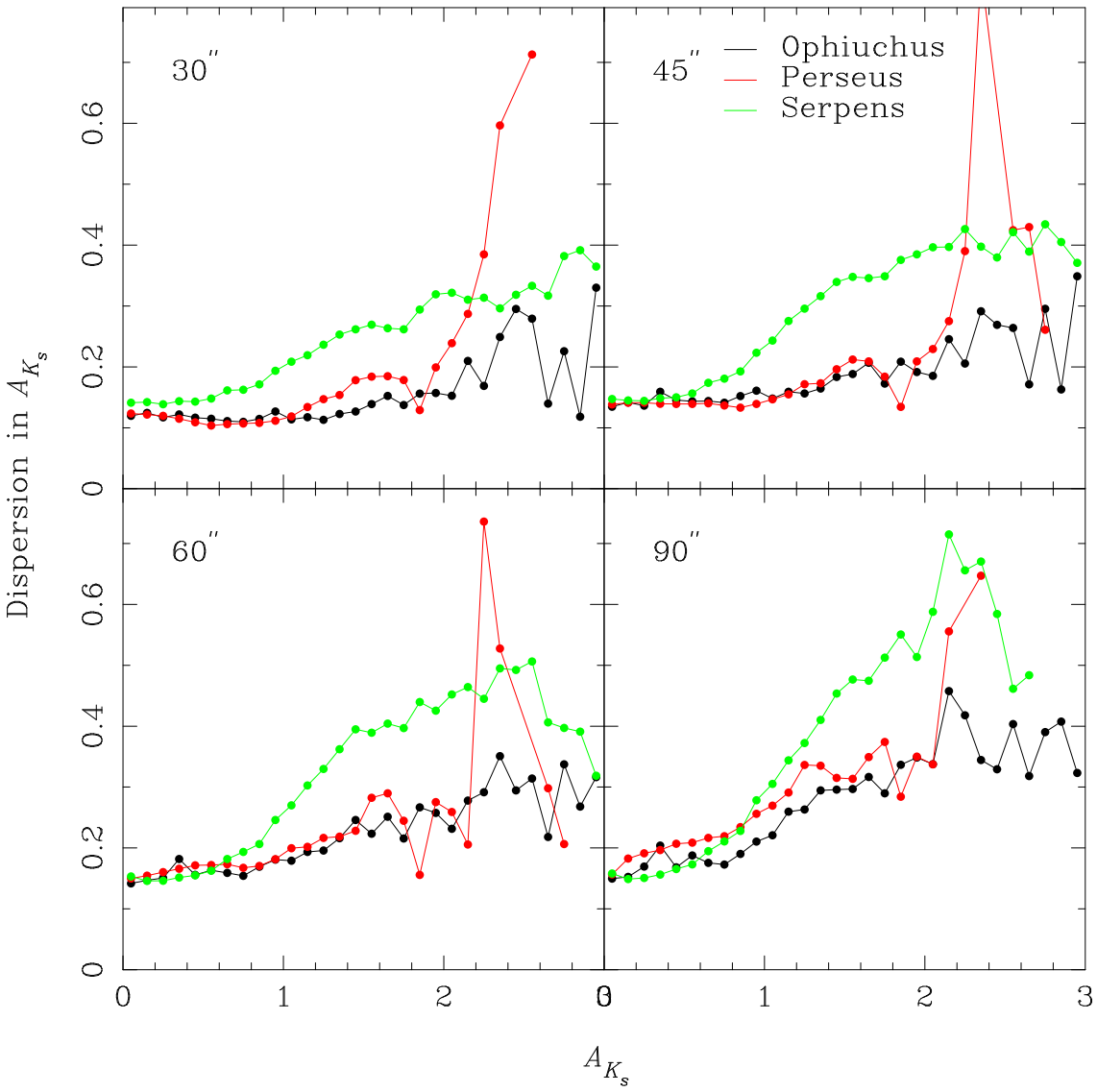

Figure 3.13: The standard deviation of A_{K_s} versus A_{K_s} for the clouds. The values were derived from extinction maps made at with four different resolutions: 30, 45, 60, and 90″. We have binned our data in A_{K_s} to make the plot clearer.

rise in $\sigma_{A_{K_s}}$. Less than 0.1% of the cells in Perseus, have $A_{K_s} \geq 2$, so small number statistics may be dominating the relationship in this cloud. The Serpens $\sigma_{A_{K_s}} - A_{K_s}$ distribution has a positive slope at all resolutions.

The change in the slope of the $\sigma_{A_{K_s}} - A_{K_s}$ relation is consistent with numerous other observational results (Alves et al. 1998; Lada et al. 1999, 2004, 1994; Lombardi et al. 2006). As we decrease the resolution from 90″ to 30″, we see that the slope flattens

suggesting that some of the dust structure is being resolved at higher resolution. Lada et al. (1999) found that the $\sigma_{A_{K_s}} - A_{K_s}$ relationship could also be entirely explained by a r^{-2} density profile in the IC 5146 dust filament. It is beyond the scope of this paper to explore whether this scenario is plausible in our clouds. Our results do not appear to fit the prediction for supersonic turbulence (Padoan et al. 1997). Padoan et. al. showed that supersonic turbulence would lead to a log-normal density distribution on all spatial scales and therefore the slope would be expected to remain constant (see e.g. Lada et al. 1999).

3.6 Dust Properties

Up to this point, we have concentrated solely on the *quantity* of dust along each line-of-sight. From this, we have studied the structure within the clouds. However, we have ignored the properties of the dust itself. We now turn to this important problem.

Many authors have fit the near-infrared extinction to a power law, $A_\lambda \propto \lambda^{-\beta}$, with $\beta = 1.6 - 1.8$ (Draine 2003, and references therein). Many of these studies have been restricted to low extinction (e.g. Cardelli et al. 1989, with $A_V \lesssim 5$) although Moore et al. (2005) measured the extinction law from $1 - 2.2\,\mu$m towards nine ultra-compact H II regions with $A_V \gtrsim 15$ to address this bias. The authors found no evidence for a steeper extinction law than $\beta = 1.8$. The Weingartner & Draine $R_V = 3.1$ and $R_V = 5.5$ models are very similar in the near-infrared JHK_s bands, reflecting this apparent universality of the near-infrared extinction law. We will exploit the constancy of the extinction law in the near-infrared by using the extinctions computed from the JHK_s bands and then extrapolating the extinction law to the *Spitzer* wavebands.

Starting from our basic equation relating flux and extinction,

$$\log(F_{obs}(\lambda)/F_{model}(\lambda)) = \log(K) - 0.4 \times C_{ext}(\lambda) \times A_{K_s} \tag{3.4}$$

we can re-arrange this to solve for C_{ext}, defined as A_λ / A_{Ks}:

$$C_{ext}(\lambda) = \frac{2.5}{A_{K_s}}[\log(K) - \log(F_{obs}(\lambda)/F_{model}(\lambda))] \tag{3.5}$$

At this point, we are still stuck because we do not know K, the scaling factor for distance, nor F_{model}, the best fit stellar model for each source. We do not want to fit the JHK_s bands to find these parameters since this technique may provide inaccurate values as we found is the case for the extinction (§ 2.6). However, since we are only interested in *differences* in the extinction law, we can subtract $C_{ext}(K_s)$ to eliminate the need for K:

$$\begin{aligned} C_{ext}(\lambda) - C_{ext}(K_s) &= \frac{2.5}{A_{K_s}}[\log(K) - \log(F_{obs}(\lambda)/F_{model}(\lambda))] \\ &\quad - \frac{2.5}{A_{K_s}}[\log(K) - \log(F_{obs}(K_s)/F_{model}(K_s))] \end{aligned} \tag{3.6}$$

Since $C_{ext}(K_s) \equiv 1$ and $F_{model}(K_s) \equiv 1$ (all stellar models are scaled relative to K_s), this can be simplified:

$$C_{ext}(\lambda) = \frac{2.5}{A_{K_s}}[\log(F_{obs}(K_s)/F_{obs}(\lambda)) + \log F_{model}(\lambda)] + 1 \tag{3.7}$$

Finally, the uncertainty in C_{ext} can be found via propagation of errors:

$$\begin{aligned} \Delta C_{ext}(\lambda) &= \frac{2.5}{A_{K_s}}\left[\left(\frac{C_{ext}(\lambda)-1}{2.5}\right)^2 \sigma^2_{A_{K_s}} + \left(\frac{\sigma F_{obs}(K_s)}{F_{obs}(K_s)\ln 10}\right)^2 + \right. \\ &\quad \left. \left(\frac{\sigma F_{obs}(\lambda)}{F_{obs}(\lambda)\ln 10}\right)^2 + \left(\frac{\sigma F_{model}(\lambda)}{F_{model}(\lambda)\ln 10}\right)^2\right]^{0.5} \end{aligned} \tag{3.8}$$

For F_{model} we will use the average cloud stellar model derived in § 2.7. This model is weighted based on the expected stellar distribution (Jarrett 1992; Jarrett et al. 1994) and detectability.

3.6.1 χ^2 in the Clouds

We would like to construct a two-dimensional map of the changes in the dust properties across a cloud. We will do this by computing a reduced χ^2 value along each line-of-sight, and then applying the same method we used to create A_{K_s} maps, except this time our "extinction" values will be χ^2 values. We define χ^2 as the sum of the difference between our computed extinction law and a theoretical model over the *Spitzer* IRAC wavebands ($3.6-8\,\mu$m). The reduced χ^2 is then simply χ^2 divided by the number of bands summed minus 1, since we have 1 free parameter in the model, namely A_{K_s}:

$$\chi^2 = \frac{1}{n-1}\sum_{\lambda}^{n}\left(\frac{C_{ext}^{obs}(\lambda) - C_{ext}^{model}(\lambda)}{\sigma_\lambda}\right)^2 \tag{3.9}$$

$C_{ext}^{obs}(\lambda)$ is computed from Equation 3.7, C_{ext}^{model} is the extinction law for a given dust model, and σ_λ is the uncertainty in C_{ext}^{obs}. In this paper, whenever we will refer to "χ^2", we are actually referring to the reduced χ^2 as defined by Equation 3.9. We have used both the WD3.1 and WD5.5 dust models in creating our χ^2 maps. Note that we have only summed over the IRAC bands. As we shall see later, the extinction law at $24\,\mu$m is typically much higher than either the WD3.1 or WD5.5 extinction models (§ 3.6.2). We do not want to bias our results based on those data, so we have excluded this data point when calculating the reduced χ^2. Finally, we excluded any negative values for C_{ext}^{obs} as unphysical.

We created a map of the χ^2 values using the same process we used for extinction mapping and with the same resolution. Our χ^2 maps for Ophiuchus, Perseus, and Serpens can be seen in Figures 3.14 - 3.16. We have drawn our contours starting at $\chi^2 = 4$ because this is the approximate level at which there is a definite transition between the WD3.1 and WD5.5 dust models (see Figure 3.17). Further, with one degree of freedom there is approximately a 5% chance that $\chi^2 = 4$ would arise by chance. This probability decreases with more degrees of freedom.

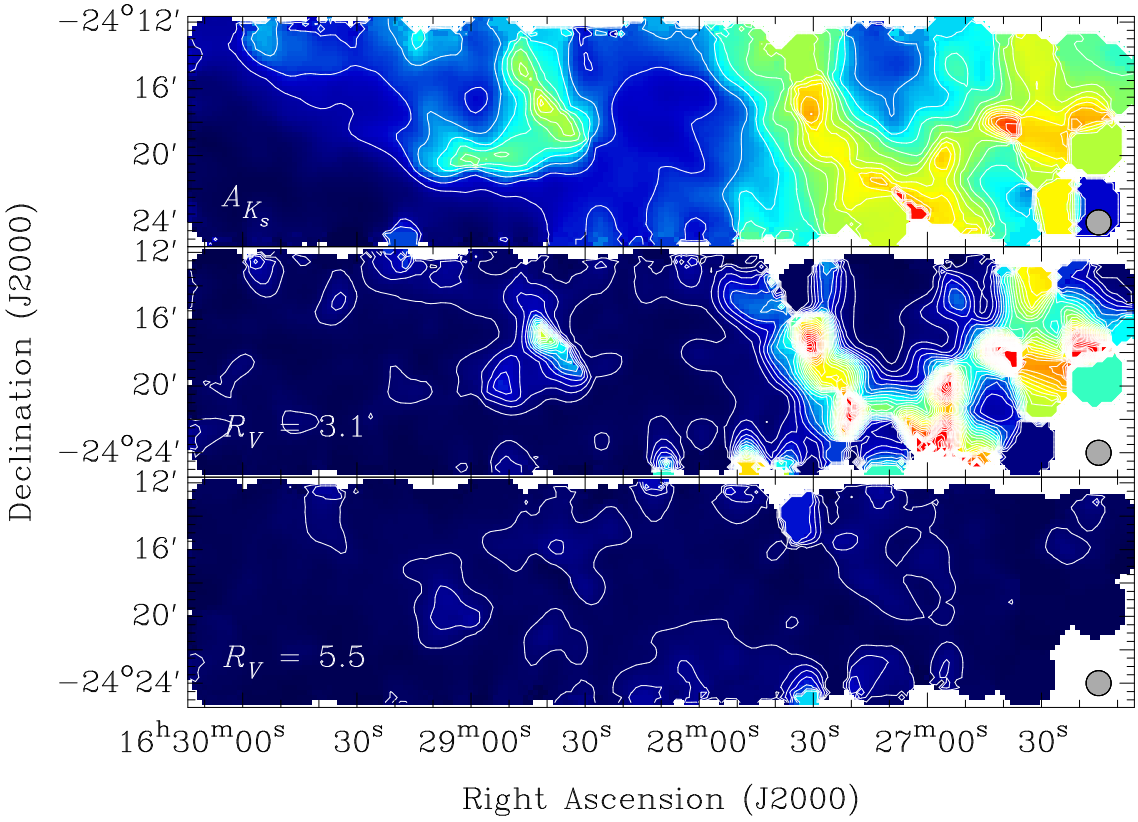

Figure 3.14: Map of the A_{K_s} and χ^2 values in Ophiuchus. The top panel shows the A_{K_s} map with contours starting at 0.5 magnitudes in steps of 0.25 mag (5σ). The middle and bottom panels show the χ^2 maps for the same region made assuming either the WD3.1 (middle) or WD5.5 (bottom) extinction laws. Contours start at 4 in steps of 4.

In broad terms, there is a correlation between high extinction and large χ^2 in our $R_V = 3.1$ maps. The same correlation is not seen with $R_V = 5.5$. To make a quantitative comparison between χ^2 and A_{K_s}, we binned our data in $A_{K_s}$and for each bin determined the average χ^2 with both the WD3.1 and WD5.5 models. Our results are shown in Figure 3.17. The $R_V = 3.1$ χ^2 curve is shown in black while $R_V = 5.5$ is shown in gray. At low extinction, $A_{K_s} \lesssim 1$, the $R_V = 3.1$ and 5.5 curves are very similar suggesting it is difficult to distinguish between dust models at low extinctions. This explains why most of low A_{K_s} regions in Figures 3.14 - 3.16 appear very similar in both the WD3.1 and WD5.5 χ^2 maps. Above $A_{K_s} \approx 1$, the $R_V = 3.1$ curve rises sharply while $R_V = 5.5$ either decreases or stays roughly constant.

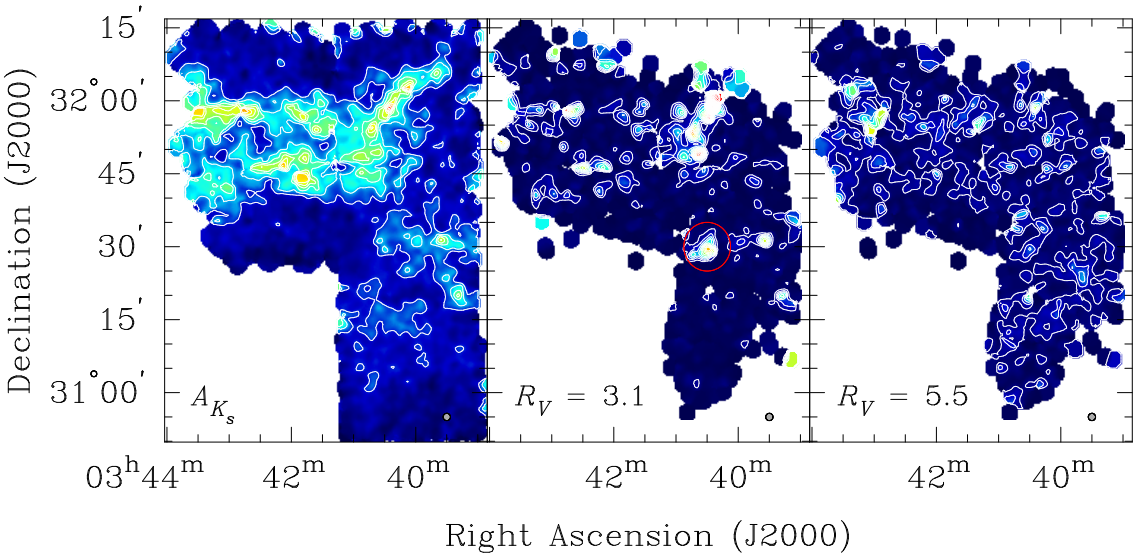

Figure 3.15: Map of the A_{K_s} and χ^2 values in Perseus. The left panel shows the A_{K_s} map with contours starting at 0.5 magnitudes in steps of 0.25 mag. (5σ). The middle and right panels show the χ^2 maps for the same region made assuming either the WD3.1 (middle) or WD5.5 (right) extinction laws. Contours start at 4 in steps of 4. The region circled in red is discussed in the text.

The correlation between high A_{K_s} and high χ^2 is not surprising since it is consistent with the idea of grain growth in denser regions leading to a different extinction law. This same behavior was found by Kandori et al. (2003) in the L1251 cloud. This correlation is not always strictly observed. There is one small region within the Perseus $R_V = 3.1$ χ^2 map where this correlation does not hold. This region is located at $\sim 3^{\rm h}40.5^{\rm m}$ $+31°30'$ and circled in red in Figure 3.15. This region has a peak χ^2 value of 39, but since it is non-circular and larger than the integration radius, it seems unlikely that there is a single bad data point affecting the χ^2. The most puzzling thing about this region is that the extinction is fairly unremarkable suggesting that grain growth may not be causing the increase in χ^2. However, other dust features, such as ice on dust grains may be causing the anomalous χ^2. In the next section, we explore changes in the observed extinction law as a function of wavelength and A_{K_s}. This will help us to understand regions such as the one in Perseus.

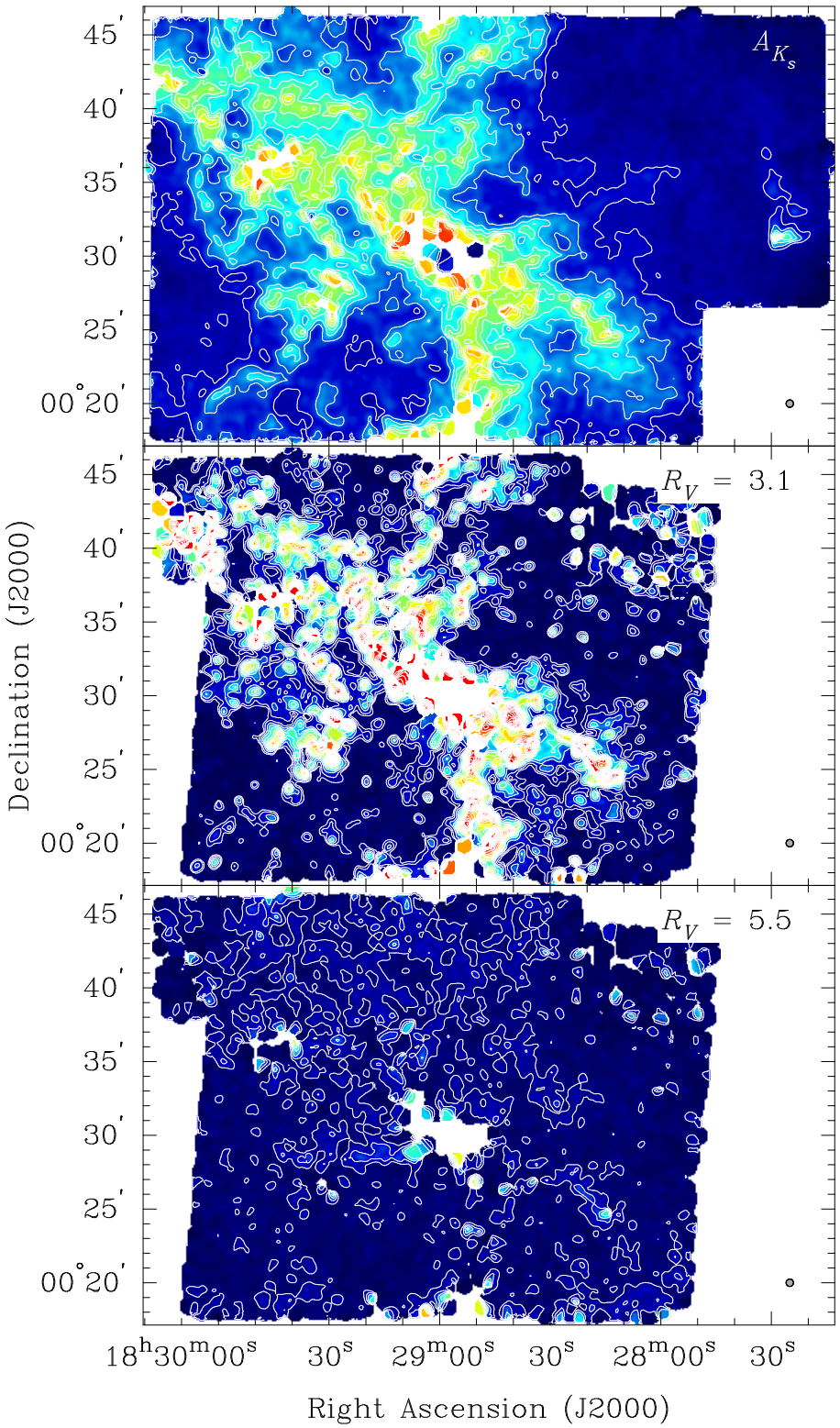

Figure 3.16: Map of the A_{K_s} and χ^2 values in Serpens. The top panel shows the A_{K_s} map with contours starting at 0.5 magnitudes in steps of 0.25 mag. (5σ). The middle and bottom panels are the χ^2 maps for the same region made assuming either the WD3.1 (middle) or WD5.5 (bottom) extinction laws. Contours start at 4 in steps of 4.

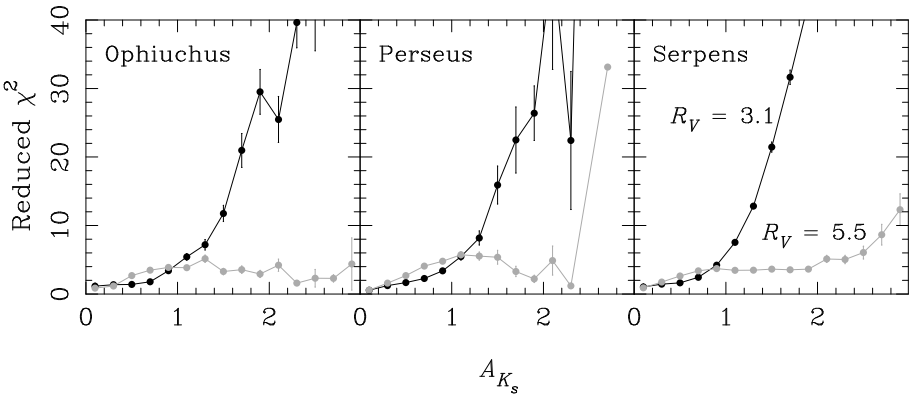

Figure 3.17: χ^2 versus A_{K_s} for the clouds we observed. The WD3.1 χ^2 values are black, while the WD5.5 χ^2 values are light gray. The error bars shown are the standard deviations of the mean χ^2 value in each bin.

3.6.2 The Mid-Infrared Extinction Law

We have line-of-sight measurements of A_{K_s} and the extinction law for every star within our clouds. In the previous section, we turned these measurements into a map of the χ^2 deviation from either the WD3.1 or WD5.5 extinction laws. Now we would like to explore what the extinction law actually is as a function of wavelength and A_{K_s}. We have started by binning our line-of-sight measurements into four A_{K_s} ranges from low to high: $0.15-0.5$, $0.5-1$, $1-2$, and ≥ 2. For each bin, we excluded any negative C_{ext}^{obs} values as unphysical. Our results for the three clouds can be seen in Figures 3.18 - 3.20. The errorbars in each bin are the larger of either the standard deviation of the mean or the minimum uncertainty due to systematic errors in measuring fluxes. To compute the systematic error, we used Equation 3.8 and ignored the first term which is due to uncertainties in A_{K_s}. The final three terms are the uncertainty in flux at K_s, λ, and for the average stellar model. We used the uncertainties quoted in §§ 2.4.1 and 2.4.2 and in Table 2.4 to compute the systematic uncertainty at each wavelength. Note that the uncertainty is proportional to $A_{K_s}^{-1}$. We used the average value for A_{K_s} in each bin, weighted by our uncertainties in C_{ext}, to compute the systematic errors.

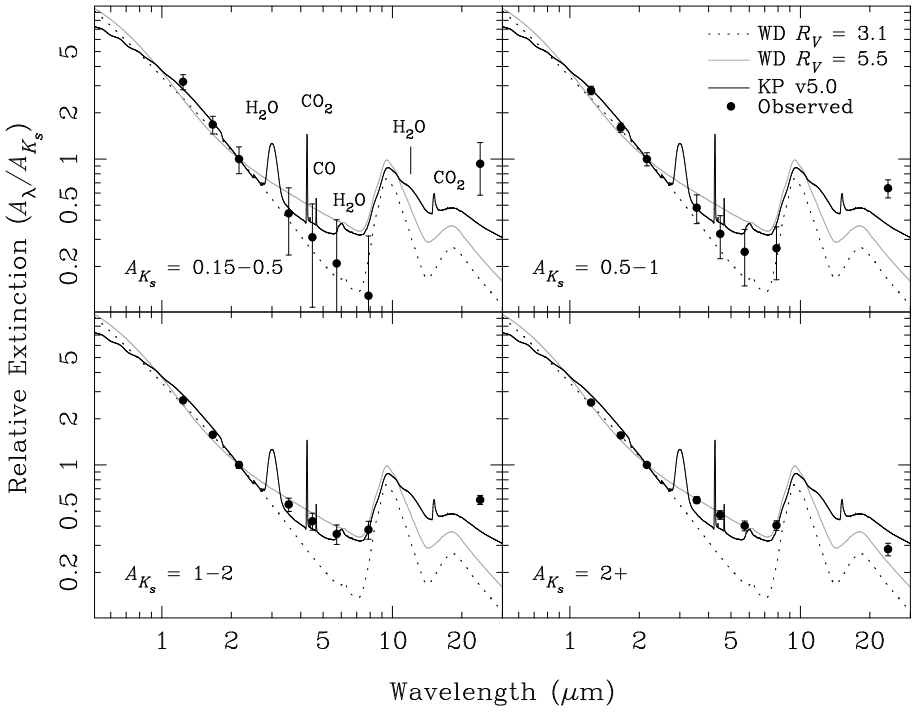

Figure 3.18: The extinction law in Ophiuchus in four different A_{K_s} ranges: 0.15-0.5, 0.5-1, 1-2, 2+. The data points are the average observed extinction law computed from all sources within the specified A_{K_s} range where the errorbars are the larger of: the standard deviation of the mean or the minimum uncertainty due to systematic errors in the flux. We have plotted three different dust models for comparison: Weingartner & Draine $R_V = 3.1$ and 5.5 (dotted, gray lines), and KP v5.0 (Pontoppidian et al., in prep) in black. Using Gibb et al. (2004) as a reference, we have identified the ice features in KP v5.0.

We plotted three theoretical extinction laws in our figures. The WD $R_V = 3.1$ and WD $R_V = 5.5$ models are the same WD3.1 and WD5.5 models we used in computing the χ^2. In addition to those two, we plotted a third model, labeled KP v5.0 (Pontoppidian et al., in prep). This dust model utilizes a simplified version of the WD3.1 dust model and adds icy mantles of water and other volatiles. Several ice absorption features can be seen in the figures, these are due to H_2O, CO_2, or CO.

The observed $3.6-8\,\mu$m extinction laws in all three clouds show a similar trend: At low A_{K_s}, the extinction law is more consistent with the WD3.1 law while at higher extinctions the observed law gradually flattens to become more consistent with WD5.5. At the lowest extinctions, $A_{K_s} = 0.15-0.5$, the extinction law from $3.6-8\,\mu$m is fairly

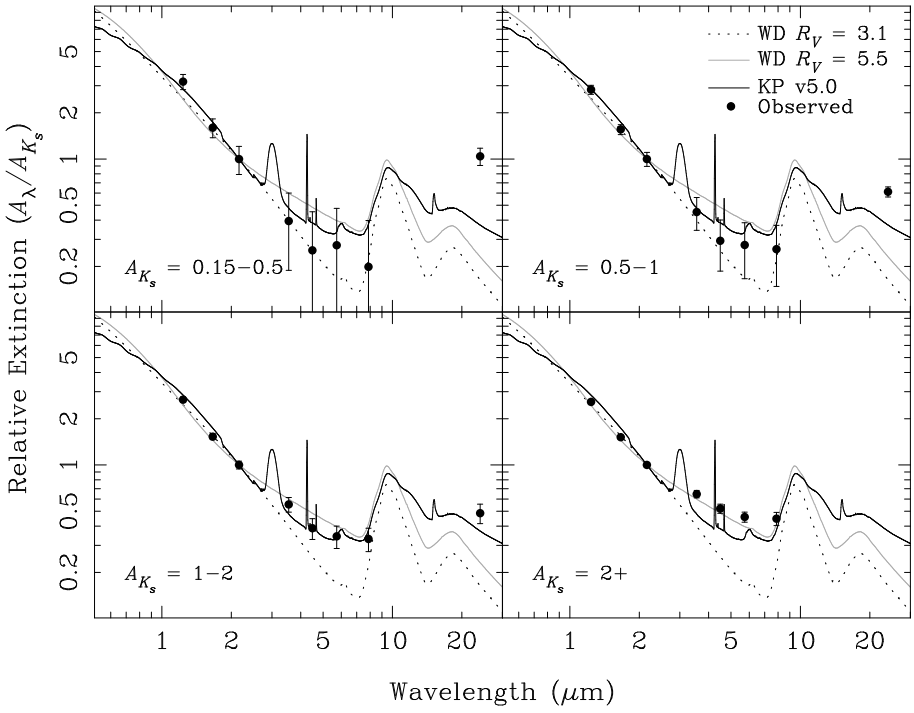

Figure 3.19: The extinction law in Perseus in four different A_{K_s} ranges: 0.15-0.5, 0.5-1, 1-2, 2+. The data points are the average observed extinction law computed from all sources within the specified A_{K_s} range where the errorbars are the larger of: the standard deviation of the mean or the minimum uncertainty due to systematic errors in the flux. We have plotted three different dust models for comparison: Weingartner & Draine $R_V = 3.1$ and 5.5 (dotted, gray lines), and KP v5.0 (Pontoppidian et al., in prep) in black.

consistent with the WD3.1 dust model except at $5.8\,\mu$m in Perseus and Serpens. However, the $A_{5.8}/A_{K_s}$ data point is not statistically significant since our systematic errors in flux lead to very large errorbars at low A_{K_s}. At higher A_{K_s}, the extinction law flattens towards the WD5.5 model and the systematic errorbars shrink too, since they are proportional to $A_{K_s}^{-1}$. Even though the systematic errors can be quite large, the relative systematic uncertainties between the bands are much smaller. In Ophiuchus, the data for $A_{K_s} \geq 2$ are very close to the WD5.5 dust model while in Perseus and Serpens the extinction law is flatter than predicted by WD5.5.

The extinction law we observe at high A_{K_s} is comparable to other results. In Figure 3.21 we have plotted our observed law for Serpens along with the results from several other surveys. (Lutz 1999) measured Hydrogen recombination lines towards the Galactic

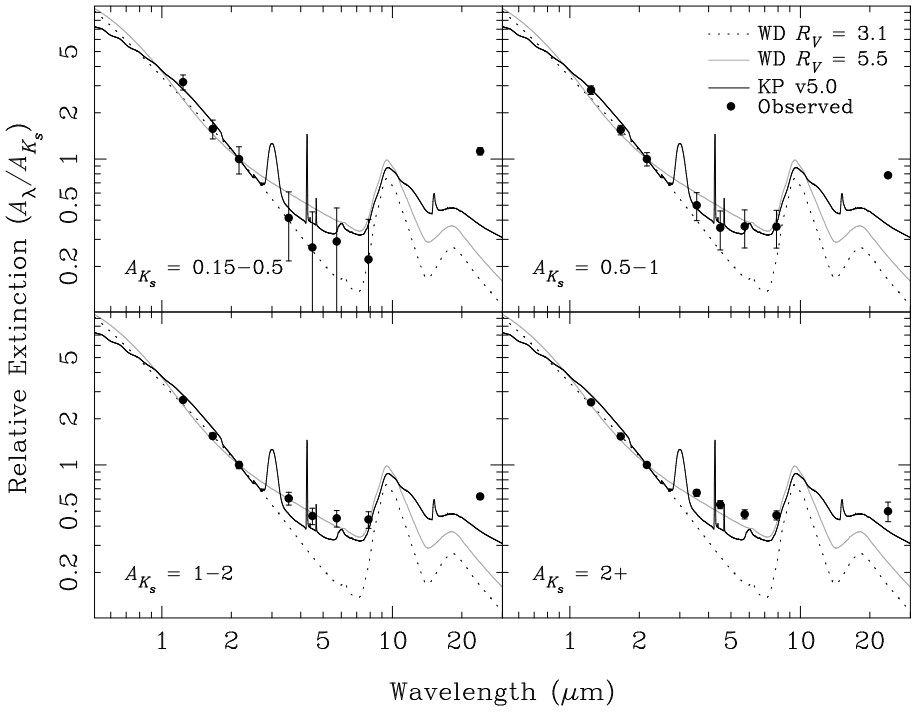

Figure 3.20: The extinction law in Serpens in four different A_{K_s} ranges: 0.15-0.5, 0.5-1, 1-2, 2+. The data points are the average observed extinction law computed from all sources within the specified A_{K_s} range where the errorbars are the larger of: the standard deviation of the mean or the minimum uncertainty due to systematic errors in the flux. We have plotted three different dust models for comparison: Weingartner & Draine $R_V = 3.1$ and 5.5 (dotted, gray lines), and KP v5.0 (Pontoppidian et al., in prep) in black.

center to compute the extinction law from $2.6 - 19\,\mu$m. Indebetouw et al. (2005) used the IRAC instrument on-board *Spitzer* and measured the extinction law along two lines of sight using data from the GLIMPSE *Spitzer* Legacy Science program (Benjamin et al. 2003). The authors found their extinction law was in good agreement with the Lutz (1999) results. Finally, Flaherty et al. (2007) also used *Spitzer* to measure the extinction law toward five different regions, including small parts of the c2d observations of Serpens and Ophiuchus. Their average results are slightly higher than the Lutz et al. or Indebetouw et al. values, but within the errorbars. All of these results are consistent with the idea of grain growth in dense regions (represented by the WD5.5 model). The extinction law in the denser regions of Perseus and Serpens appears flatter than WD5.5, primarily due to the $5.8\,\mu$m data point. This can be explained by the presence of the $6.02\,\mu$m water ice

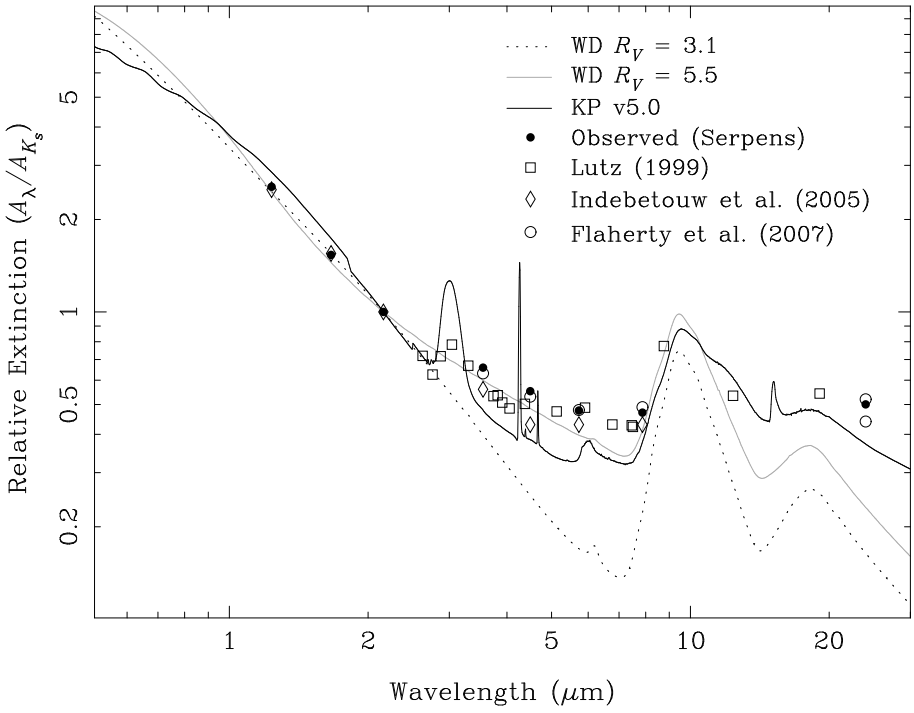

Figure 3.21: The extinction law measured by three different authors along with theoretical models. Our average extinction law for our Serpens data with $A_{K_s} \geq 2$ is shown with black circles. For clarity, we have suppressed the errorbars.

feature (as can be seen in the KP v5.0 dust model).

The extinction law at 24 μm is generally higher than that predicted by any of the three dust models. This means there is more extinction for a given column density, or alternatively, our observed 24 μm fluxes are fainter than models predict. The exact value of A_{24}/A_{K_s} ranges from 0.28 to 1.1 and varies between clouds and extinction bins. For most ranges of extinction, A_{24}/A_{K_s} is much higher than the value predicted by any extinction model. This discrepancy is the reason why we excluded the 24 μm data when creating our χ^2 maps in § 3.6.1.

There are fewer results available from other authors on the extinction law at 24 μm. Neither Lutz (1999) nor Indebetouw et al. (2005) observed at 24 μm. Flaherty et al. (2007) did measure A_{24}/A_{K_s} for two of their five regions. Only in these regions were there enough data points for them to measure the slope of $H-K_s$ versus $K_s-[24]$. They

found $A_{24}/A_{K_s} = 0.44 \pm 0.02$ and 0.52 ± 0.03 for Serpens and NGC2068/71, respectively. Rosenthal et al. (2000) measured H_2 rotational lines towards OMC-1 and obtained an extinction law that covers 24 μm with a value of $A_{24}/A_{K_s} \sim 0.45$ (interpreted from their Figure 6). Our values of A_{24}/A_{K_s} vary significantly between different clouds and ranges of extinction. In all three clouds, they are highest at low extinctions and decrease as A_{K_s} increases. In most cases, A_{24}/A_{K_s} is significantly higher than any model predicts by a factor of $3-5$. The only exception to this is for the $A_{K_s} = 2+$ point in Ophiuchus which is only marginally higher than the predicted value from WD5.5. However, this value is computed from just 2 stars. One possible explanation for these A_{24}/A_{K_s} data points is that the average stellar model at 24 μm is incorrect. From Table 2.4 we see that the model for clouds lists an average flux of 0.014 ± 0.001 mJy (scaled relative to K_s). As a test, we used a smaller average flux of 0.012 in Serpens and our values for A_{24}/A_{K_s} were reduced dramatically. The effect was largest (-54%) for $0.15 \leq A_{K_s} < 0.5$, and smallest (-23%) at high extinction ($A_{K_s} \geq 2$). Even so, our A_{24}/A_{K_s} data points are almost always higher than any current dust models, but are roughly consistent at higher extinctions with previously observed values.

Finally, the anomalous region in Perseus has 57 stars within the region defined by the $\chi^2 = 4.0$ contour. We plotted these in Figure 3.22. The extinction law for these data is more consistent with that observed in the densest regions of Perseus and Serpens. The data points lie above the WD5.5 model and the largest deviation occurs at 5.8 μm, where $A_{5.8}/A_{K_s}$ is higher than any of the extinction laws we have plotted. The water ice feature at 6.02 μm may explain the discrepancy, however ices are seen towards dense cores and the average extinction for this region is relatively modest ($A_{K_s} = 0.62$) (Gibb et al. 2004; Knez et al. 2005). Another possibility is that the sources in this region do not fit the average stellar model. The star would have to all be very young and massive since the stellar model fluxes tend to rise towards later spectral types and higher model fluxes would

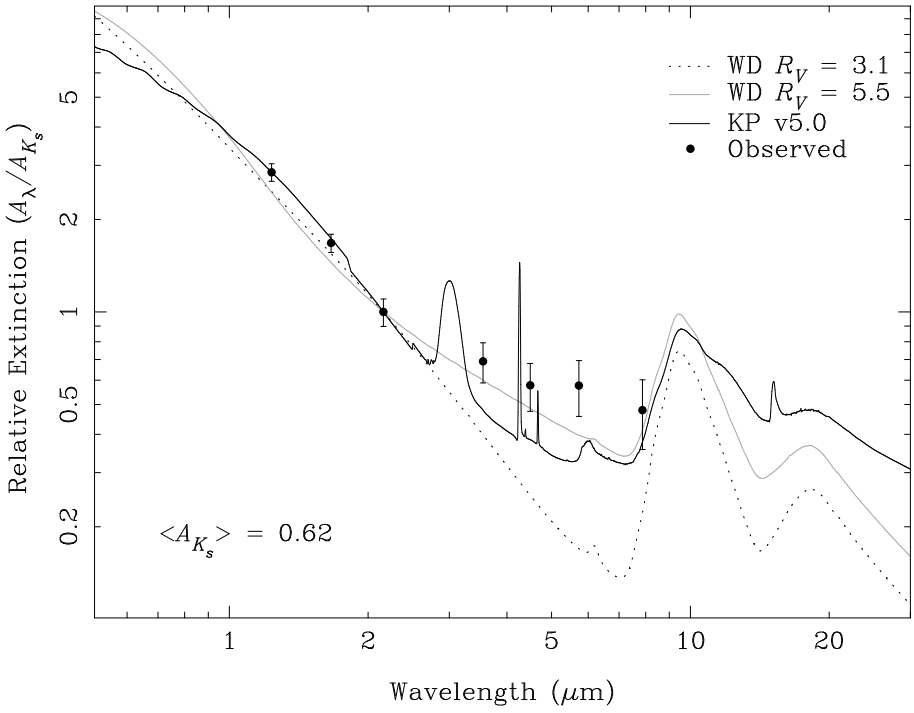

Figure 3.22: The average extinction law obtained for the region in Perseus with anomalously high χ^2 in the $R_V = 3.1$ map. The coordinates of this region are ($\sim 3^h40.5^m$ $+31°30'$). The dust models are the same as in Figures 3.18-3.20.

increase, not decrease, our values of A_λ/A_{K_s}.

3.6.3 Changes in the Near-Infrared Extinction Law

Throughout this chapter, we have assumed the extinction law in the near-IR wavelengths does not change from the WD5.5 model. This has advantages for comparison between our clouds and also comparing our results to other authors' who have made the same assumption. Furthermore, this assumption is backed by many observations as we discussed in § 3.6. If the near-infrared extinction law is fit as a power law, $A_\lambda \propto \lambda^{-\beta}$, than many authors have found values of β between 1.6 and 1.8 (Draine 2003, and references therein). Our WD5.5 model has $\beta \approx 1.6$. In this section, we would like to investigate how realistic our assumption for the near-IR extinction law is and what impact different extinction laws would have on our results.

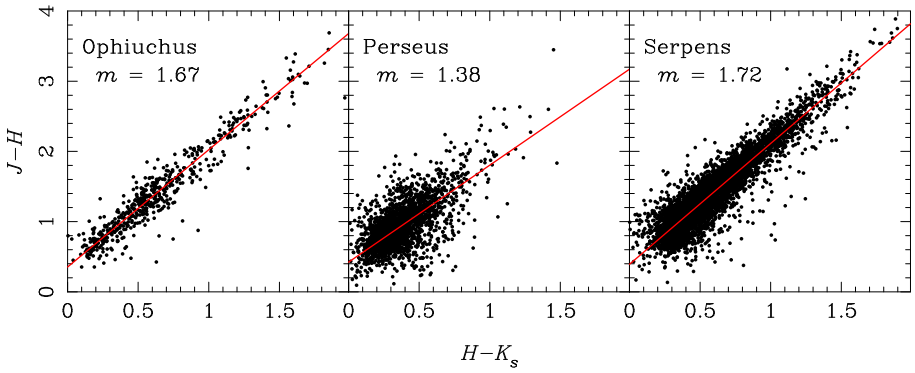

Figure 3.23: $J-H$ versus $H-K_s$ for all sources brighter than 15th magnitude at K_s. The best-fit line for each cloud is shown with the specified slope.

The JHK_s bands can be used to derive the extinction law in the near-infrared by plotting $J-H$ versus $H-K_s$ and fitting a straight line to the resultant distribution. If we assume the extinction law in the near-infrared can be expressed as a power law of the form $A_\lambda \propto \lambda^{-\beta}$, then the slope, m, is related to β:

$$m = \frac{(\lambda_H/\lambda_J)^\beta - 1}{1-(\lambda_H/\lambda_{K_s})^\beta} \tag{3.10}$$

where λ_J, λ_H, and λ_{K_s} are the isophotal wavelengths for the JHK_s bands. We have adopted 2MASS' isophotal wavelengths of 1.235, 1.662,and 2.159 μm for the JHK_s bands, respectively. In Figure 3.23 we have plotted $J-H$ versus $H-K_s$ for each cloud and the best-fit line through the data.

The best-fit lines for Ophiuchus and Serpens have slopes of 1.67 and 1.72, respectively, which correspond to $\beta = 1.38$ and 1.48. Our best-fit line in Perseus is not a good fit by eye to the reddening vector. The data appear to be consistent with a slope of approximately 1.7 as well. Slightly different slopes can change β by disproportionate amounts. For example, a slope of 1.68, 1.78, or 1.88 corresponds to β = 1.4, 1.6, or 1.8. Even though our data in all three clouds are most consistent with a slope of $\sim$ 1.7, slightly steeper slopes of 1.78 and 1.88 also provide a reasonable fit to the data. Therefore, we have plotted in Figure 3.24 the change in the extinction law due to assuming different

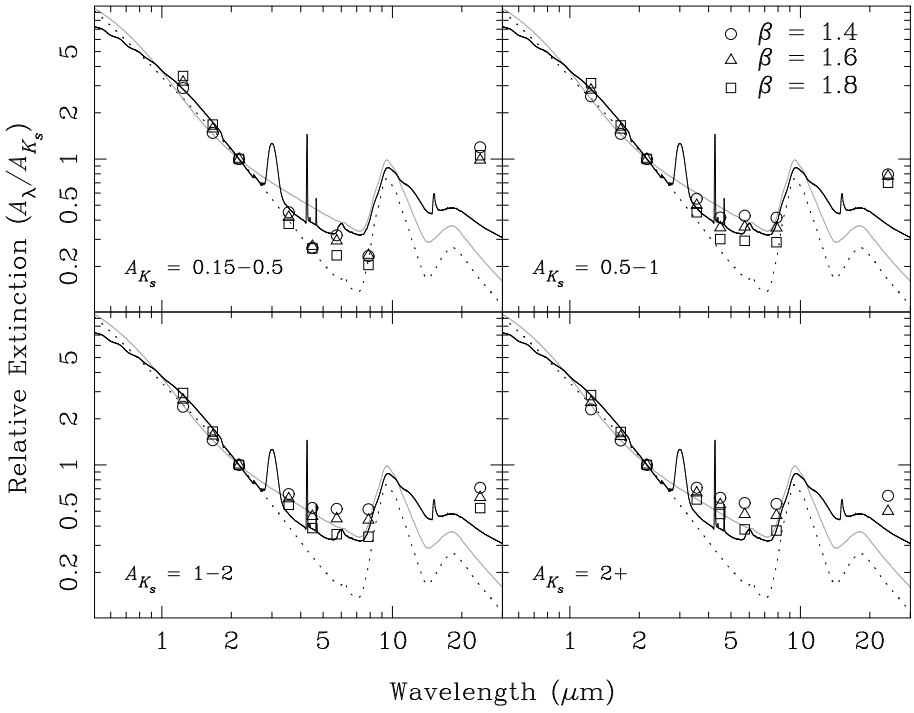

Figure 3.24: The extinction law in Serpens using three different extinction laws for the near-infrared JHK_s bands. These extinction laws are of the form $A_\lambda \propto \lambda^{-\beta}$.

values of β. This figure presents our data for Serpens with $\beta = 1.4$, 1.6, or 1.8.

Changes in β can noticeably alter our computed extinction law in the IRAC bands. In general, our extinction law is flatter for lower values of β. Between $\beta = 1.4$ and $\beta = 1.6$, the extinction law in the IRAC bands decreases by $10-15\%$ and between $\beta = 1.6$ and $\beta = 1.8$, the extinction law decreases a further $15-20\%$. The difference is larger at higher A_{K_s} values. Therefore, based on this analysis, we expect our assumption of the WD5.5 model ($\beta = 1.6$) introduces a systematic error of $10-15\%$ in our results. This level of error will shift the location of A_λ/A_{K_s} points up or down but will not affect our main conclusions. Note that the WD3.1 model also has $\beta = 1.6$.

3.7 Conclusions

We have observed regions up to 1 square degree in three molecular clouds: Ophiuchus, Perseus, and Serpens with both deep JHK_s and mid-infrared *Spitzer* data. All three clouds contain a range of column densities (extinction) and environments, with both star formation and unremarkable, non-star forming regions.

Based on the SED for each source, we identified the background stars in each cloud and created our catalogs of high-reliability stars. Our catalogs contain 2,365 stars in Ophiuchus, 11,280 in Perseus, and 49,485 stars in Serpens.

Each of these stars gave us a line-of-sight measurement of the extinction towards the source. We converted these measurements into uniform extinction maps with either $90''$ resolution in Ophiuchus and Perseus or $30''$ in Serpens. These maps trace the dust structure and can tell us about the physical properties of the clouds. Based on simulations of turbulent clouds, many authors have shown that the histogram of density, the probability density function, is expected to be lognormal. Ostriker et al. (2001) showed the same is true for the column density, a more readily observable parameter. We plotted the histogram of extinction for each of our clouds in Figure 3.12. All three clouds are log-normal, though each also contains a "tail" at low extinction which is likely due to the inclusion of off-cloud regions in our maps.

We also compared the size-scale of the dust structure by computing $\sigma_{A_{K_s}} - A_{K_s}$, the standard deviation of A_{K_s} measurements in a cell versus the average A_{K_s} of that cell. Serpens, at $l = 30$, $b = 5$ appears to contain sub-structure below $30''$ resolution while Ophiuchus and Perseus, at higher Galactic latitudes, appear to resolve all sub-structure at $30''$ resolution for $A_{K_s} \leq 2$. Above $A_{K_s} = 2$, the small number of cells prevents us from drawing definitive conclusions about the possible existence of sub-structure.

In addition to the quantity of dust along a given line-of-sight, we mapped the changes

in the dust properties in comparison to two dust models, the Weingartner & Draine (2001) $R_V = 3.1$ and $R_V = 5.5$ models. We computed a χ^2 statistic for each star based on its difference from either dust model and then created a uniform map similar to how we created A_{K_s} maps. We found that the χ^2 value based on $R_V = 3.1$ is strongly correlated with A_{K_s} while the $R_V = 5.5$ χ^2 shows little or only slight increase based on A_{K_s}. We did find one region in Perseus which appears to violate this general rule: despite a modest extinction, $A_{K_s} = 0.62$, the $R_V = 3.1$ χ^2 peaks at 39.

In addition to creating χ^2 maps which show the spatial dependence of the dust properties, we also computed the wavelength dependence of the extinction, known as the extinction law. We plotted the extinction law in several ranges of A_{K_s}. For low extinction, our results in the IRAC bands ($3.6 - 8\,\mu$m) are consistent with the WD3.1 dust model. This is not so surprising since WD3.1 was designed to match observations in the diffuse interstellar medium (e.g. Rieke & Lebofsky 1985). The systematic errors in determining the flux cause the errorbars to be very large for $A_{Ks} < 0.5$, making it impossible to statistically distinguish between WD3.1 and WD5.5.

At higher extinctions, the extinction law tends to flatten in all three clouds and is consistent with the WD5.5 dust model. This indicates grain growth in the denser regions of clouds because the WD5.5 model incorporates larger grains than WD3.1. This flatter extinction law is more consistent with many recent results (Flaherty et al. 2007; Indebetouw et al. 2005; Lutz 1999). Serpens and Perseus are slightly above the WD5.5 model which may indicate water ice due to the $A_{5.8}/A_{K_s}$ data point. There appears to be no correlation between star formation and the extinction law. Ophiuchus, centered on the star forming region of L1688, has an extinction law well fit by the WD5.5 dust model, while Serpens with "Cluster B" has an extinction law flatter than WD5.5. The star-forming region in Perseus identified as IRAS 03382+3145 does not appear significant in the χ^2 map of the region (fig. 3.15)

The anomalous region in our $R_V = 3.1$ χ^2 Perseus map has an extinction law much flatter than in any other cloud. The most prominent data point is again at 5.8 μm. One possible explanation is that water ice in this region is causing the extinction law to vary, even though the average column density in this region is modest.

At 24 μm, our computed extinction law is significantly higher than current dust models predict. With slight changes to our assumed average stellar model, we were able to lower our values, but they are still not in line with WD3.1, WD5.5, or KP v5.0. Our values *are* consistent with the values found by Flaherty et al. (2007). There appears to be a negative correlation between A_{K_s} and the value of A_{24}/A_{K_s}. This is the opposite trend we would expect since grain growth in dense regions should increase A_{24}/A_{K_s}, not lower it.

Chapter 4

Deep JHK_S and *Spitzer* Imaging of Four Cores

4.1 Introduction

Unlike clusters such as Orion or NGC 1333, dark cores are believed to be cases of individual star formation in isolation. This theory has not been well-tested since the primary infrared survey in cores has been, until recently, IRAS. The low resolution and low sensitivity of IRAS means that it is impossible to address whether IRAS protostars may actually be resolvable into several components, or whether faint low-mass companions exist to the primary source in a core. The presence or lack of embedded protostar(s) within an isolated core may also affect the dust properties due to processing of the ISM through radiation or molecular outflows.

In this chapter we have observed four isolated cores using both *Spitzer* and ground-based JHK_S imaging. Based on IRAS, two of these cores are known to harbor protostars while two are believed to be starless. As was the case in L1014 (Young et al. 2004), we hope to uncover previously unknown protostars in our core sample. Furthermore,

with the *Spitzer* and JHK_s data, we will be able to map changes in the dust properties throughout each core and compare the dust properties of cores with protostars to those without. We will use three different dust models in this chapter. The Weingartner & Draine (2001) $R_V = 3.1$ and $R_V = 5.5$ models were chosen because they incorporate polycyclic aromatic hydrocarbons (PAHs) and grain growth in the $R_V = 5.5$ model. The third model is being developed by Pontoppidian et al. (in prep) starting from a simplified version of the Weingartner & Draine $R_V = 3.1$ model and incorporating icy mantles on the dust grains. We have used version 5.0 of this model. Throughout this chapter we will denote these models as WD3.1, WD5.5, or KP v5.0, respectively.

4.2 Observations

We mapped four cores in the near-infrared and *Spitzer* wavelengths: L204C-2, L1152, L1155C-2, and L1228. These cores were selected based on being nearer than 400 parsecs (for the best spatial resolution and detecting faint objects), located at a galactic latitude $b = 10 - 20^\circ$ (so as to minimize stellar confusion), and observable from Kitt Peak so we could obtain deep JHK_s observations. Furthermore, two of our cores, L1152 and L1228, are classified as "starred" while L204C-2 and L1155C-2 are "starless". This classification was made based on the presence or lack of an embedded IRAS source as determined by Lee et al. (1999).

For our JHK_s data, we used the FLoridA Multi-object Imaging Near-ir Grism Observational Spectrometer (FLAMINGOS) (Elston 1998) instrument installed on the 4-meter telescope at Kitt Peak. Our observations spanned four epochs from October 2003 to June 2006. We mapped each core with 5-7 $10' \times 10'$ fields. With the exception of a small corner in L204C-2, these data completely cover the areas mapped with *Spitzer*, including regions only mapped in 1 or 2 *Spitzer* bands. Each core was mapped to ensure 10σ limits

$\sim$ 3.5 magnitudes deeper than 2MASS in all three of the JHK_s bands. Furthermore, we mapped the central regions of L1152, L1155C-2, and L1228 to an even deeper limit, or approximately $4-4.5$ magnitudes deeper in JHK_s . We did not map the central region of L204C-2 to this deeper limit due to time constraints.

We modeled our *Spitzer* observations after the c2d ones. We chose to integrate $10\times$ longer than c2d in the IRAC1-4 and MIPS1 wavebands (3.6, 4.5, 5.8, 8.0, and 24 μm). We observed each core in two epochs, where the second epoch was separated from the first by as little as one day but could be up to almost a month later. Only one core, L204C-2, is located at an ecliptic latitude where asteroids may be a problem. The separation of the two observing epochs ensures we can identify these sources. IRAC and MIPS1 were observed separately, resulting in four *Spitzer* Astronomical Observation Requests (AORs) per core. Unlike c2d, we did not take short integrations in the IRAC bands to compensate for saturated objects. Our *Spitzer* observations are summarized in Table 4.1. Basic properties of the cores are presented in Table 4.2.

4.3 Data Reduction

We have produced final source catalogs of our cores using separate pipelines for the JHK_s and *Spitzer* observations. Full descriptions of the pipelines used for reducing our data can be found in Chapter 2 and in the c2d delivery documentation (Evans et al. 2007). We will discuss briefly our data and how our processing procedure differs from the standard pipelines.

Table 4.1. Summary of *Spitzer* Observations

Region	AOR Number	Date Observed YYYY-MM-DD	Program ID
L204C-2	11393792	2005-04-07	3656
	11396352	2005-04-08	3656
	11392000	2005-08-22	3656
	11398912	2005-08-23	3656
L1152	11390976	2004-07-23	3656
	11399424	2004-07-28	3656
	11394304	2004-10-15	3656
	11396864	2004-11-10	3656
L1155C-2	11392768	2004-07-22	3656
	11399936	2004-08-12	3656
	11394816	2004-12-02	3656
	11397376	2004-12-26	3656
L1228	11391232	2004-11-28	3656
	11395072	2004-12-07	3656
	11400192	2004-12-16	3656
	11397632	2004-12-26	3656

Table 4.2. Basic Properties of the Cores

Core	*l* (deg.)	*b* (deg.)	Dist. (pc)
L204C-2	6	20	165[a]
L1152	102	16	325[a]
L1155C-2	102	15	325[a]
L1228	111	20	300[b]

[a]Lee et al. (1999)

[b]Jijina et al. (1999)

4.3.1 Image Mosaics

The mosaics for the *Spitzer* bands were made using MOPEX as part of the c2d pipeline (Makovoz & Marleau 2005). For the JHK_s bands, we used the `mscimage` and `imcombine` tasks in IRAF. We plotted the mosaics for the $J-24\,\mu$m bands in Figures 4.1 - 4.4. Furthermore, we combined the IRAC1 ($3.6\,\mu$m), IRAC4 ($8\,\mu$m) and MIPS1 ($24\,\mu$m) images into a three-color image for each core. These color images are displayed in Figures 4.5-4.8. On each color image we have also plotted extinction contours in white to make the location of the core evident. These contours start at $A_{K_s} = 0.5$ in steps of 0.15 ($3\,\sigma$). The extinction maps will be discussed in more detail in § 4.5.

4.3.2 Saturated Sources in IRAC

Our *Spitzer* observations were processed using the c2d pipeline. Our data differ from c2d's observations of these cores in that we did not take any short "high dynamic range" (HDR) observations to obtain the fluxes for bright sources saturated in the IRAC bands. Instead, we used the c2d observations, which *do* contain HDR frames to correct for saturated fluxes. We compared our fluxes with the c2d fluxes in each IRAC band and empirically determined a flux limit at which our values diverged from c2d's. We then substituted the c2d fluxes for any sources with a c2d flux brighter than this limit. The flux limits we used are 35, 35, 300, and 150 mJy for the 3.6, 4.5, 5.8, and $8.0\,\mu$m bands, respectively.

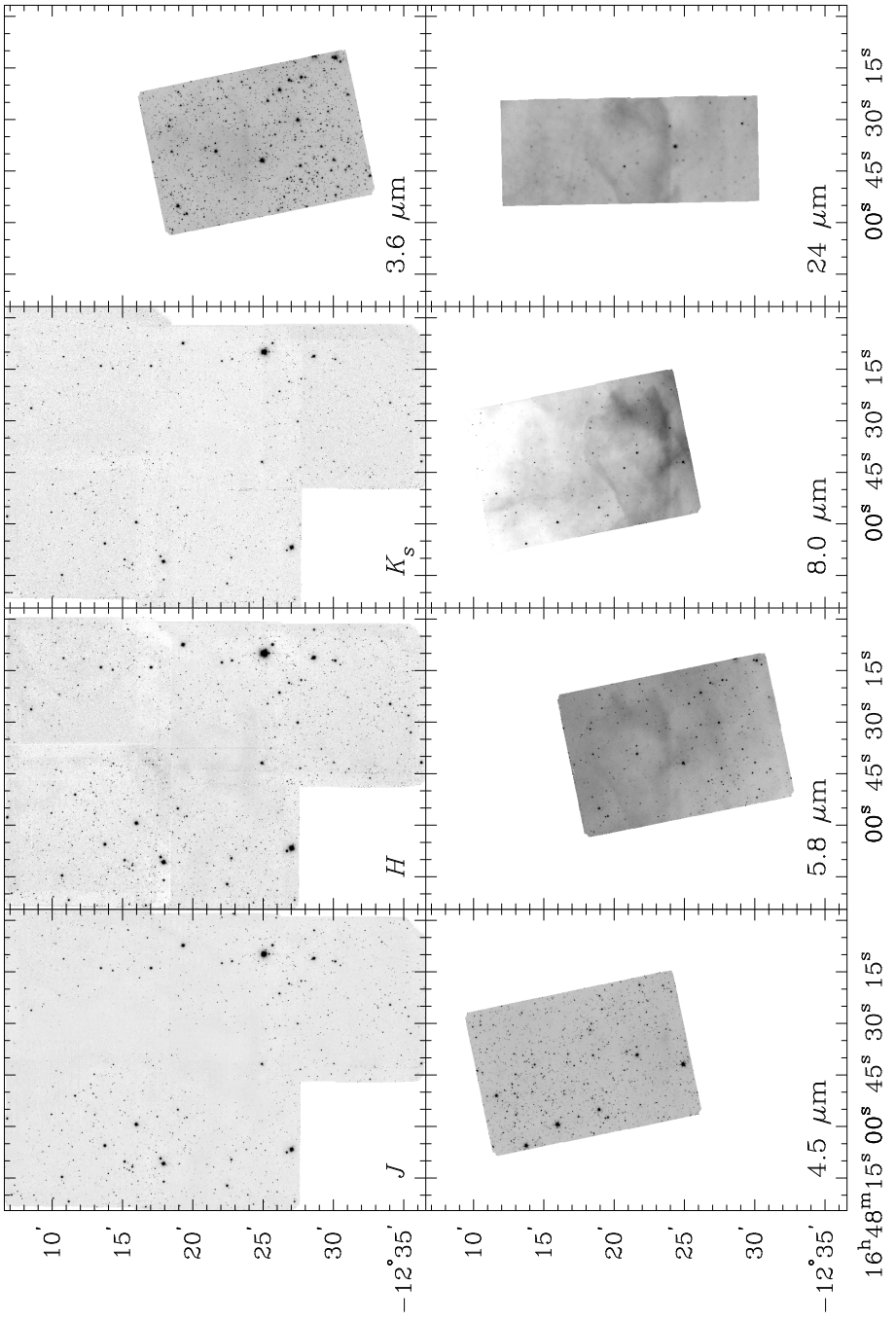

Figure 4.1: Image mosaics for the J - 24 μm bands in L204C-2.

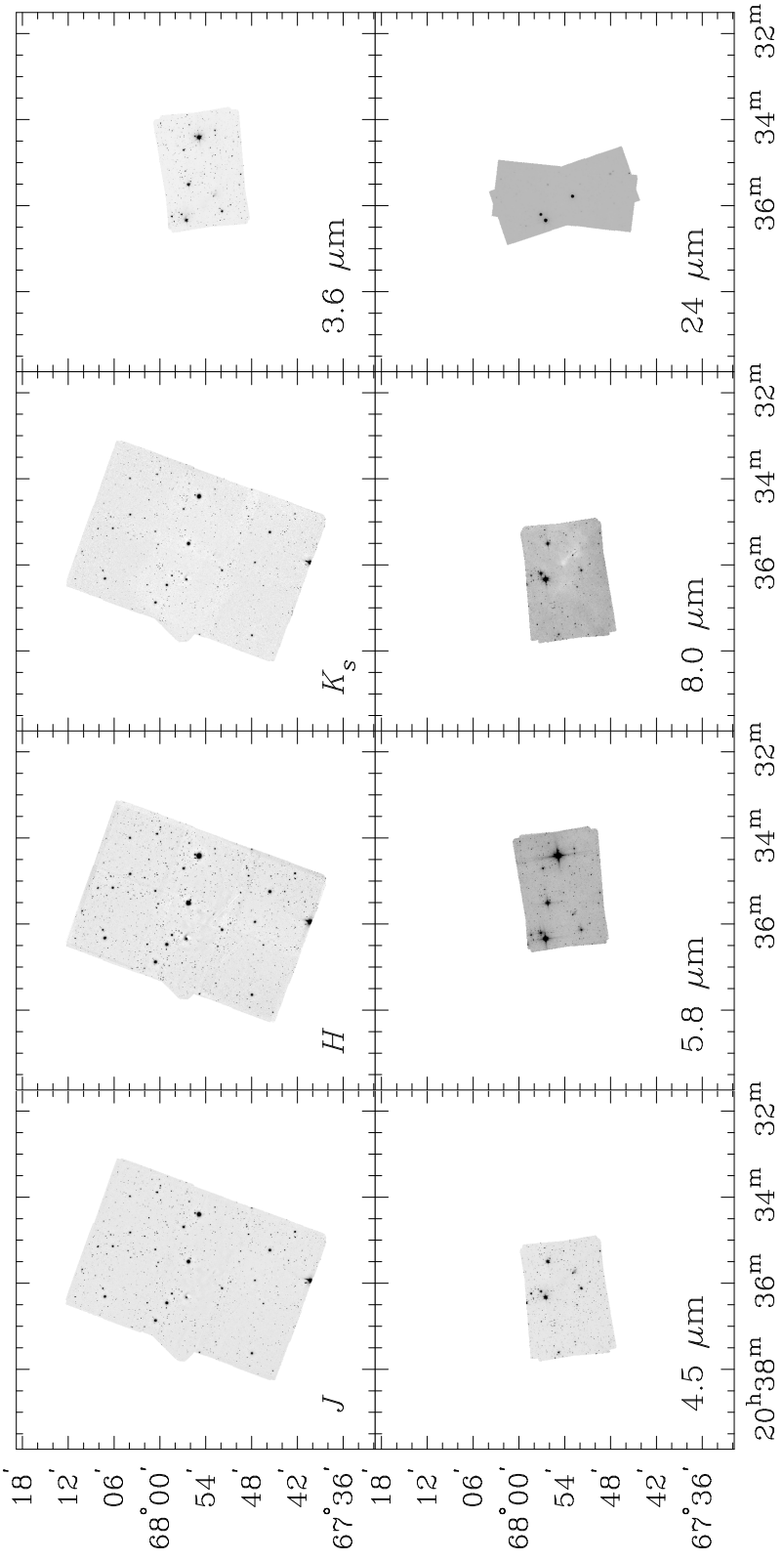

Figure 4.2: Image mosaics for the J - 24 μm bands in L1152.

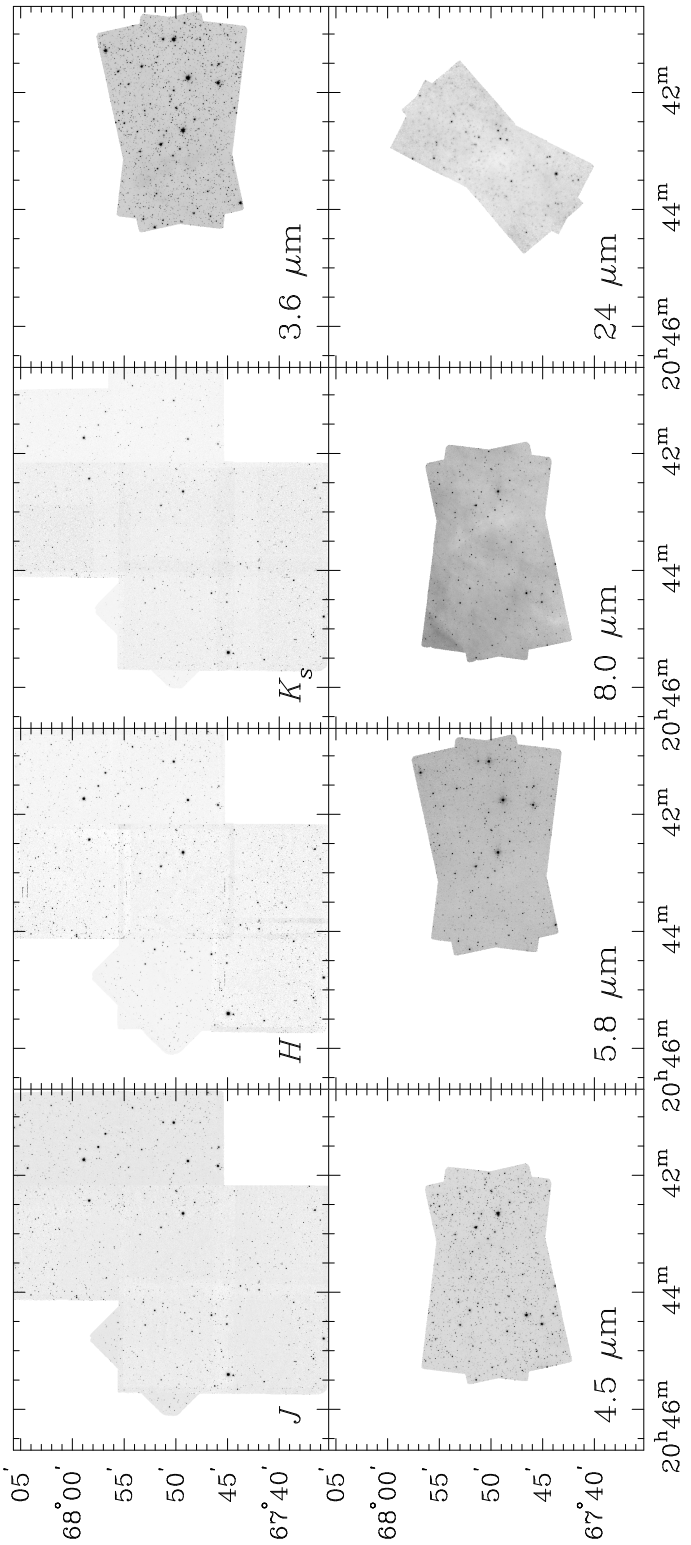

Figure 4.3: Image mosaics for the J - 24 μm bands in L1155C-2.

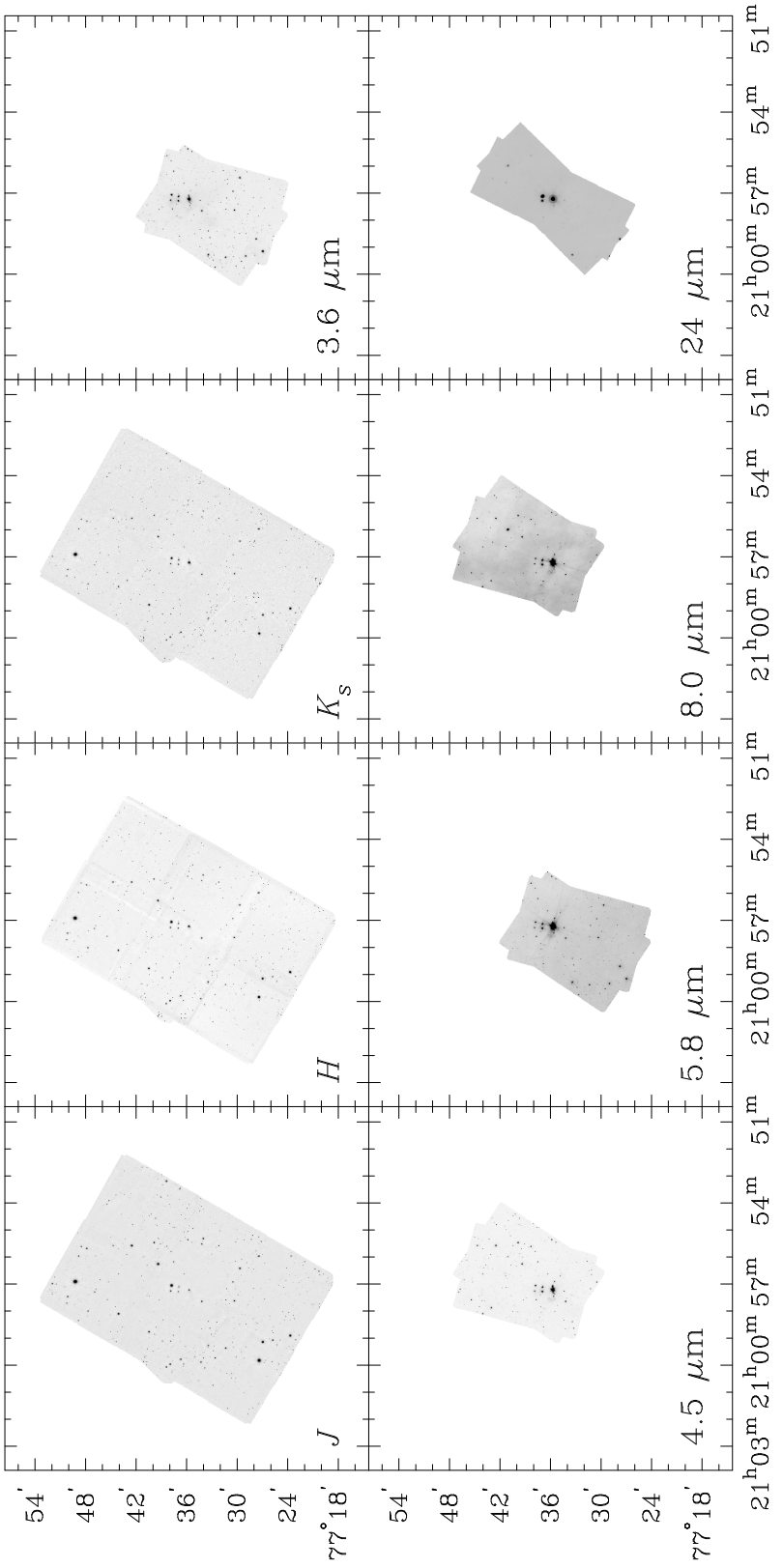

Figure 4.4: Image mosaics for the J - 24 μm bands in L1228.

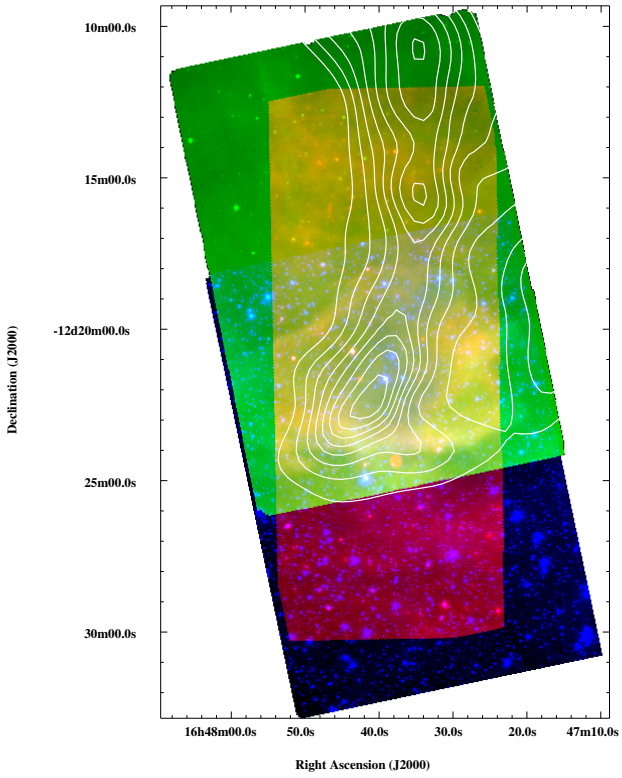

Figure 4.5: Color image of the core L204C-2 made from the 3.6 μm (blue), 8.0 μm (green), and 24 μm (red) channels on board *Spitzer*. We have plotted extinction contours to show the location of the core. Contours start at $A_{K_s} = 0.5$ in steps of 0.15 (3σ).

4.3.3 High Reliability Star Catalogs

We used the c2d pipeline to classify our sources, as discussed in § 2.5. For our discussion on the dust extinction and the extinction law, high reliability near-infrared JHK_s data are essential because these wavelengths alone are used to calculate extinctions and extrapolate the extinction law in the *Spitzer* bands. With 'Young Stellar Object candidates' (YSOcs), 'Galaxy candidates' (Galc), and other infrared excess sources we cannot separate out the expected flux of the SED from changes in those fluxes due to variations in the extinction law. JHK_s-only sources cannot be used in computing changes in the extinction law at mid-infrared wavelengths but are useful in obtaining line-of-sight extinctions.

Some heavily extincted stars may only fit the WD5.5 dust model rather than the tradi-

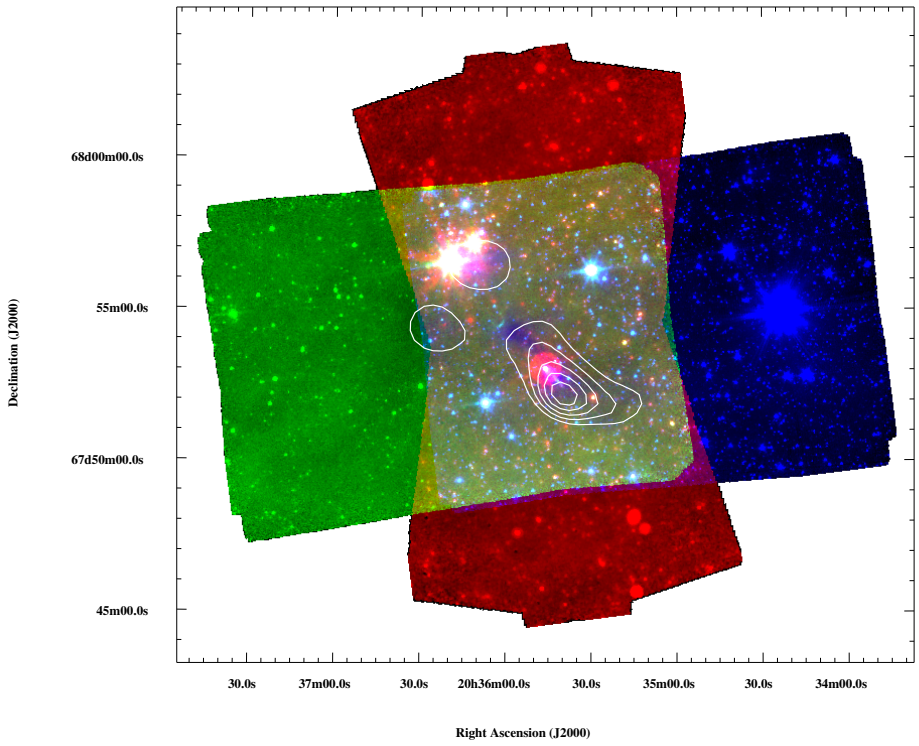

Figure 4.6: Color image of the core L1152 made from the 3.6 μm (blue), 8.0 μm (green), and 24 μm (red) channels on board *Spitzer*. We have plotted extinction contours to show the location of the core. Contours start at $A_{K_s} = 0.5$ in steps of 0.15 (3σ).

tional WD3.1 extinction law. We saw this in the clouds, § 3.3. Therefore, to create high-reliability star catalogs we only used those sources classified as stars with the WD5.5 dust model. In this step we also excluded any sources only classified as stars when one of the wavebands was dropped. We did not want to bias our results on the extinction law due to a prominent absorption or emission line. Furthermore, because accurate extinctions are essential to this dissertation, we required sources to have detections $\geq 5\sigma$ in each of the JHK_s bands. Lastly, we 'cleaned' our star catalogs to remove suspected faint background galaxies. This procedure will be discussed in detail in § 4.4.1. In Table 4.3 we list the number of sources in our star catalog for each core both before and after removal of faint background galaxies. In this chapter whenever we refer to the star catalogs, we will be

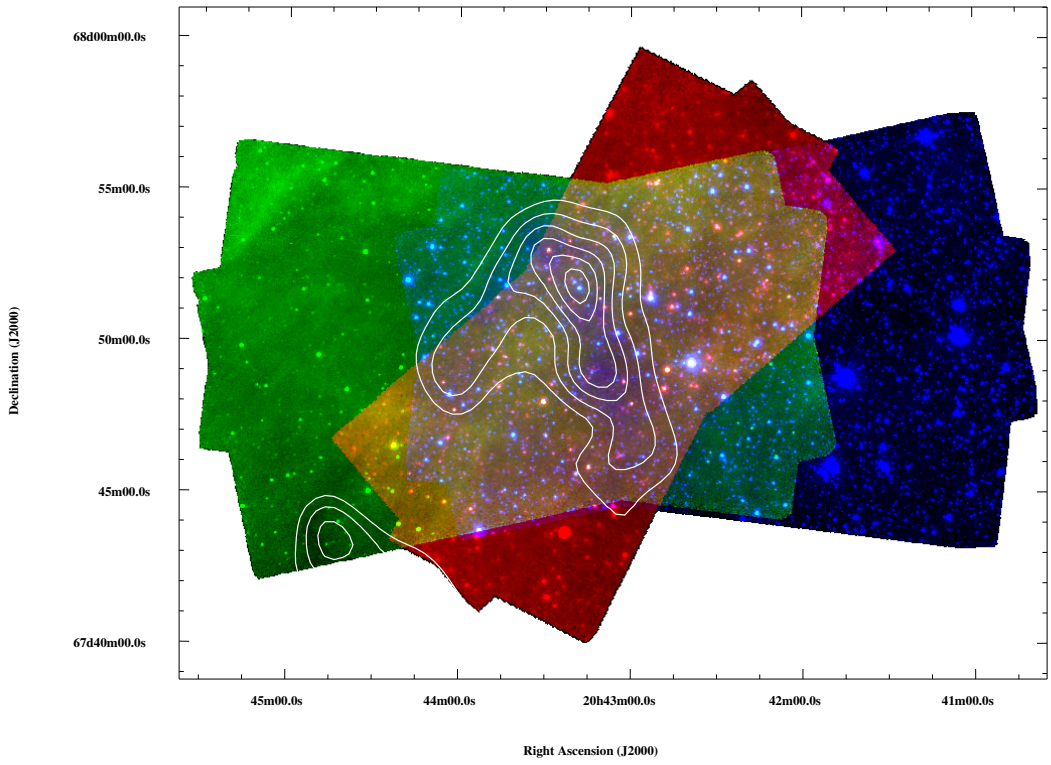

Figure 4.7: Color image of the core L1155C-2 made from the 3.6 μm (blue), 8.0 μm (green), and 24 μm (red) channels on board *Spitzer*. We have plotted extinction contours to show the location of the core. Contours start at $A_{K_s} = 0.5$ in steps of 0.15 (3σ).

using the cleaned star catalogs.

4.3.4 Detection Limits

Our 10σ limits are: 19.5, 18.8, 17.7, 18.6, 17.9, 15.5, 14.7, and 10.4 magnitudes for the J, H, K_s, IRAC1, IRAC2, IRAC3, IRAC4, and MIPS1 bands, respectively. Our JHK_s limits are ~ 3.5 magnitudes deeper than 2MASS' 10σ limits of 15.8, 15.1, and 14.3 magnitudes in the JHK_s bands. We also took deeper JHK_s observations in the region near the dense core for L1152, L1155C-2, and L1228. The 10σ limits for JHK_s in these regions are 19.9, 19.7, and 18.6 magnitudes, or $4-4.5$ magnitudes deeper than 2MASS in all three bands.

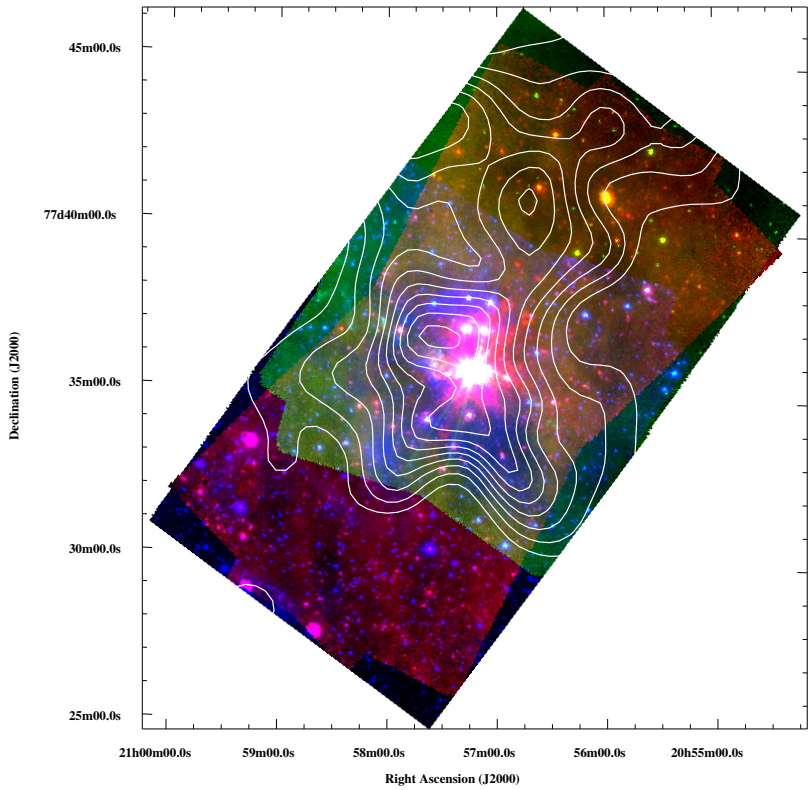

Figure 4.8: Color image of the core L1228 made from the 3.6 μm (blue), 8.0 μm (green), and 24 μm (red) channels on board *Spitzer*. We have plotted extinction contours to show the location of the core. Contours start at $A_{K_s} = 0.5$ in steps of 0.15 (3σ).

4.4 Source Statistics

Table 4.3 lists the number of sources detected in each core. This number is further broken down by: sources detected in 3 or more bands, JHK_s-only detections, sources in our high reliability star catalog, and sources in our high reliability catalog after the removal of faint suspected background galaxies (called "cleaning"). This procedure will be described below. Compared to 2MASS, our JHK_s data match up with 5$\times$ as many *Spitzer* sources.

Table 4.3. Number of Sources in the Cores

Core	Total	3+ bands	JHK_s-only	High Reliability[a]	
				Stars	Cleaned
L204C-2	18,511	4950	2202	3244	3219
L1152	17,878	6142	3126	4038	4010
L1155C-2	23,542	6734	2498	3926	3891
L1228	16,395	3682	1414	1850	1810

[a] Sources meeting our high-reliability criteria, § 4.3.3

Note. — The number of sources in each core meeting different selection criteria. The 'stars' and 'cleaned' columns are discussed in § 2.5 and § 4.4.1.

4.4.1 Bright 24 μm Sources

There are a number of bright 24 μm sources that appear red in the color mosaics. These sources are very unlikely to be stars since stars will not be brighter at 24 μm compared to shorter wavelengths due to the Rayleigh-Jeans tail on the blackbody curve. Therefore, these sources are either asteroids, background galaxies, or embedded YSOs. Asteroids are only potentially a problem in L204C-2, which is located at ecliptic latitude $\beta \approx 10^\circ$. The other three cores are located at $\beta \sim 75^\circ$ ecliptic latitude. By comparing our two individual epochs of observation, we were able to identify several prominent asteroids by eye in our L204C-2 data.

Even after the removal of asteroids from L204C-2, there remains a number of non-asteroid bright 24 μm sources in the mosaic for this core, as well as in the mosaics for the other three cores. Since these sources are not asteroids, they are either background galaxies or embedded YSOs.

To help separate the background galaxies from the YSOs, we have used the SWIRE

observations of ELAIS N1 (Surace et al. 2004). The ELAIS N1 region is towards the North Galactic pole. Because of the low extinction towards this region and its galactic location, these data are expected to contain nothing except stars and background galaxies, making them very useful for comparison. The c2d team processed these SWIRE data through their pipeline to create a c2d-processed SWIRE catalog. We will be using this catalog.

Figure 4.9 shows K_s vs. $K_s - [24]$ for each core. In this figure, we have only plotted sources with JHK_s detections $\geq 5\sigma$ and with MIPS1 detections $\geq 3\sigma$. We chose to plot these two bands because the remaining red sources appear bright at $24\,\mu$m and because our K_s observations cover the entire $24\,\mu$m region observed. We have used four symbols based on how each source is classified (see § 2.5): stars are shown as circles, Galc sources are squares, YSOc objects are triangles, and plus signs represent all other classifications. The vertical dotted lines separate different YSO classes defined by $\alpha = \frac{\mathrm{d}\log\lambda F_\lambda}{\mathrm{d}\log\lambda}$, the slope of the linear least-squares fit to all data points in the SED from $K_s - 24\,\mu$m. The four classes are as follows: Class I: $\alpha \geq 0.3$; Flat spectrum: $0.3 > \alpha \geq -0.3$; Class II: $-0.3 > \alpha \geq -1.6$; and Class III: $\alpha < -1.6$ (Greene et al. 1994). We have included sources with $\alpha = 0.3$ into class I since these sources were left undefined by Greene et al. (1994). Class I objects should be the youngest and most embedded protostars while Class III sources are the oldest protostars and very close to entering the main-sequence. The shaded contours are the c2d-processed SWIRE data.

We identify three regions in our color-magnitude diagram: stars are located at $K_s - [24] \approx 0$, background galaxies have an excess $K_s - [24]$ color but are fainter than 15th magnitude at K_s, and YSOs also have a positive $K_s - [24]$ color but are brighter than 15th magnitude at K_s. Note that our sources from the cores do not completely match with the shaded contours that come from the c2d processed SWIRE catalog. The reasons for this are that our K_s data are deeper than 2MASS and our $24\,\mu$m observations are $\sim 3\times$ deeper

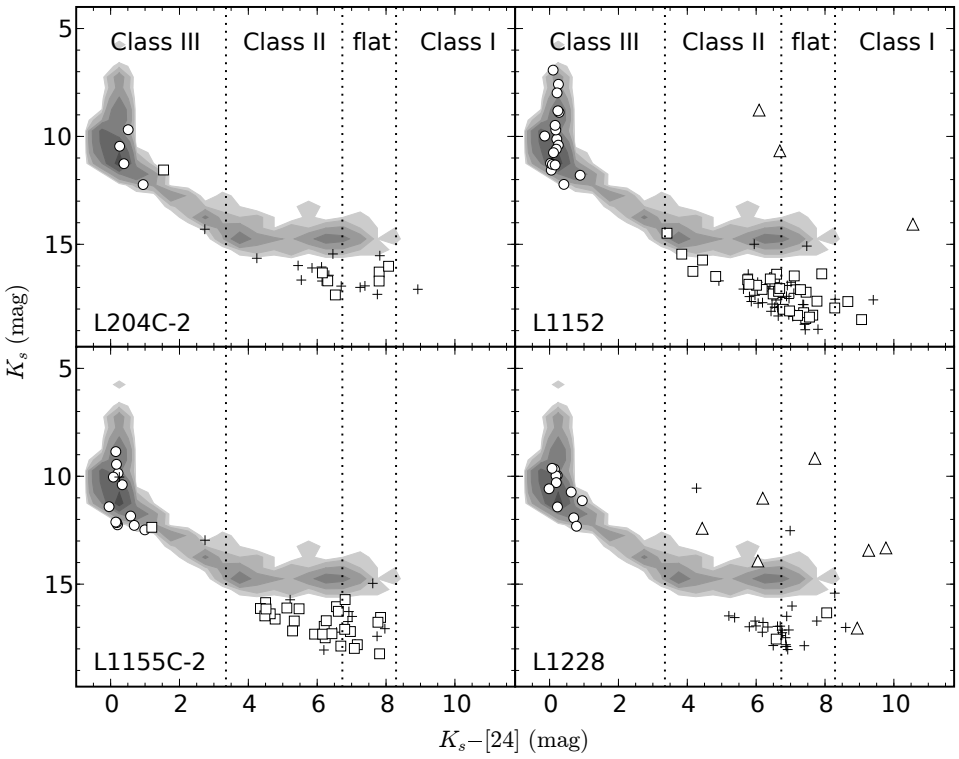

Figure 4.9: K_s vs. $K_s - [24]$ plot for our cores. We have used four different symbols to correspond to different source classifications: stars are circles, Galc sources are squares, YSOc objects are triangles, and plus signs denote all other classifications. The vertical lines denote separations between different YSO classes as defined by Greene et al. (1994). The shaded contours are of part of the SWIRE ELAIS N1 region. See the text for more description on these data.

than c2d. With our deeper data, we can match many more faint K_s and 24 μm detections to each other than possible with c2d. From Figure 4.9 we can see that almost all of the 24 μm excess sources in Figures 4.5 - 4.8 are likely to be background galaxies even if they are not classified as Galc. In the two starless cores, L204C-2 and L1155C-2, there are no objects classified as YSOc, nor any likely YSOs based on K_s vs. $K_s - [24]$ color. There are only a handful of YSOc and potential YSOs in the other two cores. The YSOs in our cores will be discussed in § 4.4.3.

4.4.2 Faint Galaxies

In Figure 4.9 we identified a number of background galaxies in our cores. However, this figure only shows those galaxies bright enough to be detected at 24 μm. There may be fainter galaxies that are detected at shorter wavelengths, but are mis-identified as stars. To explore this possibility, we followed the method from § 3.4.2. We selected two populations of 'known' sources from Figure 4.9: 'stars' ($K_s - [24] \leq 1$) and 'galaxies' ($K_s - [24] \geq 4$ and $K_s \geq 15$). Figures 4.10 and 4.11 show the location of these 'stars' and 'galaxies' in three color-color diagrams. Figure 4.10 plots $J-H$ versus $H-K_s$ while Figure 4.11 shows $H-K_s$ versus $K_s - [3.6]$ and versus $K_s - [4.5]$. The dashed lines are the same ones empirically derived in § 3.4.2. Based on these two figures, we believe that there are a number of faint background galaxies present in our star catalogs. These sources appear in $J-H$ versus $H-K_s$ with a large $H-K_s$ color but only a modest $J-H$ color that is inconsistent with stars following a standard reddening law (e.g. Lombardi & Alves 2001). From Figure 4.10 we see that many of the 'known' galaxies have these peculiar colors. In Figure 4.11 we plotted only those sources selected by the dashed lines in Figure 4.10 with the 'known' populations of stars and galaxies overlaid.

We have created cleaned star catalogs to remove these suspected background galaxies. The two criteria we have used are the same as the ones from § 3.4.2, with one important difference: because there is such a large degree of non-overlap between the four IRAC bands, we have relaxed the second criterion so that sources only need to satisfy either the first half or the second half of the criterion. Our criteria are:

1. $J-H \geq 0.6$, $H-K_s \geq 0.6$, and $J-H \leq 1.9(H-K_s) - 0.16$

2. $H-K_s \leq 1.32(K_s - [3.6])$ or $H-K_s \leq 1.32(K_s - [4.5])$

Sources meeting both of these criteria were removed from our final star catalogs. In Table 4.3 we list the numbers of sources in our star catalogs originally and after removing

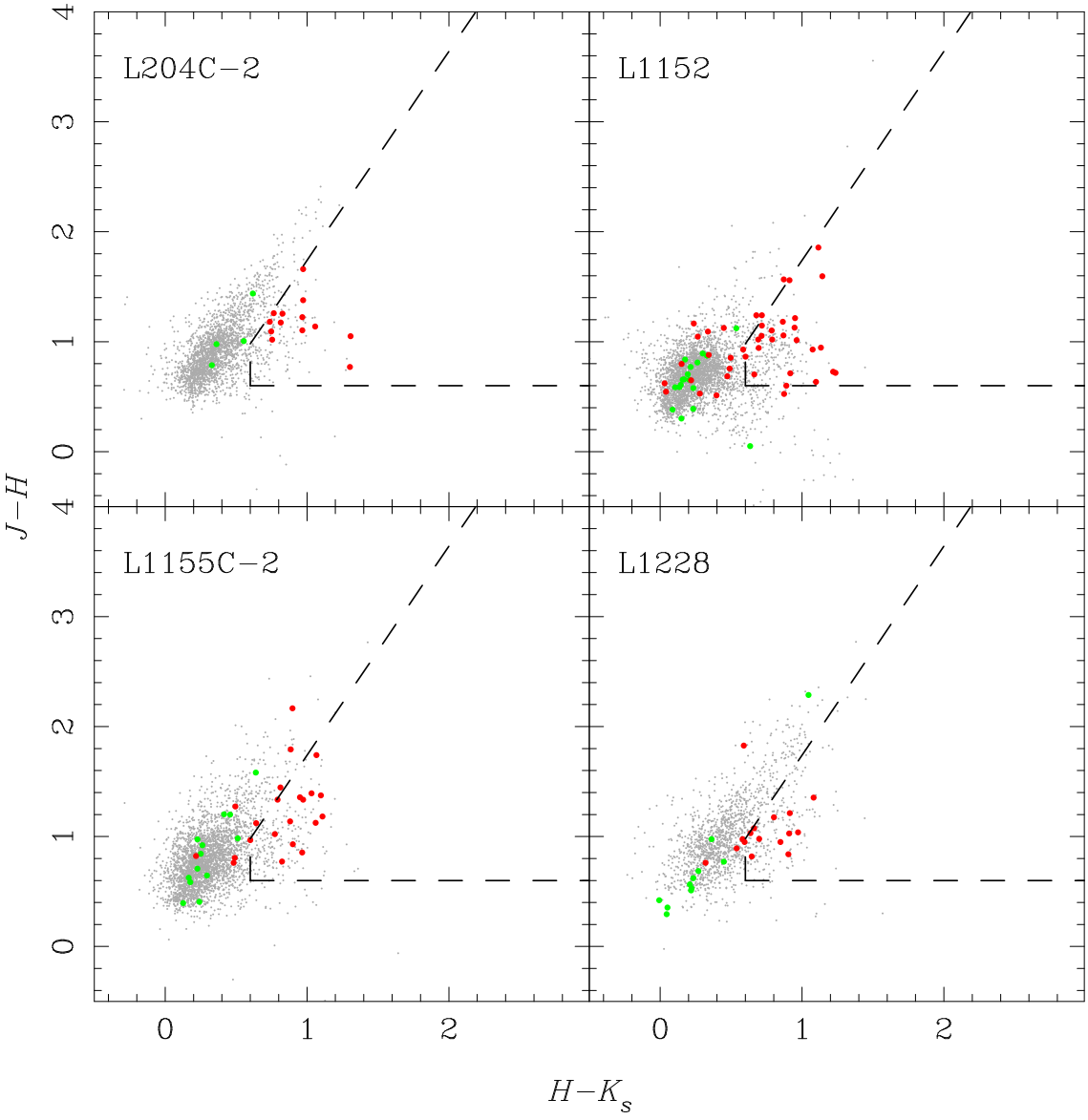

Figure 4.10: $J-H$ vs. $H-K_s$ color-color diagram for our cores. Those points classified as stars (§ 2.5) with uncertainties in JHK_s magnitudes ≤ 0.1 are shown in gray. The green points are 'known' stars and the red ones are background galaxies. See the text for a discussion on how these sources were selected. The dashed lines select those sources with $J-H \geq 0.6$, $H-K_s \geq 0.6$, and $J-H \leq 1.9 \times (H-K_s) - 0.16$.

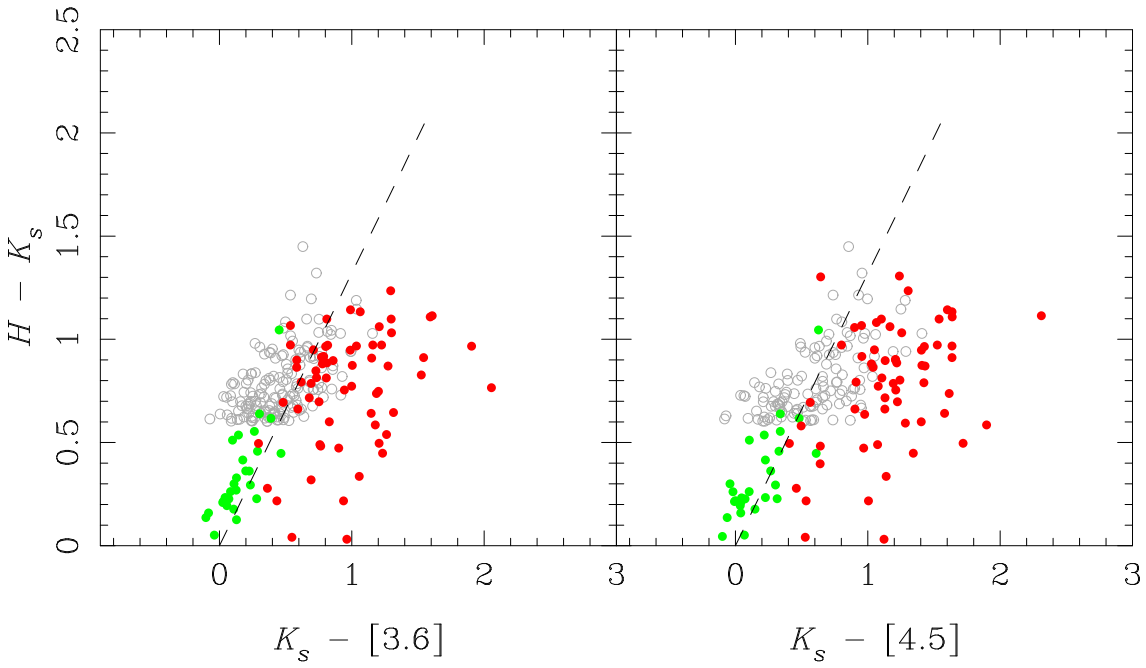

Figure 4.11: $H - K_s$ vs. $K_s - [3.6]$ (left) and vs. $K_s - [4.5]$ (right). The gray points are the sources selected from Figure 4.10. The green points are stars while the red points are background galaxies. See the text for discussion of how these sources were selected. The dashed line in each panel has the equation $H - K_s = 1.32x$ where x is either $K_s - [3.6]$ or $K_s - [4.5]$.

faint background galaxies. The percentage of sources removed is less than 1% for L204C-2, L1152, and L1155C-2, and 2.2% in L1228.

4.4.3 Young Stellar Objects

In Table 4.4 we list the positions and fluxes of the 10 YSOs in our cores. To create this list, we first selected all objects classified as YSOc in each core (10 sources). We also added all sources from Figure 4.9 with $K_s - [24] \geq 3$ and $K_s \leq 14.5$. This amounts to two sources in L1228, neither of which is classified as YSOc because they are outside of the area observed in IRAC2 and IRAC4 (4.5 and 8 μm). Finally, we plotted all the Galc objects in Figures 4.13-4.16 and selected those located in the dense core region. We selected one source each in L204C-2 and L1152 and two in L1228.

After these three selection criteria, we had a total of 16 objects. After visual in-

spection, we excluded the Galc objects in L1152 and L1228 since all appeared visually extended in mosaics. We also excluded the one Galc object from L204C-2 which has an SED of a heavily extincted star rather than a Galc. In Figure 4.9, this source is the Galc at $K_s - [24] = 1.5$. Furthermore, we excluded one of the YSOc objects in L1228 which is clearly a knot of emission from the outflow and not a real source ($K_s - [24] = 9$). Lastly, we also excluded one of the non-YSOc sources in L1228 which only has an infrared excess at $24\,\mu$m ($K_s - [24] = 4.3$). After visual inspection, this source appears confused with two other nearby sources at $24\,\mu$m.

In our final table there are three sources in L1152 and seven in L1228. Neither L204C-2 nor L1155C-2 appear to contain any YSOs, further confirming the starless nature of these cores. In Figure 4.12 we have plotted the SED for each YSO listed in Table 4.4.

We estimated the luminosity for each YSO using DIRT, the Dust InfraRed Toolbox (Pound et al. 2004, 2000). DIRT has a grid of hundreds of thousands of models for stars in envelopes with many tunable parameters such as source luminosity, effective temperature, grain type, and various parameters controlling the envelope. We searched the grid to obtain models fitting the following parameters: $A_V = 1 - 100$, any outer envelope radius, $L = 0.001 - 100\,L_\odot$, OH5 (Ossenkopf & Henning 1994) dust grains, and an envelope density profile of r^{-2}. These parameters returned around 15,000 models for us to choose from. Each model contained observed fluxes, scaled to the distance of our cores, for near- and mid-infrared wavelengths. The near-infrared wavelengths were *not* convolved to the JHK_s bands, however the mid-infrared values are convolved for the *Spitzer* IRAC and MIPS filters.

For each YSO, we computed χ^2, the difference between the model and the observed flux over the wavebands J - MIPS1. We then binned the $\sim 15,000$ models by luminosity and computed the mean χ^2 in each luminosity bin. The luminosity bin with the minimum χ^2 was chosen as our best estimate for the luminosity of the source. With this method, we

Table 4.4. Young Stellar Objects in the Cores

Region	RA (J2000)	DEC (J2000)	Lum. ($L_\odot$)	J (mJy)	H (mJy)	K_s (mJy)	3.6 μm (mJy)	4.5 μm (mJy)	5.8 μm (mJy)	8.0 μm (mJy)	24 μm (mJy)	70 μm (mJy)
L1152	308.9428774	67.8839438	0.01	0.130 ± 0.007	0.696 ± 0.034	1.57 ± 0.05	3.59 ± 0.19	6.44 ± 0.32	5.50 ± 0.26	3.36 ± 0.16	280 ± 26	3670 ± 341
L1152	309.0485380	67.9525803	0.3	9.19 ± 0.19	25.5 ± 0.6	36.1 ± 0.7	41.3 ± 2.0	47.9 ± 2.3	60.8 ± 2.9	77.8 ± 3.6	183 ± 17	347 ± 33
L1152	309.0827139	67.9421226	1	52.8 ± 1.5	130 ± 4	205 ± 4	228 ± 2	243 ± 16	259 ± 13	262 ± 13	597 ± 56	1080 ± 102
L1228	313.9044401	77.6387757	0.01	5.76 ± 0.12	7.18 ± 0.14	7.21 ± 0.15	5.69 ± 0.29	4.68 ± 0.22	3.78 ± 0.18	3.89 ± 0.18	4.58 ± 0.42	···
L1228	314.2782392	77.6155814	0.05	0.541 ± 0.036	1.78 ± 0.12	3.13 ± 0.19	7.81 ± 0.39	11.1 ± 0.5	13.9 ± 0.7	18.5 ± 0.9	271 ± 25	2240 ± 212
L1228	314.2831840	77.6165947	0.01	0.624 ± 0.014	1.91 ± 0.037	2.82 ± 0.060	3.16 ± 0.15	3.46 ± 0.16	3.28 ± 0.15	7.32 ± 0.34	154 ± 14	···
L1228	314.3039643	77.5953619	0.3	8.74 ± 0.20	58.5 ± 1.8	143 ± 3	32.8 ± 2.4	169 ± 11	359 ± 18	460 ± 38	1850 ± 174	7850 ± 730
L1228	314.3146768	77.5732263	0.01	0.141 ± 0.004	0.715 ± 0.017	1.79 ± 0.038	2.00 ± 0.10	2.41 ± 0.11	2.46 ± 0.12	2.94 ± 0.14	5.04 ± 0.47	···
L1228	314.3210184	77.6162648	0.1	5.14 ± 0.11	15.1 ± 0.3	26.1 ± 0.6	31.3 ± 1.5	38.0 ± 1.8	37.2 ± 1.7	42.1 ± 2.0	83.8 ± 7.7	334 ± 32
L1228[a]	314.6666221	77.4626441	0.1	1.17 ± 0.03	3.08 ± 0.07	6.53 ± 0.18	22.9 ± 1.1	···	24.7 ± 1.2	···	43.6 ± 4.2	···

[a] This object is not identified as 'YSOc' because it was not observed in IRAC2 and IRAC4. However, based on its location in Figure 4.9 and visual inspection we have included it here as a potential YSO.

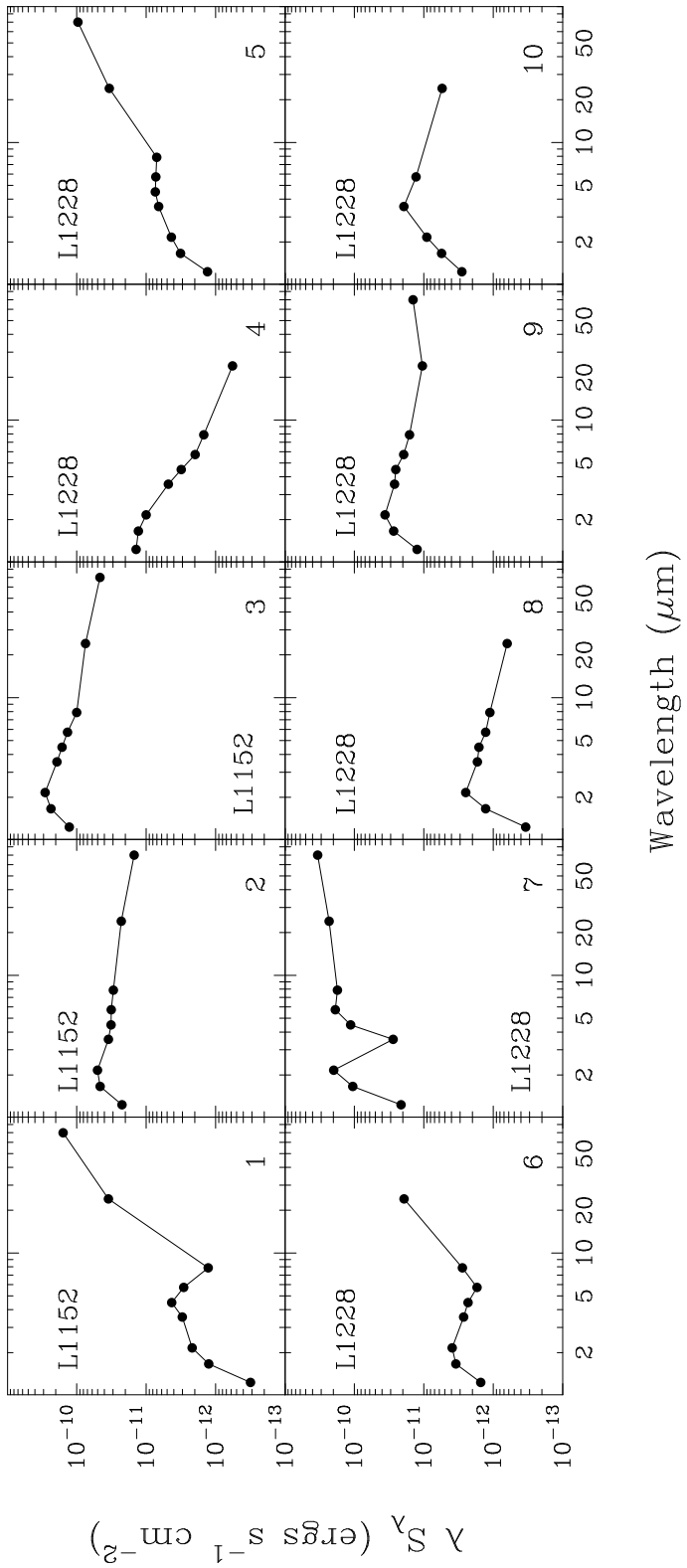

Figure 4.12: The spectral energy distribution for every source listed in Table 4.4. The numbers in the lower right corners correspond to the source number as listed in the table.

found our minimum χ^2 values were quite large, up to ~ 1000. These large χ^2 values are caused by the JHK_s bands where the models grossly under-predict the observed fluxes. All our "best-fit" models are heavily extincted, with $A_V \sim 50$. The model, with a spherical envelope, heavily extincts the near-infrared wavelengths. Our real sources undoubtedly have a complicated non-spherically smooth structure and therefore the JHK_s data, which are most sensitive to the A_V, are not being extincted by a full $A_v = 50$. Therefore, we computed a second χ^2 from the IRAC1-MIPS1 wavelengths. Except for the first YSO in L1152, the "best-fit" luminosity is the same regardless of which χ^2 we used. For the one exception, the luminosity only changes slightly, from 0.01 $L_\odot$ to 0.03 $L_\odot$.

L1152 YSOs

There are three YSOc sources in L1152. Two of these, IRAS 20353+6742 and IRAS 20359+6745, are previously known and both have outflows associated with them. IRAS 20353+6742 is the source embedded in the L1152 core and is the first source in the table. Only one lobe of the outflow is visible, but it can be seen from J - IRAC4. In Figure 4.9 this source is a Class I YSO, with a $K_s - [24]$ color of ~ 10.5. The second known source, IRAS 20359+6745, has a cone-shaped outflow next to the source that is visible in $J - K_s$, but not at longer wavelengths. This is the third listed source in Table 4.4. The Herbig-Haro object HH376A is located $2\farcm6$ to the southwest and has a bow-shock shape suggesting it came from the same outflow. Furthermore, HH376A is located along the apparent axis of the cone-shaped outflow. The remaining YSO is approximately $1'$ to the west of IRAS 20359+6745. This source is the second reddest YSO in Figure 4.9, right on the boundary between flat and Class II. We used SIMBAD[1] to look for references to this source, but did not find any.

[1] http://simbad.u-strasbg.fr/simbad/

L1228 YSOs

We identified seven potential YSOs in L1228. Six of these objects are classified as YSOc based on their colors § 2.5 while the remaining one cannot be classified as such because it appears outside of the area covered by IRAC2 and IRAC4. This object appears as a triangle in Figure 4.9 at $K_s - [24] = 7$. Five of the YSOc sources appear to be spatially coincident with the core of L1228. The brightest source, IRAS 20582+7724, is located in the center and has been previously observed. This is source 7 in Table 4.4. There is an outflow, HH 199, extending from this source in the East-West direction which is very prominent in K_s and all the *Spitzer* bands. The other YSOs have not been previously detected though Bally et al. (1995) inferred the existence of a second YSO in the core based on the discovery of a second outflow, HH 200.

The sixth YSOc source and the one non-YSOc source are not spatially associated with the extinction core. The YSOc source may simply be a background galaxy since its K_s magnitude places it just within the shaded contours in Figure 4.9 denoting background galaxies. This is less likely to be the case for the final source which is much brighter, $K_s = 12.5$. Neither of these two objects appears extended in the JHK_s nor the *Spitzer* images.

4.5 Extinction Maps

We started with our cleaned star catalogs for each core. These catalogs contain a line-of-sight extinction measurement calculated using the NICER technique (Lombardi & Alves 2001) and the WD5.5 dust model. Assuming a WD5.5 dust model, the conversion factor between the A_V and A_{K_s} is $A_V = 8.3A_{K_s}$. Our method for creating extinction maps has been detailed elsewhere (§ 3.5) so we will only give a brief outline here.

With line-of-sight extinction measurements for each source, these randomly distributed

samplings of the true extinction within the core need to be converted into a uniformly sampled map. We overlaid a grid on each region with an 18″ spacing between grid elements. At each grid position, an extinction value was computed as the average of the individual measurements within a 90″ radius. This average is weighted both by the uncertainty of each line-of-sight value and also by a Gaussian function with full width half maximum (FWHM) equal to 90″. Thus, our final maps have 90″ resolution with 5 pixels across the FWHM. Foreground star subtraction was also performed using the procedure in § 3.5.

We chose the 90″ resolution because this gave us a reasonable number of stars per cell for good statistics. The median number of stars per cell is $\sim 35-40$ for L204C-2, L1152, and L1155C-2 and 18 in L1228. The percentage of cells with less than or equal to 5 stars ranges from 6% in L1152 and L1155C-2 to 11% in L204C-2 and 14% in L1228. In Figures 4.13 - 4.16 we have plotted extinction maps of our four cores. The contours in each map start at 0.5 A_{K_s} in steps of 0.15 (3σ). We have also plotted the YSOc and Galc sources from our catalogs on the extinction maps. The dashed lines denote the region covered with IRAC1-4 and MIPS1. YSOc and Galc sources can only be classified in regions where all the *Spitzer* wavelengths are present.

The core of L204C-2 has a peak extinction of $A_{K_s} = 2.0$. Extending northward from the central core is a dust filament with two other broad, lower density extinction peaks. To the west of the core is a low density clump with a peak extinction of $A_{K_s} = 0.8$. Despite having the highest column density of any of our cores, we detect no YSOs in L204C-2. There is one Galc object located near the center of the core, however, as we discussed in § 4.4.3 this source has an SED consistent with a heavily extincted background star.

L1152 is a small core with peak $A_{K_s} = 1.7$. To the east are two additional separate extinction peaks. Both of these are of lower column density than the main core. There is one very bright YSOc embedded in the primary core, but slightly offset from the peak of extinction. One lobe of an outflow can be seen in *J* - IRAC4 extending from this YSO

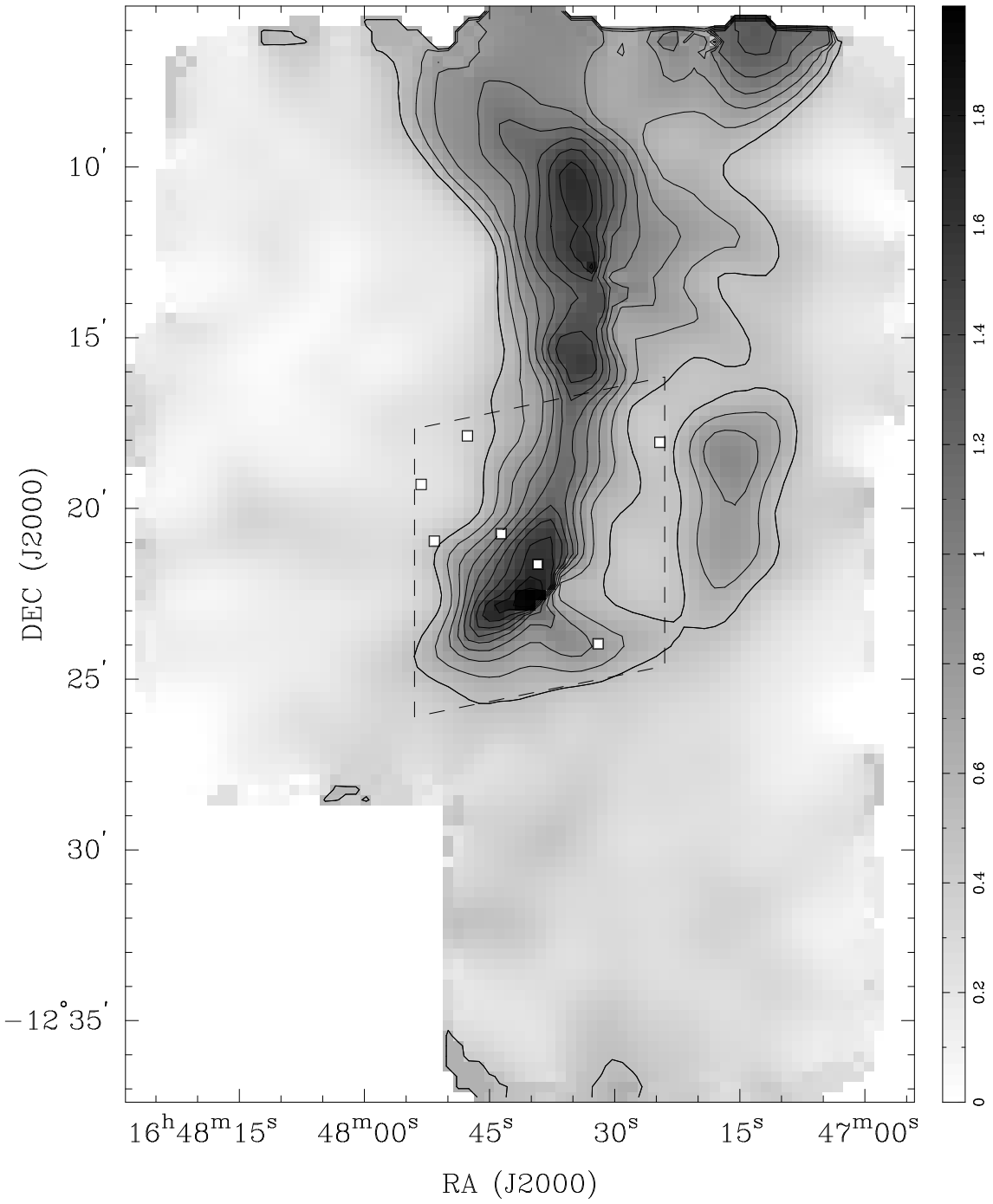

Figure 4.13: Extinction map of the core L204C-2 showing A_{K_s} within the observed region. The map has a resolution of 90″. See § 4.5 for a discussion on how this map was made. The maximum A_{K_s} value in the map is 2.0 magnitudes. Sources classified as YSOc (Galc) are shown as triangles (squares) on the image. The dashed region denotes the approximate area covered with both IRAC and MIPS.

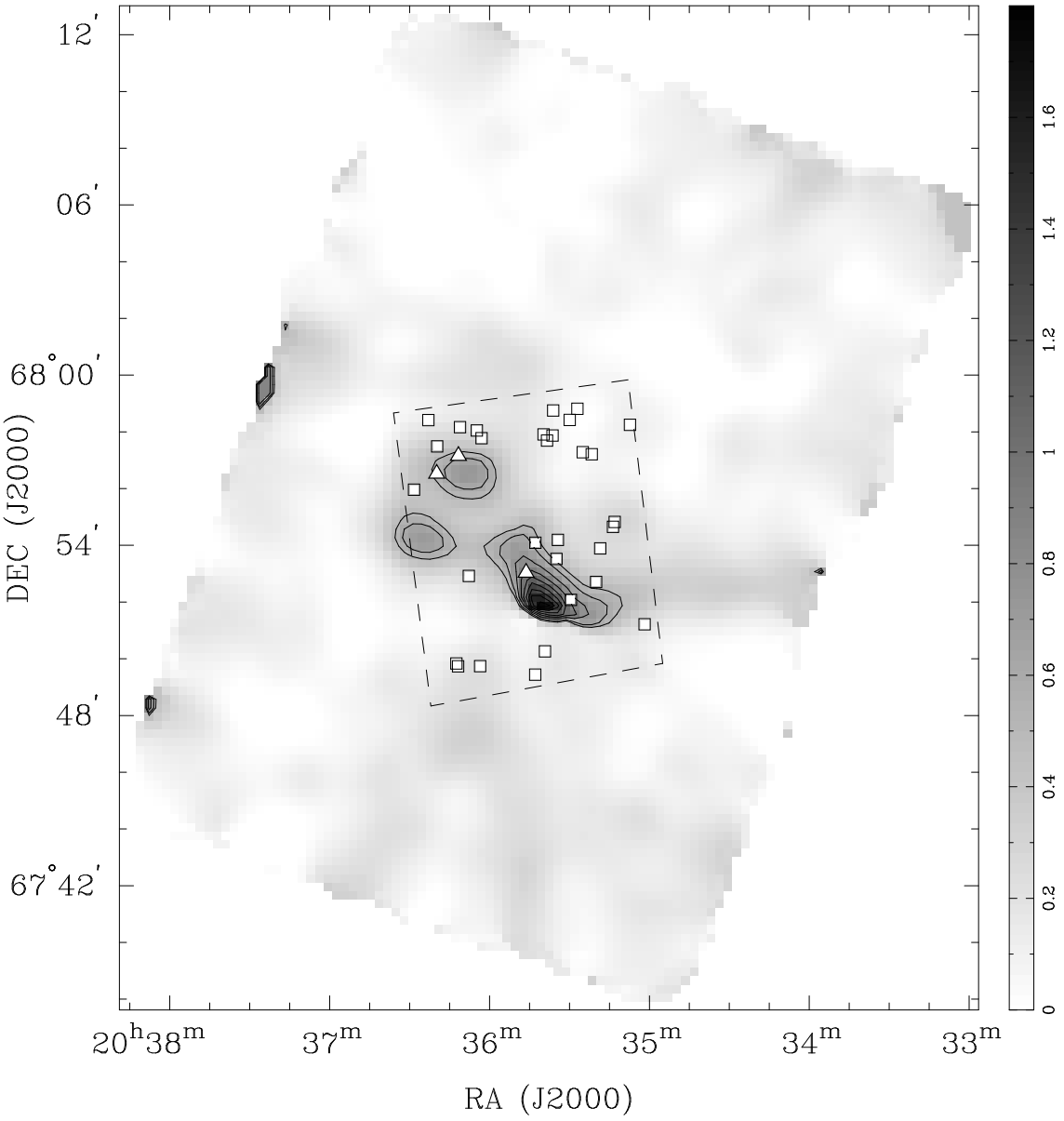

Figure 4.14: Extinction map of the core L1152 showing A_{K_s} within the observed region. The map has a resolution of 90″. See § 4.5 for a discussion on how this map was made. The maximum A_{K_s} value in the map is 1.7 magnitudes. Sources classified as YSOc (Galc) are shown as triangles (squares) on the image. The dashed region denotes the approximate area covered with both IRAC and MIPS.

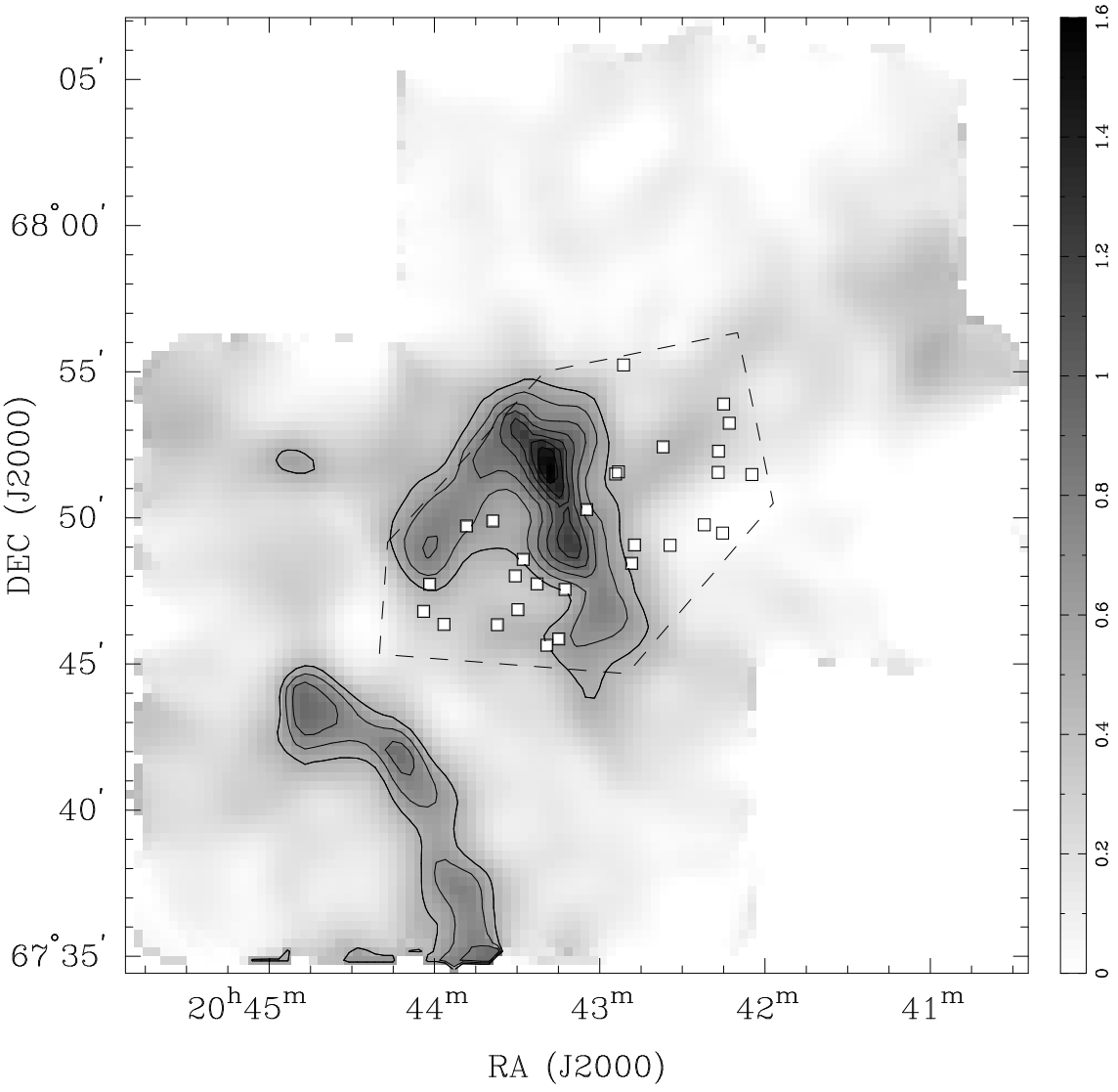

Figure 4.15: Extinction map of the core L1155C-2 showing A_{K_s} within the observed region. The map has a resolution of 90″. See §4.5 for a discussion on how this map was made. The maximum A_{K_s} value in the map is 1.6 magnitudes. Sources classified as YSOc (Galc) are shown as triangles (squares) on the image. The dashed region denotes the approximate area covered with both IRAC and MIPS.

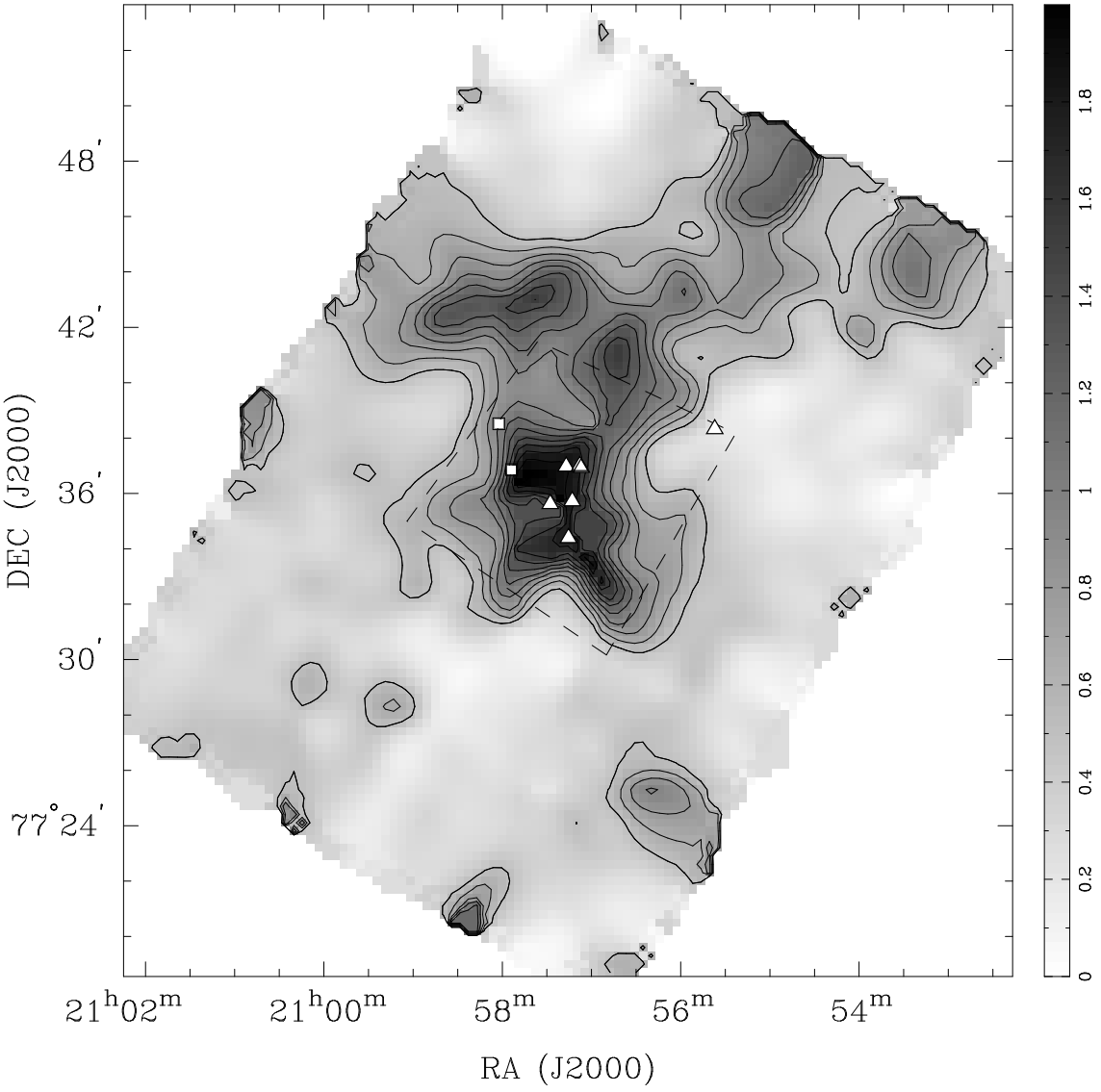

Figure 4.16: Extinction map of the core L1228 cloud showing A_{K_s} within the observed region. The map has a resolution of 90″. See § 4.5 for a discussion on how this map was made. The maximum A_{K_s} value in the map is 2.0 magnitudes. Sources classified as YSOc (Galc) are shown as triangles (squares) on the image. The dashed region denotes the approximate area covered with both IRAC and MIPS.

towards the peak of extinction. There are two other YSOs to the northeast, slightly offset from the northernmost extinction peak.

L1155C-2 is an extended core with two extinction peaks, the northernmost has a higher peak extinction. To the south is a separate dust filament which is part of L1155E. Like L204C-2, this core also appears starless.

The core of L1228 has a very complicated structure. The central core contains two extinction peaks and appears pinched in the middle. This may be more due to the low number of stars in the image rather than a true feature of region. There are several other extinction peaks nearby, mostly located to the North. L1228 has previously been classified as a starred core, and there are several YSOcs identified in the core. As discussed previously, most have not been detected previously.

4.6 The Extinction Law

4.6.1 Spatial Dependence of the Extinction Law

The χ^2 map of a core shows us the spatial distribution of the changes in the extinction law. This map is simply the sum of the difference between the observed extinction law at some wavelengths and that predicted by a given dust model. In this section we will construct such maps for our cores. Our method is discussed in more detail in §§ 3.6 and 3.6.1, though we will outline the basics here.

Calculating χ^2 is a two-step process. First, we need to calculate $C_{ext}(\lambda) = A_\lambda / A_{K_s}$, from our data. This can be done if we start from Equation 2.1 and re-arrange to solve for $C_{ext}(\lambda)$ while at the same time eliminating the need for K, the scaling factor for distance. This will give us Equation 3.7 which defines $C_{ext}(\lambda)$. χ^2 is then given by Equation 3.9.

We will compute χ^2 by summing over the IRAC bands alone. We will not use the JHK_s bands since these wavelengths were used when computing the extinction nor will

we use the MIPS1 (24 μm) data. As we shall see, the extinction law at 24 μm is frequently higher than any of our three dust models. Therefore, we have excluded this wavelength so as to not bias our χ^2 maps. Furthermore, we have only used those detections $\geq 3\sigma$ in each IRAC band when computing χ^2 and excluded any negative values for A_λ / A_{K_s} as unphysical. Finally, even though we computed the reduced χ^2 rather than the regular χ^2, we will frequently refer to the reduced χ^2 generically as 'χ^2'.

With this method we have the line-of-sight reduced χ^2 value for each star. To convert our line-of-sight measurements into a map, we followed the exact same procedure as we did when creating our A_{K_s} maps. In Figures 4.17 - 4.20 we have plotted maps of the extinction and χ^2 calculated using both the WD3.1 and WD5.5 dust models. The χ^2 maps have the same resolution as the extinction maps, 90″. For reference, the approximate size of the main core has been shown as a dashed rectangle in each figure. We have drawn our contours starting at $\chi^2 = 4$ because this is the approximate level at which there is a definite transition between the WD3.1 and WD5.5 dust models (see Figure 4.21). Further, with one degree of freedom there is approximately a 5% chance that $\chi^2 = 4$ would arise by chance. This probability decreases with more degrees of freedom.

The correspondence between the extinction, A_{K_s}, and the $R_V = 3.1$ χ^2 maps is quite remarkable. In all of our cores, the overall shape and the extinction peaks are mirrored in the WD3.1 χ^2 map. Many of the extinction features not associated with the cores also appear in the χ^2 map such as the dusty filament to the north of L204C-2, the two separate extinction peaks in L1152, and much of the structure in L1228. The picture is different in the $R_V = 5.5$ χ^2 maps. The two starless cores, L204C-2 and L1155C-2, are not visible in the WD5.5 χ^2 maps, while the two starred cores, L1152 and L1228, are seen. The low extinction region to the west of the main core in L204C-2 does not appear in either the WD3.1 or WD5.5 χ^2 maps.

To make a quantitative comparison between χ^2 and A_{K_s}, we binned our data in A_{K_s}

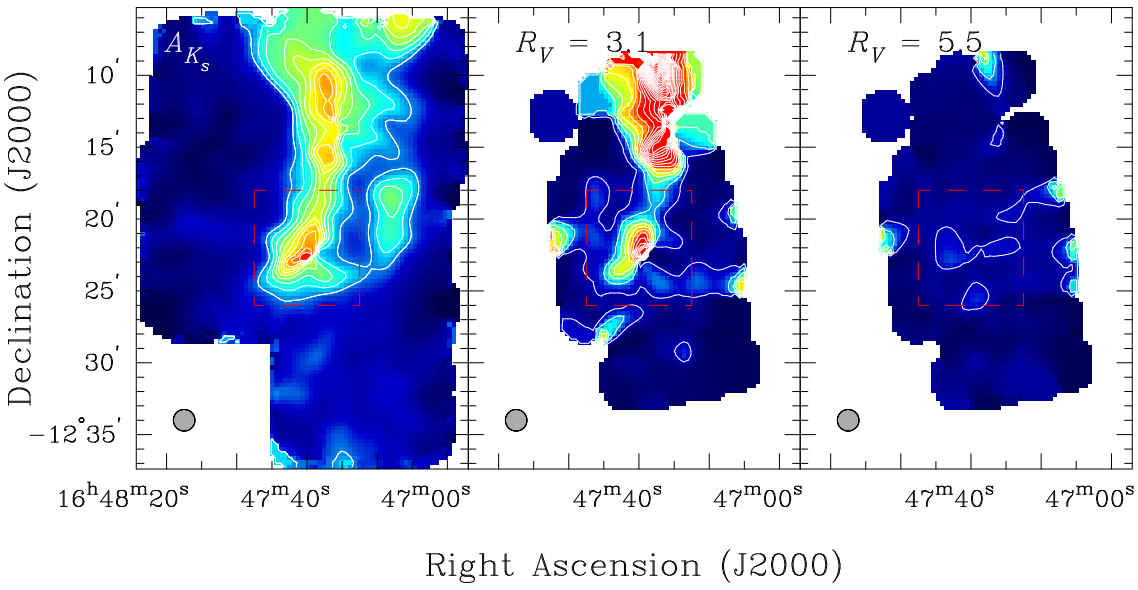

Figure 4.17: Map of the χ^2 values in the core L204C-2. The left panel shows the A_{K_s} map with contours starting at 0.5 magnitudes in steps of 0.15 mag. (3σ). The middle and right panels show χ^2 using either the Weingartner & Draine $R_V = 3.1$ (middle) or $R_V = 5.5$ (right) dust models. Contours start at 4 in steps of 4. The red box is the approximate region of the primary core. The grey circle in the lower left corner denotes the resolution of the maps, 90″.

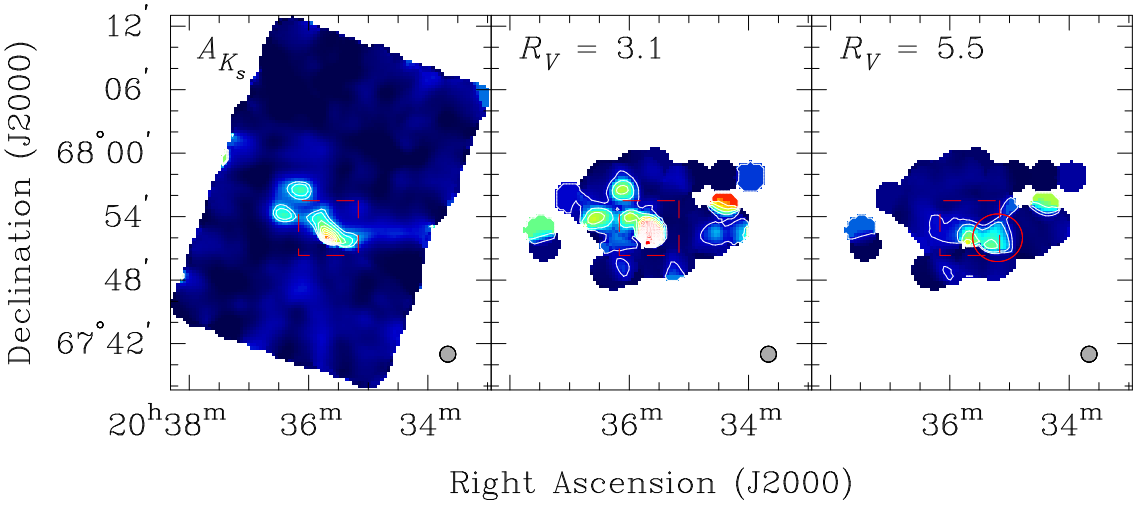

Figure 4.18: Map of the χ^2 values in the core L1152. The left panel shows the A_{K_s} map with contours starting at 0.5 magnitudes in steps of 0.15 mag. (3σ). The middle and right panels show χ^2 using either the Weingartner & Draine (2001) $R_V = 3.1$ (middle) or $R_V = 5.5$ (right) dust models. Contours start at 4 in steps of 4. The red box is the approximate region of the primary core. The grey circle in the lower right corner denotes the resolution of the maps, 90″.

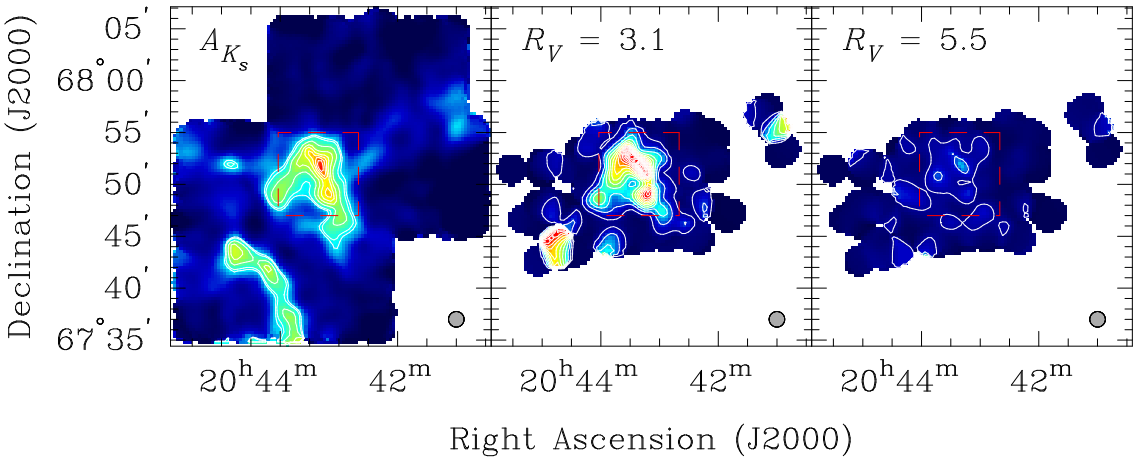

Figure 4.19: Map of the χ^2 values in the core L1155C-2. The left panel shows the A_{K_s} map with contours starting at 0.5 magnitudes in steps of 0.15 mag. (3σ). The middle and right panels show χ^2 using either the Weingartner & Draine (2001) $R_V = 3.1$ (middle) or $R_V = 5.5$ (right) dust models. Contours start at 4 in steps of 4. The red box is the approximate region of the primary core. The grey circle in the lower right corner denotes the resolution of the maps, 90″.

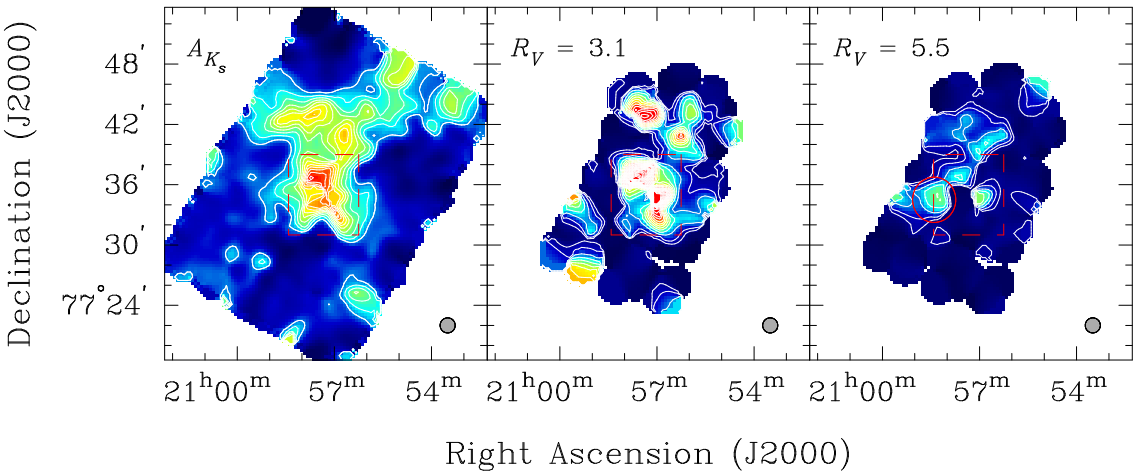

Figure 4.20: Map of the χ^2 values in the core L1228. The left panel shows the A_{K_s} map with contours starting at 0.5 magnitudes in steps of 0.15 mag. (3σ). The middle and right panels show χ^2 using either the Weingartner & Draine (2001) $R_V = 3.1$ (middle) or $R_V = 5.5$ (right) dust models. Contours start at 4 in steps of 4. The red box is the approximate region of the primary core. The grey circle in the lower right corner denotes the resolution of the maps, 90″.

and for each bin determined the average χ^2 with both the WD3.1 and WD5.5 models. Our results are shown in Figure 4.21. The $R_V = 3.1$ χ^2 curve is shown in black while $R_V = 5.5$ is shown in gray. At low extinction, $A_{K_s} \leq 0.6 - 1$, the $R_V = 5.5$ curve is very similar to the $R_V = 3.1$ one, suggesting that at low extinctions it is difficult to distinguish between these two models. This explains why most of the low A_{K_s} regions in Figures 4.17-4.20 appear very similar in both the $R_V = 3.1$ and $R_V = 5.5$ χ^2 maps. Above $A_{K_s} = 0.6 - 1$, the $R_V = 3.1$ curve rises sharply while the $R_V = 5.5$ curve stays roughly constant or increases only slightly. The highest A_{K_s} data point shows a sharp spike in the $R_V = 5.5$ reduced χ^2 for three of the cores. In each case, this is a single star.

The observed behavior in our χ^2 maps is consistent with the idea of grain growth in dense cores. Most regions of moderate to high extinction shows up in the $R_V = 3.1$ χ^2 map but not in the $R_V = 5.5$ χ^2 map. This suggests the WD3.1 extinction law is *not* valid in extincted regions because $\chi^2 = 4$ (the first contour level) corresponds to at least a 95% chance that the data do not fit the model. The differences in these two extinction laws is reflected by the differences in the properties of the dust models. The WD3.1 dust model was constructed to match observations of the diffuse ISM while also incorporating a population of small polycyclic aromatic hydrocarbons. This dust model produces an extinction law that fits the "standard" one (Rieke & Lebofsky 1985). In contrast to this, the $R_V = 5.5$ model has significantly fewer small silicate grains ($r < 0.1\,\mu$m) and significantly more large carbonaceous ones (maximum radius $\sim 10\times$ larger). This model produces a flatter extinction law in the mid-infrared and matches observations of the Galactic center (Lutz 1999; Lutz et al. 1996) and observations from the GLIMPSE *Spitzer* Legacy Science program (Indebetouw et al. 2005). A similar result was found by Kandori et al. (2003) who used optical and near-IR observations to map the distribution of A_V and R_V within the L1251 cloud. They found R_V values of $4 - 6$ in the dense high A_V areas of the cloud, compared to $R_V = 3.2$ in low A_V regions. At low extinctions it is not clear that the WD3.1

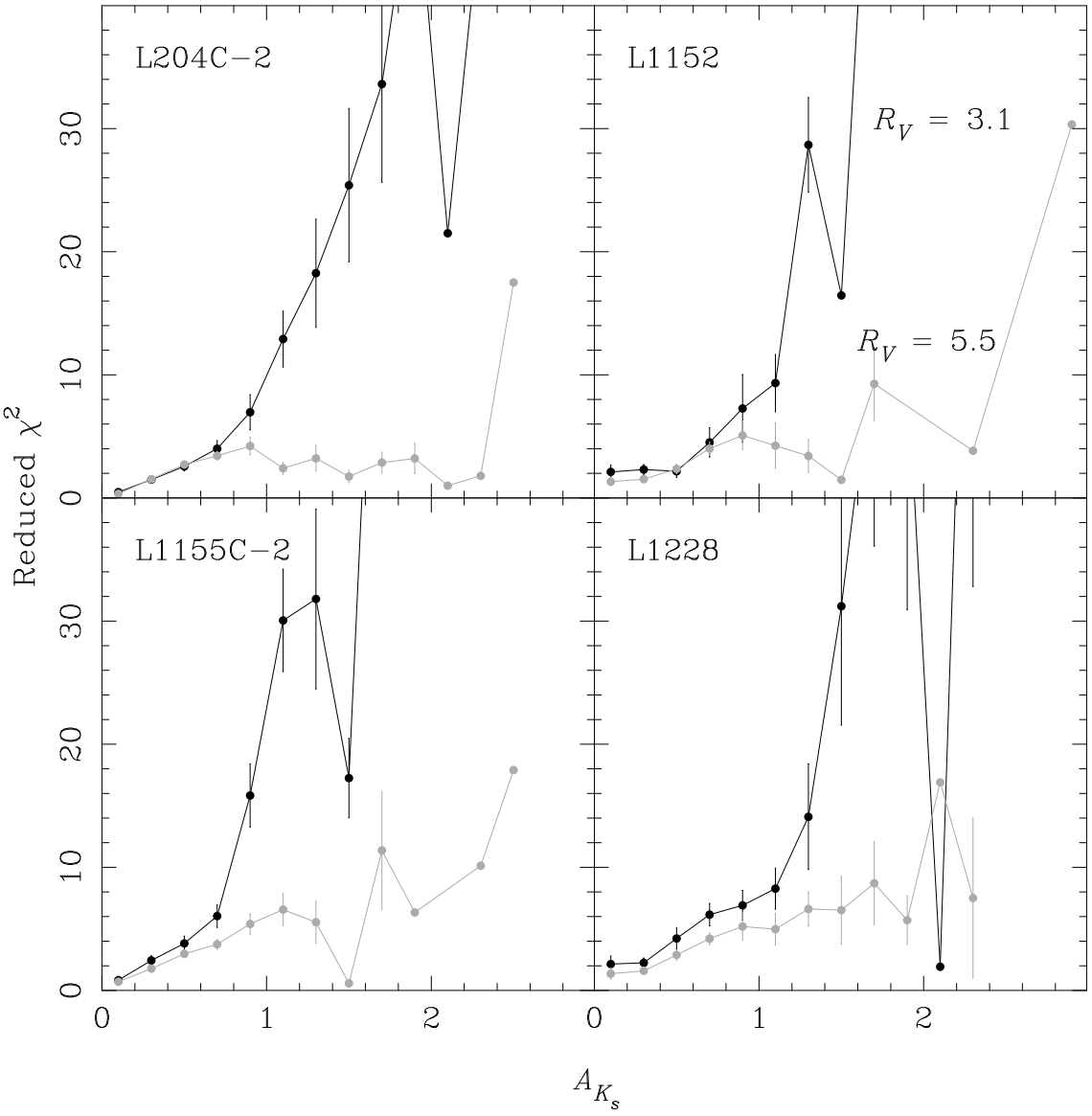

Figure 4.21: χ^2 versus A_{K_s} for the cores we observed. The WD3.1 χ^2 values are black, while the WD5.5 χ^2 values are light gray. The error bars shown are the standard deviations of the mean χ^2 value in each bin.

model provides a better fit to the data. This may be due to the fact that the majority of our sources are only detected in IRAC1 and/or IRAC2 where differences between the WD3.1 and WD5.5 dust models are smaller. Thus, when sources are averaged together for purposes of creating χ^2 maps, any extreme χ^2 values tend to be averaged out.

While most of our observations can be explained by the idea of grain growth within dense regions, in both L1152 and L1228 there are regions that appear strong in the WD5.5 χ^2 map yet are within the region of the core. Both of these cores have outflows associated with them which may be changing the dust sizes and compositions. In the next section, we explore changes in the observed extinction law as a function of wavelength and A_{K_s}. This will help us to understand exactly how the dust is changing within our cores.

4.6.2 Wavelength Dependence of the Extinction Law

As we saw in the last section, the extinction law is strongly dependent on A_{K_s}. Now we would like to explore how the extinction law changes versus wavelength. We started by binning the observed extinction law into three A_{K_s} bins: $0.15 \leq A_{K_s} < 0.5$, $0.5 \leq A_{K_s} < 1$, and $A_{K_s} \geq 1$. In each extinction bin, we have combined the individual $C_{ext}^{obs}(\lambda)$ measurements to obtain a weighted average value of A_λ / A_{K_s}. We excluded any negative values of $C_{ext}^{obs}(\lambda)$ as unphysical.

In Figure 4.22 we have plotted the observed extinction law as a function of wavelength. We have drawn errorbars for each data point as the larger of: the standard deviation of the mean or the minimum uncertainty due to systematic errors in the flux. These systematic errors were computed from Equation 3.8 and the uncertainties listed in §§ 2.4.1 and 2.4.2 and in Table 2.4. Note that the uncertainty is proportional to $A_{K_s}^{-1}$. We used the average value for A_{K_s} in each bin, weighted by our uncertainties in C_{ext}, to compute the systematic errors. Each row is a different core and each column is a different A_{K_s} bin. The left column covers the range of A_{K_s} from 0.15-0.5, the middle column is 0.5-1, and the

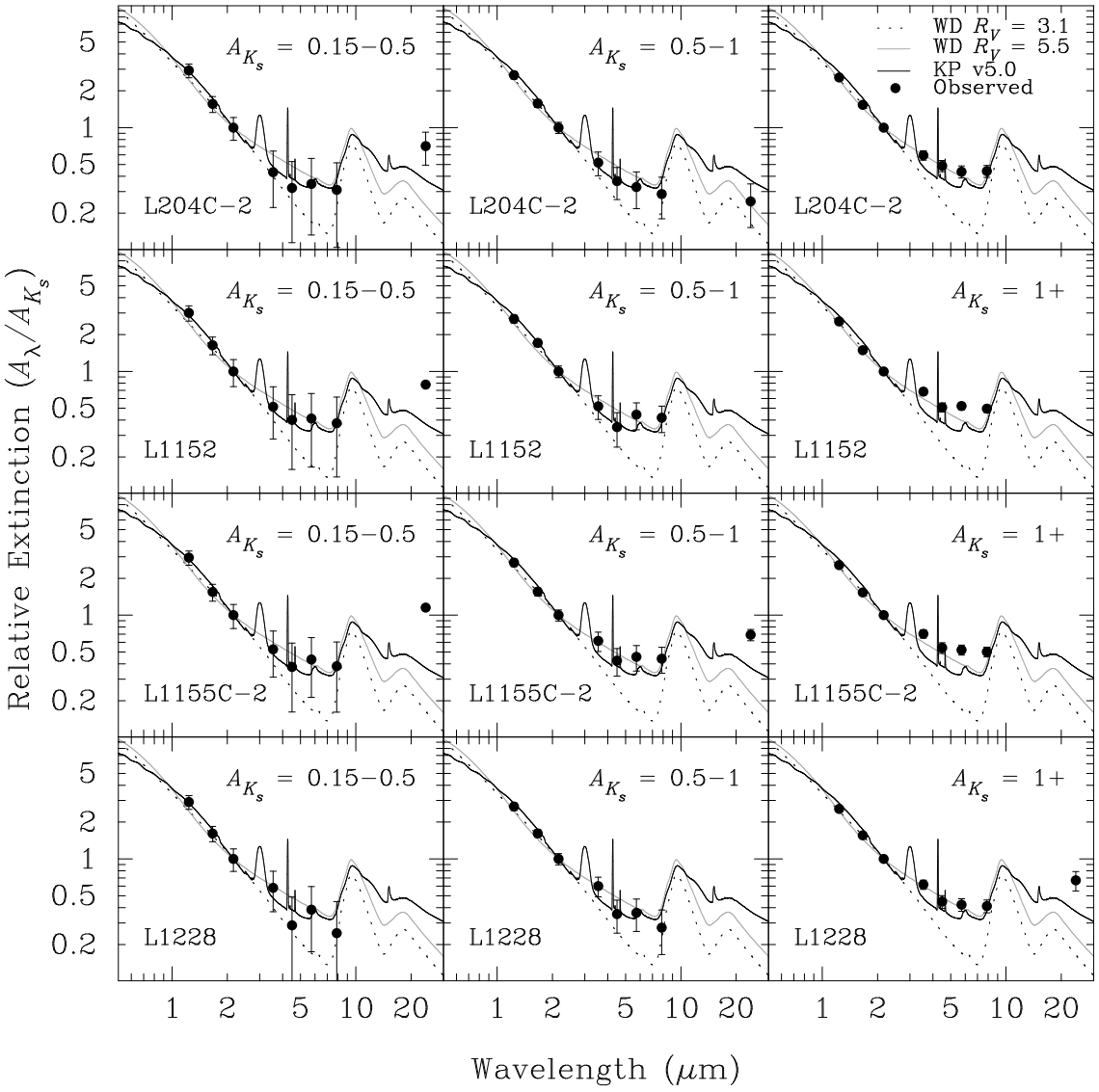

Figure 4.22: We have divided each of our cores into three A_{K_s} ranges and plotted the extinction law in each one. The left column is sources with $0 < A_{K_s} < 0.5$, the middle column is $0.5 \leq A_{K_s} < 1$, and the right column is $A_{K_s} \geq 1$.

right one is $A_{K_s} \geq 1$. In addition to the WD3.1 and WD5.5 models, we have plotted a third dust model (Pontoppidian et al., in prep). This dust model utilizes a simplified version of the WD3.1 dust model and adds icy mantles of from both water and also volatiles. Several ice absorption features can be seen in Figure 4.22, due to either H_2O, CO_2, or CO.

There is only a small difference in the extinction law between different A_{K_s} ranges and different cores. All four cores, in all three ranges of extinction, have a flatter extinction

law in the *Spitzer* IRAC bands that is more consistent with the WD5.5 or KP v5.0 extinction models. In the lowest extinction bin of L1228, the $A_{4.5}/A_{K_s}$ and A_8/A_{K_s} data points are lower than the values for the other IRAC bands. For $A_{K_s} = 0.15 - 0.5$, the errorbars are large enough such that we cannot statistically rule out a fit to the WD3.1 extinction law. These errorbars are the reason why our χ^2 maps show little difference between WD3.1 and WD5.5 at low extinction. For higher extinctions, the errorbars are smaller since the systematic errors are proportional to $A_{K_s}^{-1}$. Even though the systematic error bars can be quite large, the band-to-band relative uncertainties are much smaller which explains the smoothness in the extinction law predicted in the IRAC bands.

Our finding of a flat extinction law even at low A_{K_s} seems surprising since this contradicts our expectation that low extinction regions should correspond to the WD3.1 extinction law (e.g. Rieke & Lebofsky 1985). In chapter 3 we used the same methods to calculate the extinction law in three molecular clouds. There we found that for $0.15 \leq A_{K_s} < 0.5$ the extinction law was consistent with WD3.1. One major reason for this difference is that we are probing the column density along a line of sight and not the true density. Because isolated cores are factors of 10-30 smaller than molecular clouds, they have a correspondingly higher density than clouds for the same column density. Grain growth is a collisional process which proceeds more rapidly at higher densities. Hence, the grains in isolated cores quickly achieve at least modest grain growth compared to the WD3.1 dust grains.

At higher extinctions, our A_λ/A_{K_s} values increase slightly and the extinction law becomes even flatter. In two of the cores, L1152 and L1155C-2, the extinction law is higher than either WD5.5 or KP v5.0. This is primarily due to the 5.8 μm data point. Water ice has an absorption peak at 6.02 μm due to H-O-H bending (Gibb et al. 2004). The strength of $A_{5.8}/A_{K_s}$ suggests that water ice is present in these two cores. There is no correlation with star formation because L1152 contains three YSOs while L1155C-2 is starless.

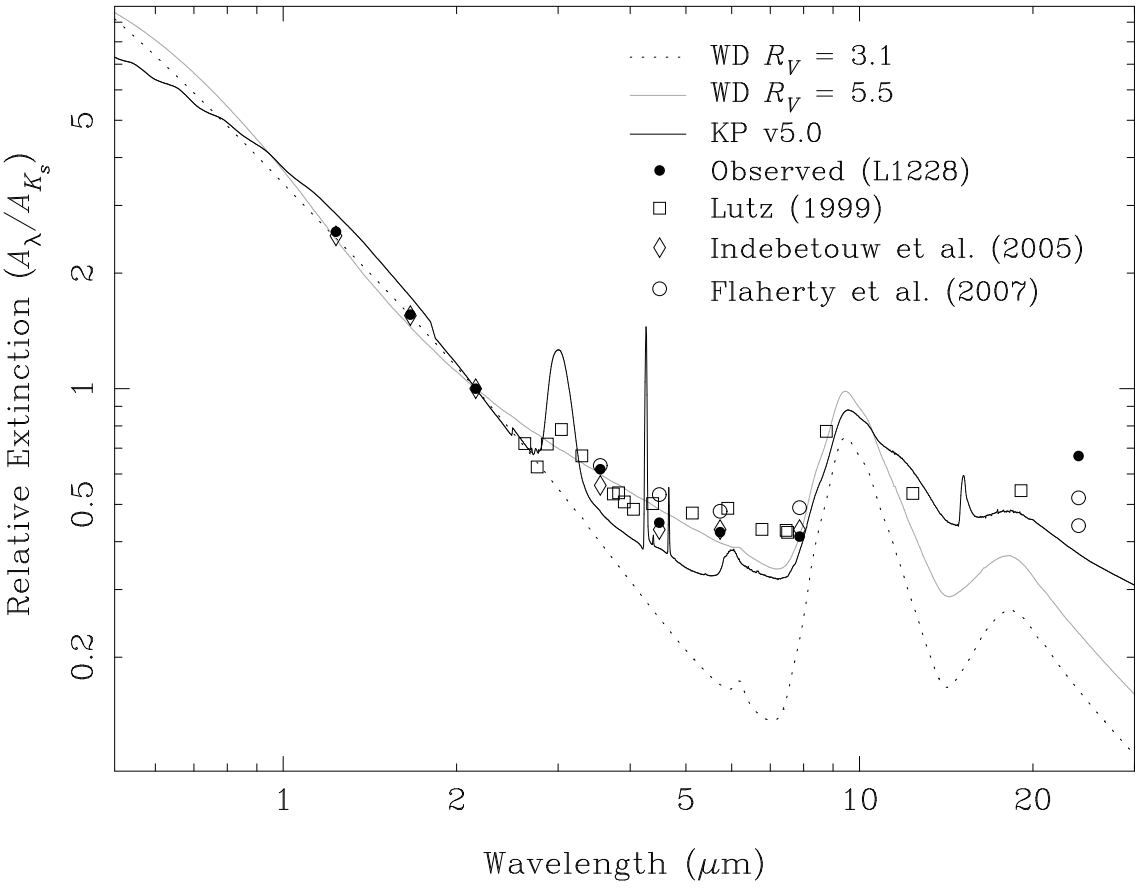

Figure 4.23: The extinction law measured by three different authors along with theoretical models. Our average extinction law for L204C-2 with $A_{K_s} \geq 1$ is shown with black circles. For clarity, we have suppressed the errorbars.

Indebetouw et al. (2005) and Flaherty et al. (2007) both used *Spitzer* observations to compute the IRAC extinction law from various sightlines. Furthermore, Lutz (1999) observed Hydrogen recombination lines towards the Galactic Center to derive the extinction law from $2.6 - 19\,\mu$m. All three of these papers computed a flat extinction law consistent with each other and consistent with our results. In Figure 4.23 we have plotted these authors' results along with our results for L1228 (the only core with a $24\,\mu$m data point in this extinction range).

Unlike in IRAC, our A_{24}/A_{K_s} data point is almost universally higher than predicted by any dust model. Four of our six points are approximately 0.7. Since there are only 15 $24\,\mu$m data points in all four cores with detections $\geq 3\sigma$, we may simply be dominated

by small number statistics. Another possibility is that our stellar model predicts a flux that is too high at 24 μm. From Table 2.4 we see that the average model for the cores predicts a flux at 24 μm of 0.013 ± 0.001 mJy (normalized to K_s). If we choose a slightly lower average model flux, 0.012 mJy, then the A_{24}/A_{K_s} data point is reduced by 15-50% for $0.15 \leq A_{K_s} < 0.5$ but only 8% for $A_{K_s} \geq 1$.

It may be possible to explain our values for A_{24}/A_{K_s} at low A_{K_s} by changing our average stellar model flux at 24 μm. However, changing the model has a smaller effect at high A_{K_s}, therefore it seems unlikely that this data point can be explained solely through the use of a different average stellar model. The extinction law has not been well-studied at 24 μm. Flaherty et al. (2007) measured it in two of their five regions and found values for A_{24}/A_{K_s} of 0.44 ± 0.02 and 0.52 ± 0.03. In our data, there is only one star in L1228 with $A_{K_s} \geq 1$. From this star, we derive a value for A_{24}/A_{K_s} of 0.668 ± 0.120. It is hard to draw conclusions from one star, but given slight changes to the average stellar model and the relatively large errorbars, our measurement is consistent with Flaherty et al. (2007) results. While KP v5.0 is close, no current dust model fits the value for A_{24}/A_{K_s}.

Finally, there were the two regions in L1152 and L1228 which appear in the $R_V = 5.5$ χ^2 maps. We speculated in the last section that the outflows present in these cores may be altering the dust properties. We selected all the sources circled in red in Figures 4.18 and 4.20 and plotted the average extinction law for each in Figure 4.24. The extinction law in both of these regions is slightly shallower than the WD3.1 dust model. This is likely due to the shock from the outflows in these cores which are destroying the dust grains and clearing out a cavity.

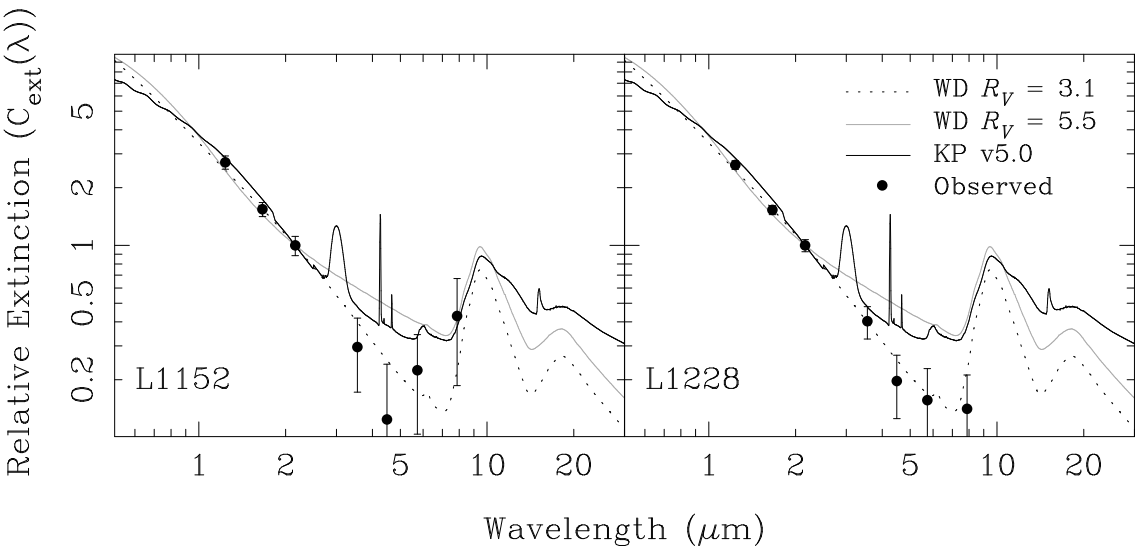

Figure 4.24: The averaged extinction laws for the sources near the outflows in L1152 (left) and L1228 (right). Three different dust models are plotted for comparison. For L1152, we only have one data point in IRAC4 which explains the relatively large errorbar. All other errorbars are the larger of: the standard deviation of the mean or the minimum uncertainty due to systematic errors in the flux.

4.6.3 Changes in the Near-Infrared Extinction Law

In this chapter, we have assumed a constant extinction law in the near-IR that can be represented by the WD5.5 dust model. We did this on purpose so we could directly compare our results with those of other authors (who assumed the same extinction law), for easy comparison between different cores, and because numerous observations support an extinction similar very similar to this one in the near infrared (Draine 2003, and references therein). In the near-infrared, the extinction law can be fit as a power law, $A_\lambda \propto \lambda^{-\beta}$. Our WD5.5 model has $\beta \approx 1.6$. We will investigate the effect of different near-IR extinction laws on our results in this section.

As we discussed in § 3.6.3, the JHK_s bands can be used to derive the extinction law in the near-infrared by fitting a straight line to a plot of $J-H$ versus $H-K_s$. Figure 4.25 shows this plot for our cores with the best-fit slope in each core.

The sparsity of points with large reddening in our cores makes it difficult to obtain

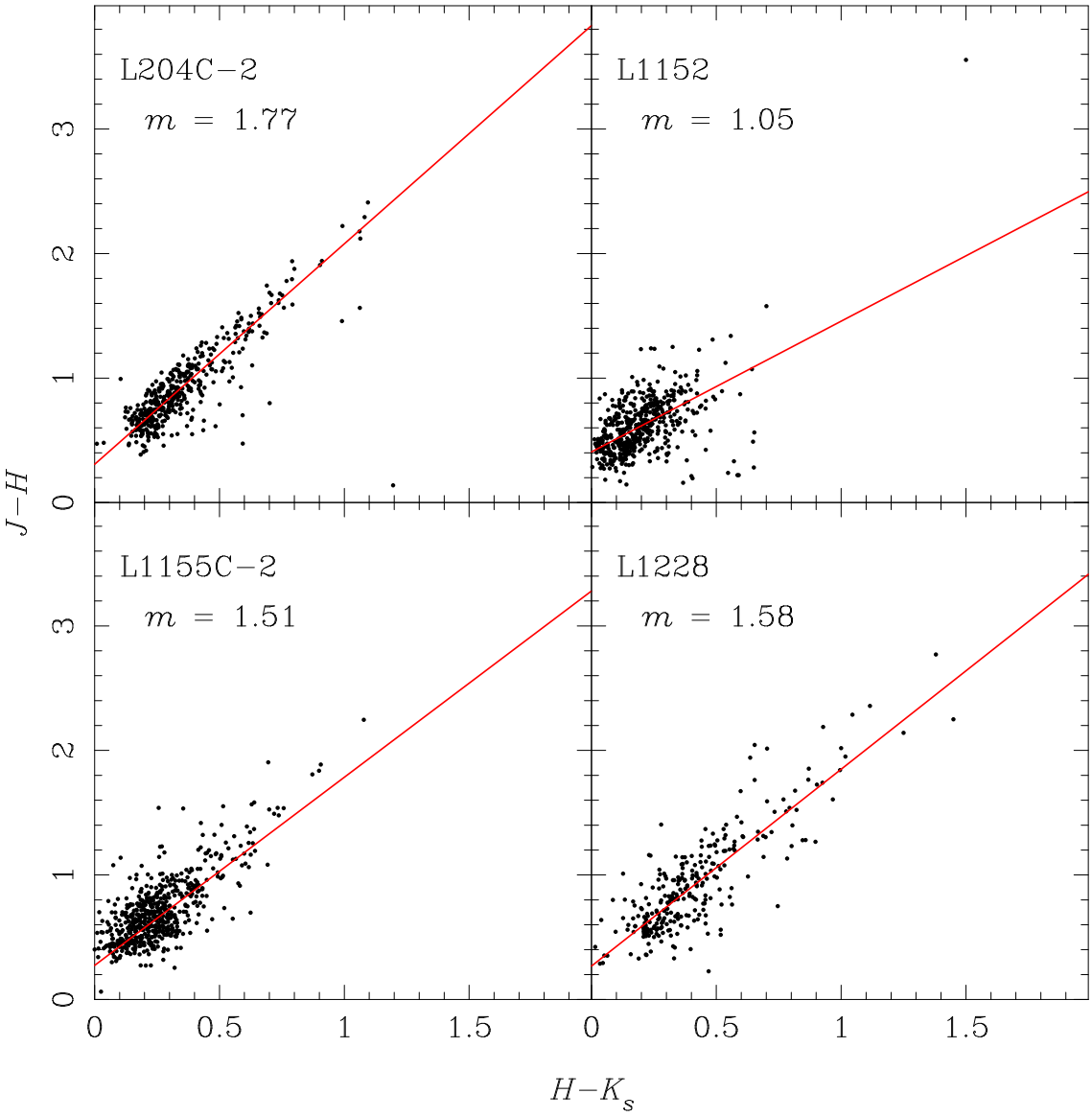

Figure 4.25: $J-H$ versus $H-K_s$ for all sources brighter than 15th magnitude at K_s. The best-fit line for each core is shown with the specified slope.

reasonable best-fit lines. L204C-2, the core with the best correlation, has a slope of 1.77, which corresponds to $\beta = 1.58$. L1155C-2 and L1228 have moderately good fits with slopes of 1.51 and 1.58 ($\beta = 1.02, 1.18$), but L1152 has too few reddened stars to obtain any sort of reasonable slope for the data. In all of our cores, the data are visually consistent with the slope of 1.77 found for L204C-2. Following § 3.6.3, we have plotted in Figure 4.26 our observed extinction law in L204C-2 for three different values of β: 1.4, 1.6, and

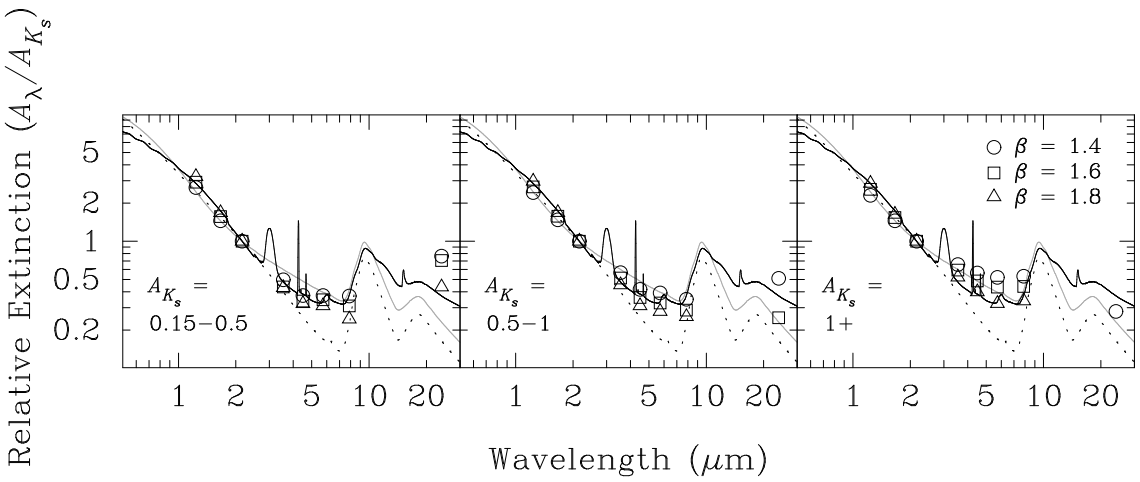

Figure 4.26: The extinction law in L204C-2 using three different extinction laws for the near-infrared JHK_s bands. These extinction laws are of the form $A_\lambda \propto \lambda^{-\beta}$.

1.8. This range of β corresponds to a relatively small range of slopes: 1.68-1.88.

Changing β has a measurable impact on our computed extinction law in the IRAC bands. In general, our extinction law is flatter for lower values of β. Between $\beta = 1.4$ and $\beta = 1.6$, the extinction law in the IRAC bands changes by $10-15\%$ and between $\beta = 1.6$ and $\beta = 1.8$, the extinction law changes by $15-20\%$. Based on this analysis, our assumption of the WD3.1 model $\beta = 1.6$ introduces a systematic error of $10-15\%$ in our computed extinction law.

4.7 Conclusions

As sites of current or potential future star formation, studying the dust properties of isolated cores can tell us about the physical conditions within the cores. We have observed four cores, L204C-2, L1152, L1155C-2, and L1228 with both deep JHK_s and *Spitzer* observations. Two of these, L1152 and L1228, are previously known to harbor protostars, while the other two are starless. This determination was based on the presence or lack of IRAS sources within the cores (Lee et al. 1999). Therefore we have a small sample illustrating both the initial and later stages of star formation.

All four of our cores contain a number of bright 24 μm sources. These sources can be very exciting since young stellar objects exhibit infrared excesses due to reprocessing of starlight by the disks and envelopes surrounding them. However, other objects such as asteroids and background galaxies may also be detected at 24 μm. After removing these objects from our catalogs, we were left with 10 YSO candidates, 3 in L1152 and 7 in L1228. We did not detect any YSOc sources in either L204C-2 or L1155C-2. Any YSOc objects would have to be fainter than our 3σ detection limit of $\sim$ 12.5 magnitudes at 24 μm.

We have also created extinction maps to trace the column density of the cores. Surprisingly, the peak of the dust extinction does not necessarily correspond to the location of the YSOs. In L1152, the bulk of the core is located to the south of IRAS 20353+6742. The situation is different in L1228, where the majority of the YSOs are located at the central extinction peak. Note that there are several other extinction peaks in this core, none of which have any YSOs associated with them. There is one possible YSO in L1228 which is *not* associated with the core. Only the primary YSO in this core has been previously detected.

The presence of YSOs in a core may alter the dust properties compared to starless cores as grain growth occurs and ice mantles on grains are heated and evaporate. To examine this in depth, we created a reduced χ^2 statistic that sums the difference between the observed extinction law and that produced by a given dust model for each source, either WD3.1 or WD5.5. We then created a map of the WD3.1 and WD5.5 χ^2 within each core. Below $A_{K_s} \lesssim 0.6 - 1$, the WD3.1 and WD5.5 χ^2 values are very similar. Above this extinction, the WD3.1 χ^2 rises sharply while WD5.5 tends to stay the same or increase only moderately.

We also binned our data in A_{K_s} and plotted the observed extinction law in each bin. Even at the lowest extinctions, our observed extinction law in the mid-infrared is fairly

flat and more consistent with WD5.5 or KP v5.0 than with WD3.1, though the systematic errorbars are large enough to incorporate the WD3.1 law as well. At higher extinctions, A_λ/A_{K_s} does not significantly change in most cores except for $A_{K_s} \geq 1$ in L1152 and L1155C-2 where the observed law is flatter than WD5.5 and KP v5.0. This flatness could be explained by water ice in these two cores. Since one core, L1152, is starred while the other is starless, the presence or lack of water ice does not appear correlated with star formation.

At 24 μm, the extinction law appears significantly higher than previous results from Flaherty et al. (2007). Slight changes in our average stellar model can dramatically lower A_{24}/A_{K_s} and bring them into line with Flaherty et al. (2007) results. However, A_{24}/A_{K_s} remains higher than the values predicted by any current dust models.

Finally, the outflows in L1152 and L1228 seem to have an impact on the dust properties within the cores. The regions near the observed tips of the outflows show evidence of dust clearing which results in an extinction law more similar to WD3.1 than WD5.5.

Chapter 5

Conclusions

5.1 Results

In this dissertation we investigated the changes in dust properties within molecular clouds and cores. We mapped regions within three molecular clouds and also four isolated cores from $1.25 - 24\,\mu$m. We derived line-of-sight extinctions towards each background star and convolved these to create extinction maps. We also computed the observed extinction law from $3.6 - 24\,\mu$m for each background star. We compared our observed extinction law to three theoretical models, each chosen to model various limits in the interstellar medium. The Weingartner & Draine (2001) $R_V = 3.1$ model was chosen to represent the diffuse ISM, their $R_V = 5.5$ model represents grain growth in denser cloud regions, and finally the Pontoppidian et al. (in prep.) model, version 5.0, was chosen since it incorporates icy mantles on dust grains. We can now answer the three questions we posed in § 1.5.

Question 1: How are dust grain sizes and compositions related to the extinction?

Short answer: There is a strong correlation between grain growth and the

column density of material. Ices appear in some of the denser regions.

In both the clouds and the cores, we computed a reduced χ^2 statistic using both the Weingartner & Draine (2001) $R_V = 3.1$ and $R_V = 5.5$ dust models. Below $A_{K_s} \sim 1$ these two models have very similar χ^2 values making it difficult to distinguish between them. Above $A_{K_s} \sim 1$ the $R_V = 3.1$ χ^2 values increase sharply while the $R_V = 5.5$ values remain roughly constant or only increase modestly. Furthermore, we created spatial maps of χ^2 using the same methodology and with the same resolution as our extinction maps. In all our regions the high extinction regions also appear in the $R_V = 3.1$ χ^2 maps while these same regions are weaker or not observed in the $R_V = 5.5$ χ^2 maps.

These two models, $R_V = 3.1$ and $R_V = 5.5$, have different dust properties, as shown in Figure 1.2. The $R_V = 3.1$ model was designed to fit observations of the diffuse interstellar medium. In $R_V = 5.5$ the carbonaceous grains can be up to $10\times$ larger than in $R_V = 3.1$. Furthermore, the number of silicate grains smaller than $0.1\,\mu$m is significantly reduced in $R_V = 5.5$.

We also computed the average extinction law in different ranges of extinction. The general trend is that the extinction law from $3.6 - 8\,\mu$m flattens as extinction increases. This agrees with our earlier evidence for grain growth. The degree of flattening is different between clouds and cores. In our clouds, the diffuse regions are very similar to the Weingartner & Draine $R_V = 3.1$ dust model. In our cores, however, even the low A_{K_s} regions have a relatively flat extinction law. This is because extinction traces the column density of material rather than the true density. Since cores are physically several orders of magnitude smaller in size than molecular clouds, cores can have a higher density compared to clouds for the same extinction (column density). In some regions, L1152, L1155C-2, Serpens, and Perseus, the extinction law in the densest regions (highest extinctions) is even higher than $R_V = 5.5$, most noticeably at $5.8\,\mu$m. This can be explained by the presence of water ice, which has an H-O-H vibrational line at $6.02\,\mu$m (Gibb et al.

2004).

There is one region within Perseus which does not follow the observed trend, i.e. higher extinction equals a flatter extinction law. This region has an extinction law higher than observed in any other region. This region has a relatively modest extinction ($A_{K_s} = 0.62$), so it seems unlikely that grain growth or ices are contributing to the flatter extinction law. We do not have an explanation for this region.

Question 2: How do star forming regions impact dust properties?

Short answer: Except for molecular outflows, the presence of star formation alone has little impact on the dust properties.

Our observations were designed to cover a range of environments including star forming regions. In our clouds, we observed a region near L1688 in Ophiuchus, the cluster of YSOs identified as IRAS 03388+3139 (IC348 West) in Perseus, and 'Cluster B' in Serpens. Two of our cores are identified as 'starred', meaning they contain embedded protostars, and two are starless. There is no consistent picture of the extinction law changing due to the presence or lack of star formation in any cloud or core. This is perhaps not so surprising because the regions near enough to YSOs for there to be significant heating of the dust grains (to temperatures $\gtrsim$ 100K) are below the resolution of our χ^2 maps. Our maps have a resolution of $30''$ in Serpens and $90''$ in all other clouds. In Tables 3.1 and 4.2 we listed the distances to each cloud and core. Using these values, our resolution ranges from $\sim 7,800$ AU in Serpens to almost $30,000$ AU in L1152 and L1155C-2. We do observe evidence for water ice in some of the highest extinction regions, but there is no correlation between the presence or lack of water ice and the occurence of star formation.

In L1152 and L1228, molecular outflows appear to clear-out or destroy the larger dust grains leaving a cavity where the extinction law is more consistent with the $R_V = 3.1$ dust model. This is a deviation from the rest of the core, where the extinction law is closer to $R_V = 5.5$, even at low extinctions.

Question 3: Do the dust properties differ between clouds, between cores, and between clouds and cores?

Short answer: All regions show the same trend where higher extinction = flatter extinction law, but there are some differences in specific regions and larger differences between the clouds and the cores.

As we discussed in our answer to Question 1, all our regions have a correlation between the column density and the extinction law. This general trend is consistent with grain growth in denser regions. There are, however, some differences. For $0.15 \leq A_{K_s} < 0.5$, both Perseus and Serpens have an $A_{5.8}/A_{K_s}$ data point that is higher than the $R_V = 3.1$ model. This behavior is not found for low extinctions in Ophiuchus. The size of the errorbars for this range of extinction make this result statistically insignificant. At intermediate ranges of extinction, the extinction law is similar between all three clouds with dust properties consistent with the WD5.5 model. Again as we discussed in our answer to Question 1, ices appear in the densest regions of Perseus and Serpens, but not in Ophiuchus.

There is a large difference at low extinctions between our clouds and cores. For the same range of extinction, $0.15 \leq A_{K_s} < 0.5$, the extinction law in the IRAC bands for the cores is much flatter than in the clouds and consistent with $R_V = 5.5$. This is caused by the difference in size between isolated cores and molecular clouds. Isolated cores are $\sim 10-30\times$ smaller than clouds so the same column density of material will correspond to a denser region in a core compared to a cloud. Because grain growth is a collisonal process and the isolated cores are denser, it is reasonable to assume the dust grains have experienced at least some grain growth compared to the WD3.1 dust grains. The four cores have a similar extinction law for all but the highest extinctions. L1152 and L1155C-2 both show evidence for water ice, but L204C-2 and L1228 do not.

5.2 Future Work

We have shown in this dissertation that the dust properties within clouds and cores change in a manner consistent with grain growth and with ices forming in some of the denser regions. This is consistent with many previous results, though there are a few areas where questions remain.

One of the biggest remaining questions is the nature of the extinction law at 24 μm. Data is sparse but Lutz (1999) and Flaherty et al. (2007) suggest an extinction law much flatter than one predicted by current dust models. Our results agree with this conclusion and also seem to suggest that A_{24}/A_{K_s} decreases as extinction increases. This behavior is contrary to the idea of grain growth in denser regions. More high-quality detections of stars at 24 μm are needed to obtain better statistics. With *Spitzer* Legacy Science Programs such as c2d and Gould's Belt, these data have been and are currently being taken and will become available to the community in the near future.

In this thesis, we used the extinction maps of clouds to investigate the possible existence of sub-structure and to compute a simple one-point correlation statistic, the power density function, which tells us about the presence of turbulence in the clouds. It might be useful to create a two-point correlation function and see if it adds to our understanding of the structure in clouds.

Finally, our anomalous region in Perseus shows that some regions do not fit standard assumptions about what the dust properties should be in molecular clouds. Since we have only discovered one such region in all three clouds, it seems more likely to be caused by stars or other objects with unusual photometry rather than a property of the cloud. With the larger sample of c2d and Gould's Belt data available, we would like to search for any other such anomalies in other clouds. If other examples are found, spectra would then be useful in determining the properties of the clouds which are causing the flat extinction

law.

Bibliography

Alves, J., Lada, C. J., Lada, E. A., Kenyon, S. J., & Phelps, R. 1998, ApJ, 506, 292

Alves, J. F., Lada, C. J., & Lada, E. A. 2001, Nature, 409, 159

Bally, J., Devine, D., Fesen, R. A., & Lane, A. P. 1995, ApJ, 454, 345

Benjamin, R. A., Churchwell, E., Babler, B. L., Bania, T. M., Clemens, D. P., Cohen, M., Dickey, J. M., Indebetouw, R., Jackson, J. M., Kobulnicky, H. A., Lazarian, A., Marston, A. P., Mathis, J. S., Meade, M. R., Seager, S., Stolovy, S. R., Watson, C., Whitney, B. A., Wolff, M. J., & Wolfire, M. G. 2003, PASP, 115, 953

Bohlin, R. C., Savage, B. D., & Drake, J. F. 1978, ApJ, 224, 132

Bok, B. J., Lawrence, R. S., & Menon, T. K. 1955, PASP, 67, 108

Cardelli, J. A., Clayton, G. C., & Mathis, J. S. 1989, ApJ, 345, 245

Cox, A. N. 2000, Allen's astrophysical quantities (Allen's astrophysical quantities, 4th ed. Publisher: New York: AIP Press; Springer, 2000. Editedy by Arthur N. Cox. ISBN: 0387987460)

de Geus, E. J., de Zeeuw, P. T., & Lub, J. 1989, A&A, 216, 44

Draine, B. T. 2003, ARA&A, 41, 241

Draine, B. T. & Anderson, N. 1985, ApJ, 292, 494

Eikenberry, S., Stolte, A., & Raines, N. 2005, private communication

Elston, R. 1998, in Proc. SPIE Vol. 3354, p. 404-413, Infrared Astronomical Instrumentation, Albert M. Fowler; Ed., ed. A. M. Fowler, 404–413

Enoch, M. L., Young, K. E., Glenn, J., Evans, II, N. J., Golwala, S., Sargent, A. I., Harvey, P., Aguirre, J., Goldin, A., Haig, D., Huard, T. L., Lange, A., Laurent, G., Maloney, P., Mauskopf, P., Rossinot, P., & Sayers, J. 2006, ApJ, 638, 293, arXiv:arXiv:astro-ph/0510202

Evans, II, N. J. 1999, ARA&A, 37, 311, arXiv:astro-ph/9905050

Evans, II, N. J., Allen, L. E., Blake, G. A., Boogert, A. C. A., Bourke, T., Harvey, P. M., Kessler, J. E., Koerner, D. W., Lee, C. W., Mundy, L. G., Myers, P. C., Padgett, D. L., Pontoppidan, K., Sargent, A. I., Stapelfeldt, K. R., van Dishoeck, E. F., Young, C. H., & Young, K. E. 2003, PASP, 115, 965, arXiv:astro-ph/0305127

Evans, II, N. J., Harvey, P. M., Dunham, M. M., Mundy, L. G., Lai, S.-P., Chapman, N. L., Huard, T., Brooke, T. Y., Enoch, M., & Stapelfeldt, K. R. 2007, Final Delivery of Data from the c2d Legacy Project: IRAC and MIPS, Tech. rep.

Fazio, G. G., Hora, J. L., Allen, L. E., Ashby, M. L. N., Barmby, P., Deutsch, L. K., Huang, J.-S., Kleiner, S., Marengo, M., Megeath, S. T., Melnick, G. J., Pahre, M. A., Patten, B. M., Polizotti, J., Smith, H. A., Taylor, R. S., Wang, Z., Willner, S. P., Hoffmann, W. F., Pipher, J. L., Forrest, W. J., McMurty, C. W., McCreight, C. R., McKelvey, M. E., McMurray, R. E., Koch, D. G., Moseley, S. H., Arendt, R. G., Mentzell, J. E., Marx, C. T., Losch, P., Mayman, P., Eichhorn, W., Krebs, D., Jhabvala, M., Gezari, D. Y., Fixsen, D. J., Flores, J., Shakoorzadeh, K., Jungo, R., Hakun, C., Workman, L., Karpati, G., Kichak, R., Whitley, R., Mann, S., Tollestrup, E. V., Eisenhardt, P., Stern, D., Gorjian, V., Bhattacharya, B., Carey, S., Nelson, B. O., Glaccum, W. J., Lacy, M., Lowrance, P. J., Laine, S., Reach, W. T., Stauffer, J. A., Surace, J. A., Wilson, G., Wright, E. L., Hoffman, A., Domingo, G., & Cohen, M. 2004, ApJS, 154, 10, arXiv:astro-ph/0405616

Flaherty, K. M., Pipher, J. L., Megeath, S. T., Winston, E. M., Gutermuth, R. A., Muzerolle, J., Allen, L. E., & Fazio, G. G. 2007, ApJ, 663, 1069

Gibb, E. L., Whittet, D. C. B., Boogert, A. C. A., & Tielens, A. G. G. M. 2004, ApJS, 151, 35

Greene, T. P., Wilking, B. A., Andre, P., Young, E. T., & Lada, C. J. 1994, ApJ, 434, 614

Harvey, D. W. A., Wilner, D. J., Lada, C. J., Myers, P. C., & Alves, J. F. 2003, ApJ, 598, 1112, arXiv:arXiv:astro-ph/0308143

Harvey, D. W. A., Wilner, D. J., Lada, C. J., Myers, P. C., Alves, J. F., & Chen, H. 2001, ApJ, 563, 903, arXiv:arXiv:astro-ph/0108470

Harvey, P., Merín, B., Huard, T. L., Rebull, L. M., Chapman, N., Evans, N. J. I., & Myers, P. C. 2007a, ApJ

Harvey, P. M., Chapman, N., Lai, S.-P., Evans, II, N. J., Allen, L. E., Jørgensen, J. K., Mundy, L. G., Huard, T. L., Porras, A., Cieza, L., Myers, P. C., Merín, B., van Dishoeck, E. F., Young, K. E., Spiesman, W., Blake, G. A., Koerner, D. W., Padgett, D. L., Sargent, A. I., & Stapelfeldt, K. R. 2006, ApJ, 644, 307

Harvey, P. M., Rebull, L. M., Brooke, T., Spiesman, W. J., Chapman, N., Huard, T. L., Evans, II, N. J., Cieza, L., Lai, S.-P., Allen, L. E., Mundy, L. G., Padgett, D. L., Sargent, A. I., Stapelfeldt, K. R., Myers, P. C., van Dishoeck, E. F., Blake, G. A., & Koerner, D. W. 2007b, ApJ, 663, 1139, arXiv:arXiv:0704.0253

Heiles, C. 1969, ApJ, 156, 493

Herschel, W. 1785, Philosophical Transactions Series I, 75, 213

Howell, S. B. 2000, Handbook of CCD Astronomy (Handbook of CCD astronomy / Steve B. Howell. Cambridge, U.K. ; New York : Cambridge University Press, c2000. (Cambridge observing handbooks for research astronomers ; 2))

Huard, T., Crews, L. J., Murphy, D. C., Myers, P, C., Lada, C. J., Bourke, T., & Evans, N. J. 2007, in prep.

Indebetouw, R., Mathis, J. S., Babler, B. L., Meade, M. R., Watson, C., Whitney, B. A., Wolff, M. J., Wolfire, M. G., Cohen, M., Bania, T. M., Benjamin, R. A., Clemens, D. P.,

Dickey, J. M., Jackson, J. M., Kobulnicky, H. A., Marston, A. P., Mercer, E. P., Stauffer, J. R., Stolovy, S. R., & Churchwell, E. 2005, ApJ, 619, 931, arXiv:astro-ph/0406403

Jarrett, T. H. 1992, PhD thesis, AA(Massachusetts Univ., Amherst.)

Jarrett, T. H., Dickman, R. L., & Herbst, W. 1994, ApJ, 424, 852

Jenkins, E. B. & Savage, B. D. 1974, ApJ, 187, 243

Jijina, J., Myers, P. C., & Adams, F. C. 1999, ApJS, 125, 161

Jørgensen, J. K., Harvey, P. M., Evans, II, N. J., Huard, T. L., Allen, L. E., Porras, A., Blake, G. A., Bourke, T. L., Chapman, N., Cieza, L., Koerner, D. W., Lai, S.-P., Mundy, L. G., Myers, P. C., Padgett, D. L., Rebull, L., Sargent, A. I., Spiesman, W., Stapelfeldt, K. R., van Dishoeck, E. F., Wahhaj, Z., & Young, K. E. 2006, ApJ, 645, 1246, arXiv:arXiv:astro-ph/0603547

Kandori, R., Dobashi, K., Uehara, H., Sato, F., & Yanagisawa, K. 2003, AJ, 126, 1888, arXiv:astro-ph/0308314

Kim, S.-H., Martin, P. G., & Hendry, P. D. 1994, ApJ, 422, 164

Knez, C., Boogert, A. C. A., Pontoppidan, K. M., Kessler-Silacci, J., van Dishoeck, E. F., Evans, II, N. J., Augereau, J.-C., Blake, G. A., & Lahuis, F. 2005, ApJ, 635, L145, arXiv:arXiv:astro-ph/0511467

Koornneef, J. 1983, A&A, 128, 84

Kramer, C., Richer, J., Mookerjea, B., Alves, J., & Lada, C. 2003, A&A, 399, 1073, arXiv:astro-ph/0212265

Kroupa, P., Tout, C. A., & Gilmore, G. 1993, MNRAS, 262, 545

Lada, C. J., Alves, J., & Lada, E. A. 1999, ApJ, 512, 250

Lada, C. J., Huard, T. L., Crews, L. J., & Alves, J. F. 2004, ApJ, 610, 303, arXiv:astro-ph/0404054

Lada, C. J., Lada, E. A., Clemens, D. P., & Bally, J. 1994, ApJ, 429, 694

Lee, C. W., Myers, P. C., & Tafalla, M. 1999, ApJ, 526, 788, arXiv:arXiv:astro-

ph/9906468

Leger, A. & Puget, J. L. 1984, A&A, 137, L5

Lilley, A. E. 1955, ApJ, 121, 559

Lombardi, M. & Alves, J. 2001, A&A, 377, 1023, arXiv:astro-ph/0109135

Lombardi, M., Alves, J., & Lada, C. J. 2006, A&A, 454, 781, arXiv:arXiv:astro-ph/0606670

Lutz, D. 1999, 623

Lutz, D., Feuchtgruber, H., Genzel, R., Kunze, D., Rigopoulou, D., Spoon, H. W. W., Wright, C. M., Egami, E., Katterloher, R., Sturm, E., Wieprecht, E., Sternberg, A., Moorwood, A. F. M., & de Graauw, T. 1996, A&A, 315, L269

Makovoz, D. & Marleau, F. R. 2005, PASP, 117, 1113, arXiv:arXiv:astro-ph/0507007

Mathis, J. S., Rumpl, W., & Nordsieck, K. H. 1977, ApJ, 217, 425

Moore, T. J. T., Lumsden, S. L., Ridge, N. A., & Puxley, P. J. 2005, MNRAS, 359, 589, arXiv:arXiv:astro-ph/0502407

Nordlund, Å. K. & Padoan, P. in , Interstellar Turbulence, ed. J. FrancoA. Carraminana, 218–+

Ossenkopf, V. & Henning, T. 1994, A&A, 291, 943

Ostriker, E. C., Stone, J. M., & Gammie, C. F. 2001, ApJ, 546, 980, arXiv:astro-ph/0008454

Padgett, D. L., Rebull, L. M., Stapelfeldt, K. R., Chapman, N. L., Lai, S.-P., Mundy, L. G., Evans, II, N. J., Brooke, T. Y., Cieza, L. A., Spiesman, W. J., Noreiga-Crespo, A., Allen, L. E., Blake, G. A., Harvey, P. M., Huard, T., Jørgensen, J. K., Koerner, D. W., Myers, P. C., Sargent, A. I., Teuben, P. J., van Dishoeck, E. F., Wahhaj, Z., & Young, K. E. 2007, in prep.

Padoan, P., Jones, B. J. T., & Nordlund, A. P. 1997, ApJ, 474, 730, arXiv:astro-ph/9603061

Passot, T. & Vázquez-Semadeni, E. 1998, Phys. Rev. E, 58, 4501, arXiv:arXiv:physics/9802019

Pound, M. W., Wolfire, M. G., & Amarnath, N. S. Astronomical Society of the Pacific Conference Series, Vol. 314, , Astronomical Data Analysis Software and Systems (ADASS) XIII, ed. F. OchsenbeinM. G. Allen & D. Egret, 784–+

Pound, M. W., Wolfire, M. G., Mundy, L. G., Teuben, P. J., & Lord, S. Astronomical Society of the Pacific Conference Series, Vol. 216, , Astronomical Data Analysis Software and Systems IX, ed. N. MansetC. Veillet & D. Crabtree, 628–+

Predehl, P. & Schmitt, J. H. M. M. 1995, A&A, 293, 889

Rebull, L. M., Stapelfeldt, K. R., Evans, II, N. J., Joergensen, J. K., Harvey, P. M., Brooke, T. Y., Bourke, T. L., Padgett, D. L., Chapman, N. L., Lai, S.-P., Spiesmann, W. J., Noreiga-Crespo, A., Merin, B., Huard, T., Allen, L. E., Blake, G. A., Jarrett, T., Koerner, D. W., Mundy, L. G., Myers, P. C., Sargent, A. I., van Dishoeck, E. F., Wahhaj, Z., & Young, K. E. 2007, ApJS, arXiv:astro-ph/0701711

Rieke, G. H. & Lebofsky, M. J. 1985, ApJ, 288, 618

Rieke, G. H., Young, E. T., Engelbracht, C. W., Kelly, D. M., Low, F. J., Haller, E. E., Beeman, J. W., Gordon, K. D., Stansberry, J. A., Misselt, K. A., Cadien, J., Morrison, J. E., Rivlis, G., Latter, W. B., Noriega-Crespo, A., Padgett, D. L., Stapelfeldt, K. R., Hines, D. C., Egami, E., Muzerolle, J., Alonso-Herrero, A., Blaylock, M., Dole, H., Hinz, J. L., Le Floc'h, E., Papovich, C., Pérez-González, P. G., Smith, P. S., Su, K. Y. L., Bennett, L., Frayer, D. T., Henderson, D., Lu, N., Masci, F., Pesenson, M., Rebull, L., Rho, J., Keene, J., Stolovy, S., Wachter, S., Wheaton, W., Werner, M. W., & Richards, P. L. 2004, ApJS, 154, 25

Rosenthal, D., Bertoldi, F., & Drapatz, S. 2000, A&A, 356, 705, arXiv:arXiv:astro-ph/0002456

Scalo, J., Vazquez-Semadeni, E., Chappell, D., & Passot, T. 1998, ApJ, 504, 835,

arXiv:arXiv:astro-ph/9710075

Schechter, P. L., Mateo, M., & Saha, A. 1993, PASP, 105, 1342

Schnee, S. L., Ridge, N. A., Goodman, A. A., & Li, J. G. 2005, ApJ, 634, 442, arXiv:arXiv:astro-ph/0508042

Shu, F. H., Adams, F. C., & Lizano, S. 1987, ARA&A, 25, 23

Strafella, F., Campeggio, L., Aiello, S., Cecchi-Pestellini, C., & Pezzuto, S. 2001, ApJ, 558, 717

Straizys, V., Cernis, K., & Bartasiute, S. 1996, Baltic Astronomy, 5, 125

Surace, J. A., Shupe, D. L., Fang, F., Lonsdale, C. J., Gonzalez-Solares, E., Baddedge, T., Frayer, D., Evans, T., Jarrett, T., Padgett, D. L., Castro, S., Masci, F., Domingue, D., Fox, M., Rowan-Robinson, M., Perez-Fournon, I., Olivier, S., Poletta, M., Berta, S., Rodighiero, G., Vaccari, M., Stacey, G., Hatziminaoglou, E., Farrah, D., Siana, B., Smith, H. E., Franceschini, A., Owen, F., Pierre, M., Xu, C., Afonso-Luis, A., Davoodi, P., Dole, H., Pozzi, F., Salaman, M., & Waddington, I. 2004, VizieR Online Data Catalog, 2255, 0

Trumpler, R. J. 1930, PASP, 42, 214

Vazquez-Semadeni, E. 1994, ApJ, 423, 681

Vrba, F. J., Coyne, G. V., & Tapia, S. 1993, AJ, 105, 1010

Weingartner, J. C. & Draine, B. T. 2001, ApJ, 548, 296, arXiv:astro-ph/0008146

Werner, M. W., Roellig, T. L., Low, F. J., Rieke, G. H., Rieke, M., Hoffmann, W. F., Young, E., Houck, J. R., Brandl, B., Fazio, G. G., Hora, J. L., Gehrz, R. D., Helou, G., Soifer, B. T., Stauffer, J., Keene, J., Eisenhardt, P., Gallagher, D., Gautier, T. N., Irace, W., Lawrence, C. R., Simmons, L., Van Cleve, J. E., Jura, M., Wright, E. L., & Cruikshank, D. P. 2004, ApJS, 154, 1, arXiv:astro-ph/0406223

Whittet, D. C. B. 1992, Dust in the galactic environment (The Graduate Series in Astronomy, Bristol: Institute of Physics (IOP) Publishing, 1992)

Wilson, R. W., Jefferts, K. B., & Penzias, A. A. 1970, ApJ, 161, L43+

Wolf, M. 1923, Astronomische Nachrichten, 219, 109

Wood, D. O. S., Myers, P. C., & Daugherty, D. A. 1994, ApJS, 95, 457

Young, C. H., Jørgensen, J. K., Shirley, Y. L., Kauffmann, J., Huard, T., Lai, S.-P., Lee, C. W., Crapsi, A., Bourke, T. L., Dullemond, C. P., Brooke, T. Y., Porras, A., Spiesman, W., Allen, L. E., Blake, G. A., Evans, II, N. J., Harvey, P. M., Koerner, D. W., Mundy, L. G., Myers, P. C., Padgett, D. L., Sargent, A. I., Stapelfeldt, K. R., van Dishoeck, E. F., Bertoldi, F., Chapman, N., Cieza, L., DeVries, C. H., Ridge, N. A., & Wahhaj, Z. 2004, ApJS, 154, 396